Fundamental study of surface charging in solid-liquid systems

by

Zhixiang Chen

A thesis submitted in partial fulfillment of the requirements for the degree of

Doctor of Philosophy

in

Chemical Engineering

Department of Chemical and Materials Engineering

University of Alberta

Abstract

Surface charging in solid-liquid systems is an elementary process influencing the performance of various industrial processes such as colloidal production, oil transportation, green energy harvesting and self-power sensor fabrication. The surface charging of solids in various liquid systems is possibly influenced by ionization and electron transfer, although this assumption has not been verified.

The focus of this thesis is the fundamental understanding of surface charging between a solid-nonpolar solvent or solid-water systems. A unique method was developed based on a custom designed Triboelectric Nanogenerator (TENG). Two surfaces of the TENG's triboelectric materials, water and Teflon, possess opposite charges, which create an electric potential difference between the electrodes as they separate. Connecting an impedance causes a current to flow between the electrodes, which screens up the electric field created by the separated charged surfaces. Bringing the two surfaces back into contact results in a change in the potential difference between the two electrodes, causing a backward flow of current. This alternative current (AC) can be observed when the cycle is repeated. Experimental parameters can be flexibly adjusted, including liquid and surface properties.

Through the design of the surface microstructure, we revealed the influence of the curvature on surface charging in the liquid-solid made TENG. The convex surface (negative curvature) is more conducive to the electron transfer with liquid drops than that of the concave surface (positive curvature). A statistical trend was found in which a smaller curvature would typically lead to a higher charging rate of negative charges after contact electrification (CE). After contact separation, the charge transfer from the surface to the atmosphere followed an exponential decay at a fixed temperature. In contrast with the curvature effect on the triboelectric charge generation, the charges on the concave surface were more likely to be emitted into the atmosphere than those on the convex surface. Based on these experimental results, we propose a curvature-dependent charge transfer model for distinct materials CE by introducing curvature-induced energy shifts of the surface states.

The solid surface chemical properties are then changed by trapping a layer of lubricant oil at the solid porous medium surface, leading to superhydrophobic feature and having low friction to water droplets. Increasing the lubricant volume caused a sharp decrease in the surface charging capability. This is most likely because the water-lubricant-infused solid CE is a combination of water-lubricant and water-solid CEs, whereas the triboelectric charges generated from the liquid-liquid CE are weaker than a water drop impacting on a solid. Theoretical calculations and atomic force microscope (AFM) measurements showed that a thin layer of oil (20 nm in thickness) on the porous solid surface was enough to preserve the advantage of low contact hysteresis if the moving velocity of the droplet on the surface surpassed a threshold (e.g., 0.3 mm/s). Importantly, we integrated the slippery lubricant-infused porous surface (SLIPS) with transistor-inspired architecture to produce a robust single-electrode triboelectric nanogenerator (SLIPS-SE-TENG) that could harvest triboelectric energy in all kinds of weather. This SLIPS-SE-TENG enhanced the instantaneous short-circuit current (~3 μA) by two orders of magnitude over an equivalent device (~0.02 μA) that has been previously reported in the literature.

Preface

This thesis is composed of several papers that have been published. Below is the statement of contributions to these co-authored papers that are presented in Chapters 4, 5 and Appendix C.

Chen, Zhixiang, Yi Lu, Rogerio Manica, and Qingxia Liu. "Curvature effect in liquid-solid contact electrification." *Nano Energy (2021): 106456.* Zhixiang Chen: Conceptualization, Methodology, Data collection, Writing-original draft. Yi Lu: Methodology, Validation, Writing – review & editing. Rogerio Manica: Writing – review & editing. Qingxia Liu: Resources, Writing – review & editing, Supervision, Project administration, funding acquisition. All authors contributed to the discussion and commented on the manuscript.

Chen, Zhixiang, Yi Lu, Rui Li, Rogerio Manica, and Qingxia Liu. " Liquid-solid triboelectric nanogenerators for a wide operation window based on slippery lubricant-infused surfaces (SLIPS)". *Chemical Engineering Journal (2022): 135688.* Zhixiang Chen: Conceptualization, Methodology, Data collection, Writing-original draft. Yi Lu: Methodology, Validation, Writing – review & editing. Rui Li: Data analysis. Rogerio Manica: Writing – review & editing. Qingxia Liu: Resources, Writing – review & editing, Supervision, Project administration, funding acquisition. All authors contributed to the discussion and commented on the manuscript.

Chen, Zhixiang, Yi Lu, Mahsa Nazemi Ashani, Rogerio Manica, Liyuan Feng, and Qingxia Liu. "Modulation of Surface Charge by Mediating Surface Chemical Structures in Nonpolar Solvents with Nonionic Surfactant Used as Charge Additives." *The Journal of Physical Chemistry C (2021), 125(35):19525-36.* Zhixiang Chen performed all the experiments and data analysis and wrote the entire paper. Yi Lu provided valuable suggestions and helped with the manuscript proofreading. Mahsa Nazemi Ashani helped with the modelling section. Qingxia Liu supervised the work. Liyuan Feng was involved in the experimental design. All authors contributed to the discussion and commented on the manuscript.

To my wife

I am so blessed to have you in my life.

Acknowledgments

First and foremost, I would like to thank my supervisor, Professor Qingxia Liu, for his instruction, support, and motivation throughout each stage of my graduate study.

I would like to express my sincere appreciation to Dr. Yi Lu, for all the discussions on science and life. I am also in debt to him for his guidance, encouragement, and patience.

I also express my thanks to the Candidacy Committee, Professor Peichun Amy Tsai, Professor Erin Bobicki, Professor Michael Serpe and Professor Qi Liu, for giving very helpful suggestions and opinions in the candidate exam.

Thank my roommate, Zhiqing Zhang, who is always able to communicate various scientific issues and daily chores, so that I can avoid the boredom of scientific research.

I thank Dr. Rogerio Manica, Dr. Bo Liu, Dr. Chao Qi, Tianzi Bai, Dr. Rui Li, Mingda Li, Dr. Bailing Xiang, and Jingqiao Li for their training and discussions.

I acknowledge Ms. Laurie Kachmaryk, Mr. James Skwarok, Mr. Shihong Xu, Ms. Nancy Zhang, for their administrative and technical assistance.

I am happy to meet all the colleagues and friends in our research group. Their accompany in the past years becomes an important section of my life.

My deepest gratitude goes to my parents, my sister Zhichong Chen, and my wife Chunlan Zhong for all the love and support.

Contents

List of Figures

List of Tables

Chapter 1

Introduction

1.1 Background and motivation

Surface charging between solids and liquids appears everywhere in our daily life. For example, makeup products involve stable colloids as their functional content which require a strong surface charge density on a solid surface to keep particles stably distributed. In the oil painting industry, satisfying surface charging capacity on the solid surface is also required to keep the suspension as stable as possible. In addition, surface charging ability plays an important role in energy harvesting by triboelectric nanogenerator (TENG), a self-powered sensor fabrication. However, a strong surface charge is sometimes pernicious and can cause discomfort or even disaster. An example is the static shock from a metal door handle that everyone has experienced, especially in cold and dry weather. More seriously, the static electricity generated inside the oil pipe owing to contact electrification between the oil flow and the PTFE pipe can trigger an explosion; such accidents are often reported from oil plants and gas stations.

It is obvious that fundamental research on surface charging between solids and liquids is important and meaningful not only in industry but also in environmental protection and sustainable energy development. For example, relying on contact electrification to harvest more clean energy could partially replace the traditional energy generated by fuel burning, which is the main source of air pollution around the world. Second, with the world's energy needs increasing, actively looking for low-cost, sustainable methods to collect energy must be a long-term goal. Finally, our lives have entered a completely new era of scientific and technological intelligence. From smart homes and intelligent control of self-charging sensors to the construction of the "Internet of Things," various small devices are required for continuous tracking and real-time monitoring. In the smart era, equipment requiring a power supply is widely distributed, and the power supply ranges from W to μW. There is an urgency to develop new technologies and new methods to obtain clean and renewable energy sources at a myriad of scales.

1.2 Objectives and scope of the thesis

The main objective of this work is to investigate the surface charging between solids and liquids (organic solvents/water) by direct surface potential (or current) measurements and theoretical analysis. A homemade triboelectric nanogenerator (TENG) device was used to provide a fundamental understanding of the process, in which the electric strength after CE between solids and liquids could be quantified during the contact-separate process.

In Chapter 4, it is demonstrated that the short-circuit current output performance of a liquid–solid TENG could be greatly improved by designing the insulating surface with an increased surface coverage of convex areas. The best performing TENG used surfaces with more negatively curved regions (convex areas), which suggests that a convex surface leads to more electrons negatively charging the surface. In general, this study provides not only new insights for understanding CE but also a novel pathway to improve the performance of the liquid–solid TENG.

In Chapter 5, we integrated the slippery lubricant-infused porous surface (SLIPS) with transistor-inspired architecture to produce a robust TENG. The integrated transistor-inspired architecture SLIPS-SE-TENG (~3 μA) directly enhances the instantaneous short-circuit current by two orders of magnitude over equivalent devices (~0.02 μA) that are limited by interfacial effects. More importantly, compared to a superhydrophobic fabricated TENG, this novel SLIPS-SE-TENG device can work normally and stably in harsh environments, such as those with low temperatures or high humidity.

1.3 Structure of the thesis

This thesis includes 6 Chapters, with Chapters 4 to 5 containing the papers that have been published. The detailed content of each chapter is introduced below:

Chapter 1 provides a brief introduction to the thesis's background and motivations, objectives and scope, and structure.

Chapter 2 contains a literature review of the fundamental knowledge of surface charging between solids and liquids, the available application of surface charging (especially in relation to the harvesting of blue energy), and several remaining questions that should be further explored.

Chapter 3 provided all involved materials and methods as well as the corresponding operating procedures.

Chapter 4 describes the curvature effects on liquid–solid contact electrification. The magnitude of charge transfer during liquid–solid contact electrification (CE) is quantified to investigate its dependency on the curvature of the sample surfaces. A statistical trend is found in which a smaller curvature would typically lead to a higher charge rate of negative charges after CE. In addition, the charge transfer from the surface to the atmosphere follows an exponential decay at a fixed temperature after separation from contact. In contrast to the curvature effect on triboelectric charge generation, the charges on the concave surface are more likely to be emitted into the atmosphere than those on the convex surface. Results from this chapter have been published:

(Zhixiang Chen, Yi Lu, Rogerio Manica, and Qingxia Liu. Curvature effect in liquid-solid contact electrification. *Nano Energy (2021): 106456.*)

Chapter 5 illustrates the slippery interface integrated with transistor-inspired architecture producing a robust triboelectric nanogenerator. Compared to the superhydrophobic fabricated TENG, this novel SLIPS-SE-TENG device can work normally and stably in harsh environments, such as those with low temperatures or high humidity. The high adaptability in harsh environments and high light transmittance enabled by using a slippery surface also makes it possible to integrate SLIPS-SE-TENG with other optoelectronic devices such as solar cells for collecting both droplet and solar energy simultaneously. This chapter has been published:

(Zhixiang Chen, Yi Lu, Rui Li, Rojas J. Orlando, Rogerio Manica, and Qingxia Liu Liquid-solid triboelectric nanogenerators for a wide operation window based on slippery lubricant-infused surfaces (SLIPS)." *Chemical Engineering Journal (2022): 135688.*)

Chapter 6 contains the contribution to knowledge and suggestions for future work.

The appendix contains the MATLAB code applied in chapters 3 and 5, as well as one published work which presents the modulation of surface charges by mediating the surface chemical structures in nonpolar solvents with nonionic surfactants used as charge additives.

(Zhixiang Chen, Yi Lu, Mahsa Nazemi Ashani, Rogerio Manica, Liyuan Feng, and Qingxia Liu. Modulation of Surface Charge by Mediating Surface Chemical Structures in Nonpolar Solvents with Nonionic Surfactant Used as Charge Additives. *The Journal of Physical Chemistry C (2021), 125(35):19525-36.*)

Chapter 2

Literature Review

2.1 Introduction

Contact electrification (CE) is a scientific term for triboelectrification, which is a universal phenomenon that occurs for almost all materials, i.e., solid-solid, solid-liquid and liquid-liquid[1]. The scientific understanding of CE is still under debate even though it has been a well-known phenomenon for more than 2600 years. For example, whether electrons[2-4], ions[5, 6] or even material species[7, 8] are the nature of transferred charges in CE has been debated but not resolved conclusively. Recently, most of the research in a nanoscale by Kelvin probe force microscopy[9, 10] (KPFM) and Electrostatic force microscopy (EFM)[11, 12] has suggested that in the case of solid-solid, the contact charge transfer is mostly dominated by electrons transfer; in the case of solid-water, it may be the synergy of ions and electrons or the dominance of the electrons transfer[13, 14]. All conclusions mentioned above are based on the basic principle that electrons can be removed from the dielectric surface by photon excitation[15, 16] and thermal excitation[17, 18], but ions still reside stably on the surface[19, 20].

Surface charging at the liquid-solid interface is an important topic because many reactions in chemistry and biology are related to charge transfer at this interface, such as colloidal suspension[21, 22], electrowetting[23, 24], electrochemistry[25, 26], photovoltaic effect[27, 28], etc. On the other hand, the liquid-solid CE concerns almost all liquid-solid interfaces. Therefore, it is necessary to gain a deeper understanding in terms of the charge transfer at the liquid-solid interface from the viewpoint of liquid-solid CE.

This literature review provides a summary of the current studies on the charge transfer at the liquid-solid CE. First, a sequence of experiments that used specific micro-scale and large-scale observation strategies are explained to systematically clarify the fundamental understanding of CE at the liquid-solid interface. Subsequently, the TENG based on the solid-liquid CE is systematically summarized, and the practical applications of solid-liquid-based TENG are briefly described. Then, the bottlenecks in the development of surface charging applications (such as TENG) are enumerated and corresponding potential solutions are provided. Finally, a brief overview is given of the research and application of surface charging in other areas, such as the charging of solids in non-polar solutions.

2.2 CE at the water-solid interface

CE research has largely focused on issues related to solid-solid interactions, while liquid-solid interactions have been the subject of relatively few studies. The reason for this may be that liquid-solid interaction mechanisms are more complicated than those related to solid-solid interaction. In the 1980s, El-Kazzaz and Rose-Innes[29] studied the CE between liquid metals and solid insulators, marking one of the earliest examples of CE between liquids and solids. In their report, liquid metal was used as a contact pair to take advantage of the fluidity of the liquid metal to achieve a better interface contact and to gain a better understanding of solid-solid CE. Matsui *et al*.[30, 31] investigated the CE of water droplets by sliding them over insulator surfaces such as PTFE or resin in the 1990s. They proved that the water droplet was always positively charged. For a long time, most scientists[32-34] believed that the adsorption of negative ions from water to the surface of the insulator was the reason for the CE between the water and the insulator, although there was no reliable evidence. On the other hand, in the CE of the liquid-solid interface, there are many types of solids, such as conductors, semiconductors, and insulators that are rarely studied. In this study, we focus on the surface charging at the interface between the liquid and the insulator and refer to the literature[35, 36] on the CE relationship between liquid-conductor and liquid-semiconductor.

About ten years ago, the invention of a liquid-solid triboelectric nanogenerator (L-S TENG) fabricated by Wang *et al.*[37] provided the possibility of quantifying the CE effect. In recent years, researchers reviewed the identity of charge carriers in liquid-solid CE. This helps to distinguish whether the transferred charges are ions or electrons, which can be done by different methods including temperature-induced electron thermionic emission or ultraviolet-induced electron emission. If the surface temperature is moderate, neither of these two methods will release the adsorbed ions. For example, based on thermionic emission theory, Lin *et al.*[9, 38] designed a temperature-dependent charge decay experiment using Kelvin probe force microscopy (KPFM) on the nanoscale to quantify the electron transfer and ion transfer between the aqueous solution and the insulator, as shown in Fig. 2.1a-b. The results of the charging and heating cycle tests are shown in Fig. 2.1c. As SiO_2 was initially free of surface charge, its surface charge density was close to zero. As the SiO_2 surface came into contact with deionized water (DI), negative charges were transferred from the DI water to the surface. Through thermionic emission, the surface charge density decreased during heating. As a result, certain charges are not removed from the surface in the first cycle ("sticky" charges), which are ions generated on the surface in the liquid−solid CE. After several cycles, the sticky charge density increased to saturation.

While the ions were building on the surface, however, electron transfer was shown to be the dominant mechanism in the CE between a virgin SiO_2 surface and DI water at the very first contact. Additionally, researchers pointed out that the proportion between electron transfers and ion transfers was above 3:4. Recent literature has pointed out that both electron transfer and ion transfer occur in liquid-solid CE through electric force microscopy (EFM)[39] and “scanning TENG” techniques[40], with electron transfer possibly even dominating in some cases.

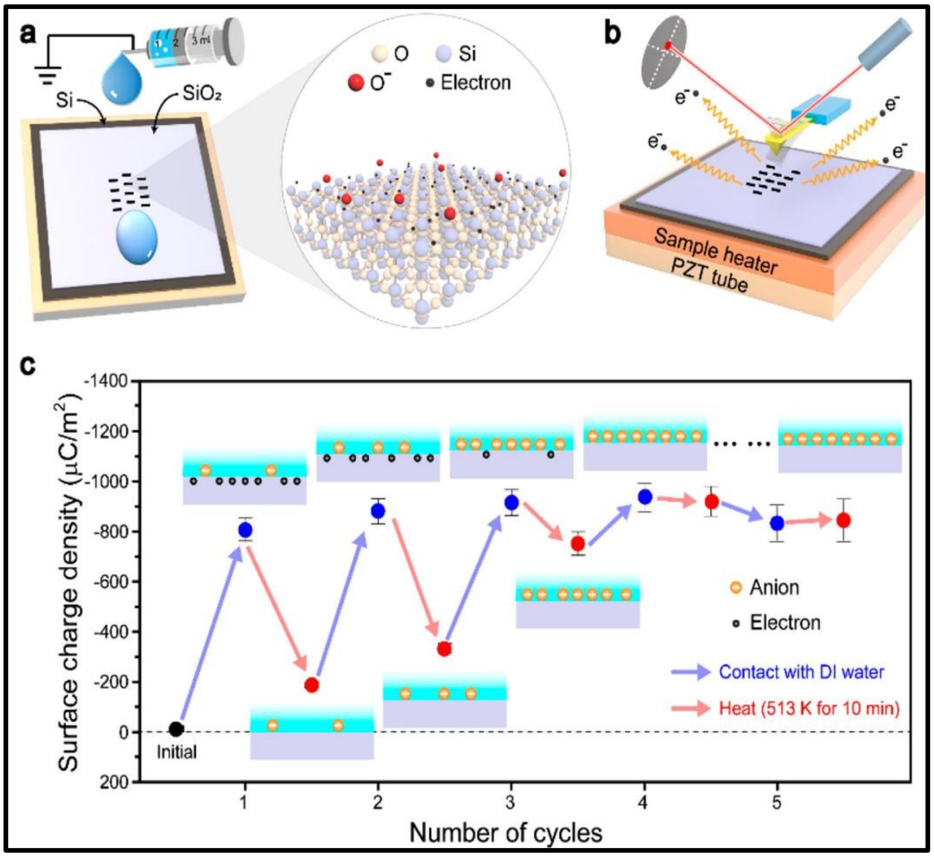

Figure 2.1: Temperature effect on the contact electrification between DI water and SiO_2[38]. (a) Setup of the contact charge experiment. (b) Setup of the AFM platform for the thermionic emission experiments. (c) Charge density on the SiO_2 surface in the charging and heating cycle tests. Copyright 2020 Nature Springer.

In addition to experimental studies, theoretical calculations have also shown that electrons can be transferred at the liquid-insulator interface. Using a quantum-mechanical model, Willatzen *et al.*[41] predicted the electron transfer in the CE for different materials systems, including liquid–solid cases. It was pointed out that ion transfer was not taken into consideration, but electron transfer was large enough to support CE between liquids and solids. Density functional theory (DFT) was used very recently by Sun *et al.*[42] to quantify the electron transfer in liquid-solid systems in different oxides. According to their study, liquid-solid electron transfer was linearly related to the dielectric function. The first-principles calculations performed in these studies were all based on electron transfer, which corroborates the experimental findings in CE on electron transfer.

Based on the electron transfer in liquid-solid CE, a "two-step" model for the formation of electrical double layer (EDL) was proposed by Wang *et al.*[34] in which the electron transfer plays a dominant role in the first step (Fig. 2.2a). During the first step, when the molecules in the solution approach a virgin surface that has no pre-existing surface charges, it is possible that the atoms or molecules in the solution directly interact with the atoms on the solid surface to form an overlap of electron clouds (Fig. 2.2b). Electron transfer occurs first to charge the "neutral" atoms on the solid surfaces, i.e., to form ions. In the second step, if ions exist in the liquid, such as H^+ and OH^-, the loosely distributed negative ions in the solution would be attracted to and migrate toward the surface bonded ions due to electrostatic interactions, forming an EDL. Both electron transfer and ion transfer co-exist at the liquid-solid interface.

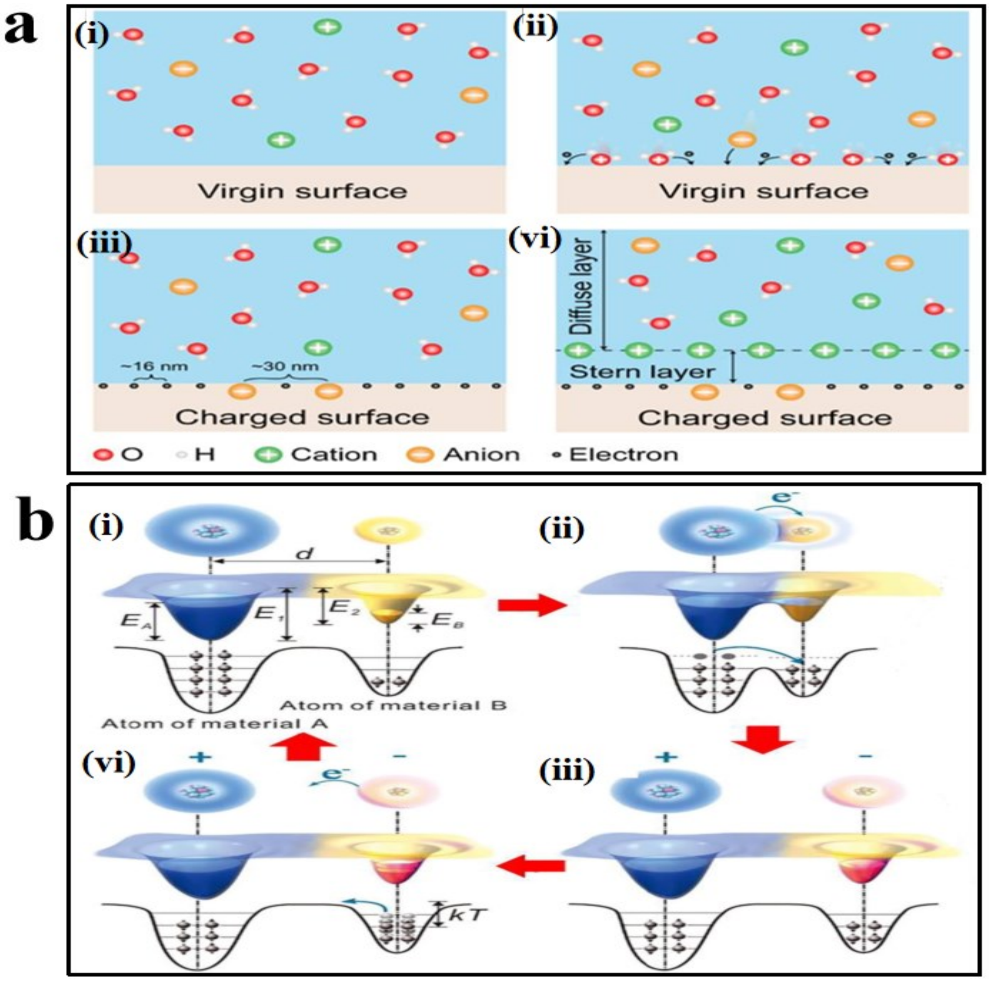

Figure 2.2: (a) The hybrid EDL model and the "two-step" process of its formation.[38] (i-iii) In the first step, the molecules and ions in the liquid impact the solid surface due to the thermal motion and the pressure from the liquid, which leads to electron transfer between them; meanwhile, ions may also attach to the solid surface. (iv) In the second step, free ions in the liquid would be attracted to the electrified surface due to electrostatic interactions, forming an EDL. (b) An electron-cloud-potential-well model proposed for explaining CE and charge transfer and release between two materials that may not have well-specified energy band structure, for general material cases. Schematic of the electron cloud and potential energy profile (3D and 2D) of two atoms belonging to materials A and B,

respectively, when they are: (i) before contact, (ii) in contact, and (iii) after contact, showing electron transfer from one atom to the other after being forced to have electron cloud overlap. (iv)Charge release from the atom at an elevated temperature T once kT approaches the barrier height. D is the distance between two nuclei; E_A and E_B, occupied energy levels of electrons; E_1 and E_2, potential energies for electrons to escape[34]. Copyright 2020 Nature Springer.

2.3 Liquid-solid CE-based TENG

It is well known that contact electrification exists everywhere, and this is at the heart of the newly discovered triboelectric nanogenerator (TENG). New strategies toward harnessing the kinetic energy of water have been proposed following the recent development of TENG, using the water-solid contact electrification technique has been reported by Lin *et al.*[34, 43] The two surfaces of TENG's triboelectric materials possess opposite charges, which creates an electric potential difference between the electrodes as they separate. Connecting a load will cause a current to flow between the electrodes, which will screen up the electric field created by the separated charged surfaces. Bringing the two surfaces back into contact results in a change in the potential difference between the two electrodes, which causes a backward flow of current. Hence, the alternative current (AC) can be observed when this cycle is repeated. TENG combines contact electrification and electrostatic induction[44-46], and is feature-rich with a low cost, significantly high output, and more material options[47-49], making it ideal for kinetic energy harvesting. Currently, five basic working modes have been developed in terms of a liquid-solid TENG. We will identify each working mode below.

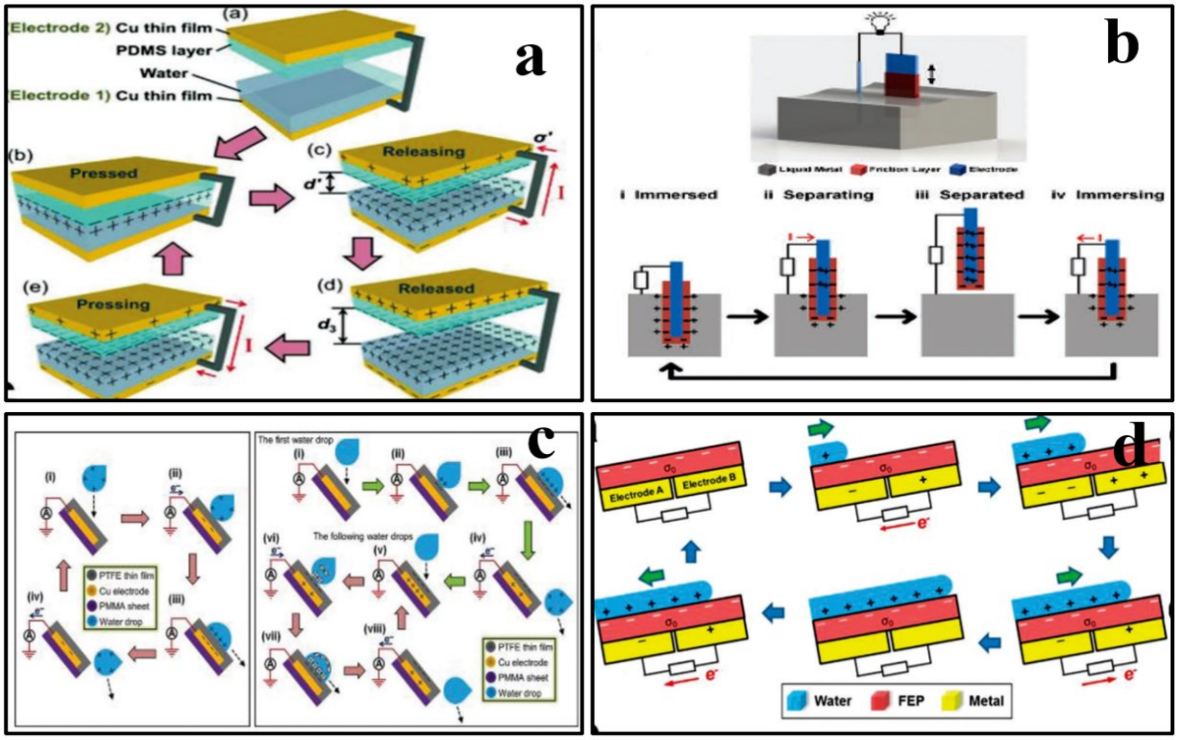

Figure 2.3: (a) Contact–separation mode of TENG[52]. (b) Sliding-mode TENG[53]. (c) Single-electrode-mode TENG[54]. (d) Freestanding-mode TENG[55]. Copyright 2020 Wiley.

Sliding Mode TENG: In the sliding mode, the liquid metal plays the role of the metal and makes contact with the dielectric material, such as polytetrafluoroethylene (PTFE), as shown in Fig. 2.3b[53]. Owing to the difference in electronegativity for the PTFE and the liquid metal, electrons are transferred from the liquid metal to the PTFE surface after contact. As the PTFE moves upward, the triboelectric charge on the surface drives the electrons to move from the induction electrode (the blue part) to the liquid metal through the external circuit. When the PTFE moves back into the liquid metal, the electrons move backward. Published results have indicated that gas molecules seem to play an important role in this kind of liquid-solid contact electrification[54]. For example, Kapton is negatively charged by contact with the liquid metal when exposed to oxygen but positively charged without oxygen.

Contact-Separation Mode: In a contact–separation-mode L-TENG (Fig. 2.3a), the contact of polydimethylsiloxane (PDMS) with water serves as the dielectric material[50]. In this mode, when PDMS is in contact with water, PDMS becomes negatively charged due to the ionization of the surface group, while the water remains positively charged. Triboelectric charges in the interface of PDMS and water will drive electrons in the external circuit to move from the back electrode of the PDMS to the back electrode of the water as they separate. Electrons move backwards when the PDMS approaches the water. Under mechanical triggering, an alternating current is generated in the external circuit. In addition, a comparison is made between the L-S TENG output produced using DI water, tap water and organic solvents[51]. According to the results, DI water produces the best performance, meaning that greater polarity in the liquid will provide a better electrification performance and therefore lead to a higher output. This is because an electrostatic field is formed on the surface of the solid film that collects the counterions in the water following contact electrification, forming an electrical double layer (EDL) to screen its surface charges. Charges on the solid surface are heavily screened by the moveable ions in the liquid. This is the main reason DI water shows the highest output performance.

Single-Electrode Mode TENG: When the water serves as a moving part, the single-electrode mode of the TENG should be the most suitable way to harvest energy, as shown in Fig. 2.3c.[56] Generally speaking, the water droplet is charged when falling from a certain height (initially positively charged by air or by the pump pipe),[57, 58] and it induces negative charges on the induction electrode (the orange part, covered by PTFE) after contact. On the contrary, if the water drop is free of charge (e.g., the metal pump pipe is grounded and it falls from a low height), the PTFE surface also could be negatively charged after contact with the water drop. To achieve an electrostatic equilibrium, when the water drops leaving off the PTFE surface the negative triboelectric charges will drive electrons in the back electrode of the PTFE film to move into the ground. This generates a detected current flowing from the ground to the TENG. Subsequentially, the charges on the PTFE surface will attract and realign the electric dipole moment in the water when the next water drop approaches the PTFE film. In this process, the positive holes will drive flow from the back electrode into the ground, therefore, creating a new electrostatic equilibrium.

Freestanding Mode TENG: The fourth mode of the L-S TENG is the freestanding mode, as shown in Fig. 2.3d.[55] After rubbing with a solid surface, e.g., Fluorinated ethylene propylene (FEP), by water drops, the FEP surface becomes negatively charged according to the difference of electronegativity. When the water drops move up and down, the negative charges on the FEP surface are screened by the electric dipole moment in the water, then the induced electrons move back and forth between the two electrodes A and B. Therefore, this kind of TENG is perfect for harvesting blue energy from water waves with a low and irregular waving frequency. For example, a published result indicated that the output of the freestanding mode TENG can reach 300 V and 15 μA of open-circuit voltage and short circuit current, respectively[59]. An output of this intensity is enough to power a wireless signal transmitter, which is very promising for the wireless monitoring of water quality, especially in rivers and in the deep ocean.

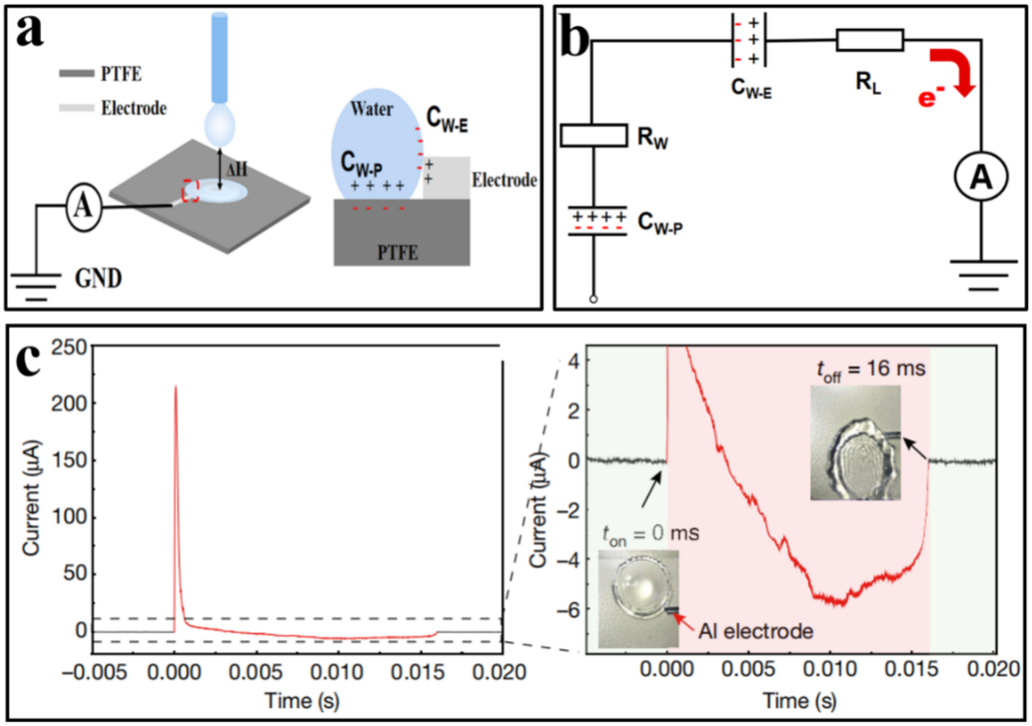

Figure 2.4: (a) The electricity generation of a single electrode TENG. By only assembling an electrode on the top surface of the material, the whole preparation of the TENG is completed. (b) The equivalent circuit model of the TENG. In the disconnected state, only capacitance $C_{W\text{-}P}$ remains in the open circuit. When the droplet contacts the electrode, $C_{W\text{-}E}$, existing between the water/electrode interfaces, is added into the connected circuit. R_W and R_L are the impedance of the water droplet and the load, respectively. There is a time-resolved variation in the current generated from the DEG during the entire droplet impact process. The dashed lines delineate the specific part of the current waveform as shown in c. (c) Synchronization of droplet-spreading dynamics and current response and mapping of the time-dependent variation in charges flowing between the PTFE/ITO and the aluminum electrode. The droplet retracts but still maintains contact with the aluminum electrode, while the current reverses to a negative value. Insets are snapshots showing droplet dynamics[60]. Copyright 2020 Nature Springer.

Transistor-Inspired Architecture Mode TENG: In 2020, the new transistor-inspired architecture TENG was designed by Xu *et al*.,[60] which directly enhanced the instantaneous power density by several orders of magnitude (Fig. 2.4c) over equivalent devices that are limited by interfacial effects. They developed a device to harvest energy from impinging water droplets by using an architecture that comprises a PTFE film on an indium tin oxide substrate plus an aluminum electrode fixed on the surface, as shown in Fig. 2.4a. They showed that the spreading of an impinged water droplet on the device bridges the originally disconnected components into a closed-loop electrical system, transforming the conventional interfacial effect into a bulk effect. The equivalent circuit model of the transistor structure inspired TENG is shown in Fig. 2.4b. When the impinging droplet contacts the electrode, the droplet bridges the originally disconnected components such as the solid surface and the single electrode into connection. A large number of negative or positive charges accumulate around the single electrode following an electrical signal output between the electrode and the ground. The direction of electron transfer depends on the charge polarity of the surface.

Currently, there are many reports on the functionalization of TENG, such as its use in self-powered liquid sensors. For example, Newaz *et al*.[61] developed a sensor for detecting the ion concentration and the velocity of the liquid flowing through a graphene-based field-effect transistor. Zhang *et al*.[62] presented a self-powered and highly sensitive acceleration sensor based on a solid-liquid TENG, which is fabricated from a liquid metal and nanofiber-networked film. The results indicate that the TENG output shows a linear trend as the acceleration changes with a sensitivity of 0.26 Vs^2/m.

Furthermore, the water-based TENG could be designed as a wearable and portable power source owing to the deformability of water drops. For example, Yi *et al.*[62] reported a bracelet-like device worn on a person's wrist which harvested energy from the tapping motion. Yang *et al.*[63] fabricated a wearable liquid-based TENG textile-like device, which generates a wide range of output from 0.5 Hz to 2.5 Hz. After connecting with a power management circuit, this device can power up different small electronics including a pedometer, calculator, and watch. An all-weather power generation-hybrid energy harvester is another powerful application based on the liquid-solid TENG. Zheng *et al.*[64] developed a hybridized cell by integrating a solar panel with a water-based TENG made up of transparent materials. Using this hybrid energy harvester, the cell can generate power continuously in any kinds of weather.

Finally, water-based TENG plays an important role in the harvesting of water wave energy in the ocean (blue energy). It is possible to collect more renewable and inexhaustible energy from the ocean, which covers more than 70% of the Earth's surface, through TENG. Wang *et al.*[65] proposed a method that uses a floating triboelectric nanogenerator network for energy harvesting. The energy collected by TENG (at 10 cm intervals) distributed in a square kilometer can generate enough electricity for a town. Li *et al.*[51] demonstrated a thin film and water-based TENG for ocean wave energy harvesting. According to reports, it can activate the wireless SOS signal transmission system to respond to marine emergencies. Furthermore, Zhao *et al.*[66, 67] displayed an in-situ, self-powered electrochemical protection system for equipment placed in the ocean. The results showed that after a few hours, the unprotected steel was corroded severely but the steel protected by TENG was not, which proved the effectiveness of the in-situ self-powered protection system. Further discussion about blue energy collection through TENG can be found in the literature.[68-70]

There has been a lot of research on the mechanism of CE, the related applications based on CE, and the great progress that has been made. However, related research about the impact of the solid surface properties on CE is still very limited. According to the reports published so far, it can be confirmed that the surface characteristics of triboelectric materials have important effects on the power generation performance of TENG.[34, 71] For example, Xu *et al*.[72] indicated that a CE of two pieces of chemically identical materials results in concave surfaces being positively charged and convex surfaces being negatively charged. The authors explained that surfaces with different curvatures have different surface energies due to the stretching or compressing of surface molecules.[73] Although the findings of curvature effect in macroscale are essential for understanding CE, it would be of great scientific value to explore this phenomenon on a smaller scale. In the real world, solid surfaces are not always molecularly smooth. Indeed, nanoscale surface curvatures commonly exist everywhere on a rough surface. Therefore, understanding how nanoscale surface roughness influences local triboelectric charges could broaden the applicability of the curvature effect in more universal scenarios. This topic can not only provide a deeper understanding of the mechanism of CE in principle but also allow the design of surface structure to artificially regulate the intensity of CE according to a specific purpose.

2.4 Integrated SLIPS-TENG

At present, the solid phase of TENG based on the solid/liquid interface is designed to be hydrophobic or superhydrophobic (SHS) to repel water droplets in time, refresh the contact points, and continue to generate electricity[74-76]. When these SHS are exposed to extreme environments such as high humidity and low temperature, more challenges arise. In both cases, the nucleation of nano-scale water droplets or ice/frost greatly inhibits the fluidity of the impacted droplets, which ultimately leads to the freezing of the entire surface and shields the generation and transmission of effective charges. Recently, the Nepenthes pitcher-inspired slippery liquid-infused porous surface (SLIPS) has gained gradual attention owing to the special nature of its surface[77].

The Nepenthes pitcher is composed of hydrophilic and rough surfaces, with high sugar and hygroscopic nectar. As a typical representative of SLIPS, it exhibits an excellent anti-wetting ability and is considered a potential solution to the problem of superhydrophobic surfaces[78, 79]. In a humid environment, these surfaces can be completely wetted by the lubrication of water to form a uniform liquid film, which allows insects with soft sticky pads to slip and be easily captured. Inspired by Nepenthes, as early as 1959, researchers conceived of SLIPS, a new type of functional material and a smooth lubricant which was injected onto a porous surface with a contact angle of about 90° and a very low contact angle hysteresis[79]. It was not until 2011 that the importance of SLIPS was realized as they performed well in self-healing, omniphobicity, and pressure stability, etc[77, 80]. The surface properties themselves do not produce non-wetting properties, but instead, hold the lubricant in place by capillary force. Unlike the surface inspired by the lotus leaf, SLIPS do not rely on a stable liquid-gas interface, but a thin and movable layer of lubricant that spontaneously attracts texture features and constantly replenishes damaged areas[77, 81]. Compared with the compressible air layer of the super-hydrophobic surface, this movable and incompressible lubricant layer ensures these surfaces have good instantaneous self-healing performance and pressure stability. Moreover, the injected lubricant creates an atomically smooth, continuous, and chemically uniform interface. This prevents foreign liquids from directly contacting and contaminating the substrate, resulting in a defect-free, no-pinning (a mobile three-phase contact line) and omniphobic surface, with the contact angle hysteresis of almost all liquids being extremely low[82]. The movement of the three-phase contact line on the surface can also bring other benefits, such as anti-fouling, anti-icing, self-cleaning, and so on. In addition, the presence of the liquid layer prevents the nucleation of droplets in the texture, so SLIPS can continue to work even in humid conditions.[83]

There is great potential in integrating SLIPS and TENG to improve the performance of TENG. However, there is only one scientific article on the combination of SLIPS and TENG[84]. By combining SLIPS with a traditional inductive charging mode as shown in Fig. 2.5a, the authors realized that TENG can work normally throughout at extremely low temperatures (-3℃, Fig. 2.5b). Regrettably, the designed TENG power generation performance was relatively low, only about 0.2 μW, owing to the limitations imposed by interfacial effects—as seen in characterizations of the charge generation and transfer that occur at solid–liquid or liquid–liquid interfaces. Answering the question of how to further improve the output performance of TENG on this basis is a prerequisite for determining whether SLIPS can be further applied in the future.

Combining the inherent advantages of SLIPS and the architecture inspired by transistors provides a new idea for the design of high-efficiency water kinetic energy collection devices (SLIPS-TENG). This new design of SLIPS-TENG may not only have the advantages of SLIPS but also possibly further improve energy conversion efficiency and long-term output stability. To the best of our knowledge, no published reports have verified and realized this unique design. This is a difficult task to achieve because the oil layer on the surface of SLIPS is not conducive to contact between the droplets and the solid surface at the bottom, which means that the contact electrification effect can deteriorate, which greatly affects the output performance of TENG. So, we must study how to coordinate the properties of SLIPS and TENG performance to achieve the integration of SLIPS-TENG.

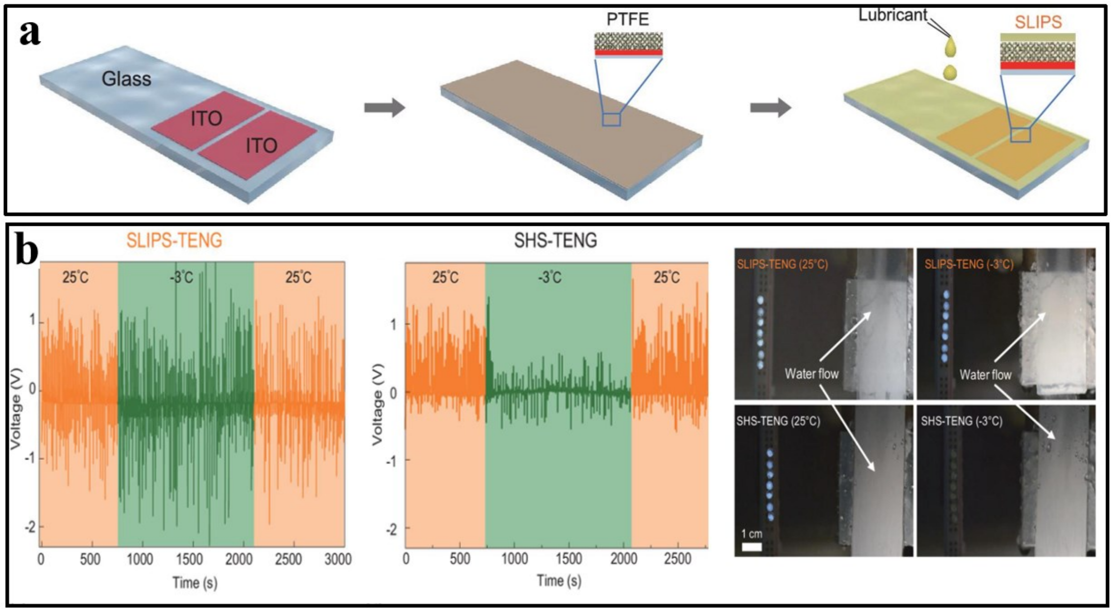

Figure 2.5: (a) Schematic drawing of the SLIPS-TENG fabrication process. (b) The time-dependent variation of the open-circuit voltage of SLIPS-TENG at 25 ºC and −3 ºC, respectively. SLIPS-TENG shows an enhanced stability of electrical output due to the super-slippery interface. In contrast, upon lowering the temperature below the freezing point, small condensate droplets are formed and adhere on the superhydrophobic surface (SHS), preventing an effective charge separation in the triboelectricity process. Copyright 2019 Oxford Academic Journal.

Chapter 3

Materials and Experiments

3.1 Materials

Ethanol (96%, Sigma), perfluoropolyether (PFPE, Miller-Stephenson, United States), silica nanospheres (Nano Composix, San Diego), polytetrafluoroethylene (PTFE) dispersion in H_2O (~60%, Sigma), extra dry n-heptane (>99%, Fisher Scientific), extra dry dodecane (>99%, Sigma), nitrogen gas (4.8 T, Prexair), argon gas (100%, Prexair), parafilm (PARAFILM® M, Sigma) were used without further purification.

Milli-Q water, PFPE oil (Dupont Krytox GPL 103, Miller Stephenson), mineral oil (Fisher Scientific, Pure) and silicone oil (Fisher Scientific, 100%) were used without further purification. The thickness and average pore size of the porous PTFE membranes (Sterlitech Coporation, 0QL8222005) were 20 μm and 450 nm, respectively.

3.2 Insulating surface preparation

The pretreated glass (uneven concave shape on the surface) was purchased from Nano Fabrication Center (NanoFab, University of Alberta). These glasses were coated by fluorocarbon oil (PFPE) (*M-glass-1*) or silica nanoparticles-PFPE (*M-glass-2*). Details of glass surface wettability is provided in the Fig. 3.1.

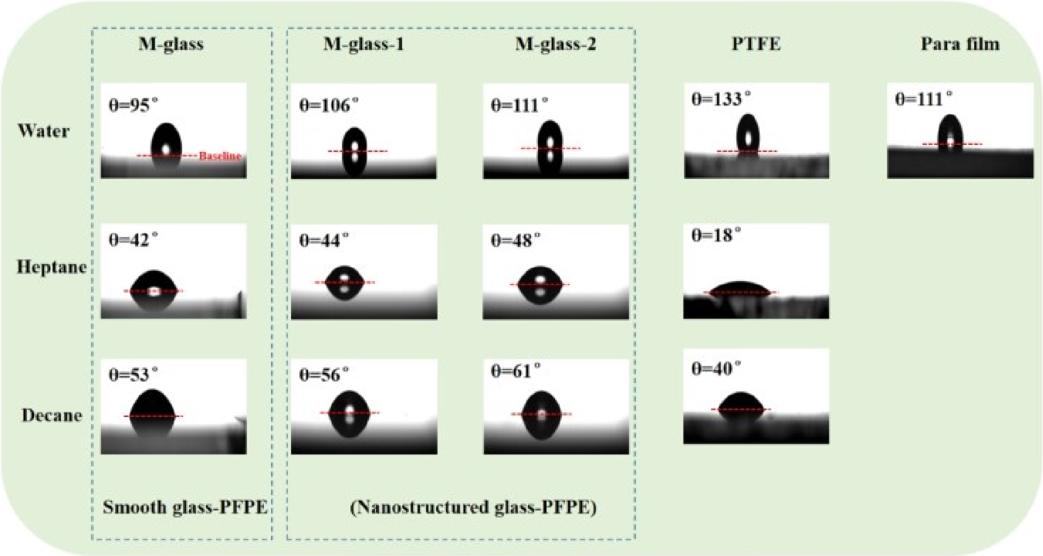

Figure 3.1: Wettability of studied surfaces.

It is worth pointing out that the distribution of PFPE on the two glass surfaces is completely uniform after the coating treatment, as shown by the force mapping analysis (Fig. 3.2). Adhesion force mapping was carried out using a silicon probe (Multi75Al-G, BudgetSensors; cantilever stiffness 3 N/m) with scanning size 2 μm and 32×32 points by a commercial MFP-3D AFM system (Asylum Research, Santa Barbara, CA). Before the AFM experiment, all samples were carefully cleaned by immersing pure glass in acidic piranha for 10 min. The coated sample was sonicated in the aqueous solution for 5 minutes, then rinsed with toluene, acetone, water, and acetone. Tests were conducted immediately after drying the sample surface by N_2 blowing. The adhesive force mappings were performed in argon atmosphere at room temperature (~ 23 ℃). The force mapping images of the three investigated surfaces are provided in Fig. 3.2 (d-f). The tip (silicon) used in the present study shows distinctly higher adhesion forces to polar surfaces (e.g., pure glass, Rq=0.21 nm) compared to nonpolar surfaces (e.g., *M-glass-1* and *M-glass-2*) and is thus representative of an attraction of polar molecules between surface and tip. In other words, if there is an uneven PFPE distribution on the surface (*M-glass-1* and *M-glass-2*), the force mapping results should show have shown a large adhesion force spot, similar to the one shown in Fig. 3.2d. Obviously, the adhesion values of the force mapping of the two PFPE coating surfaces in Fig. 3.2e and Fig. 3.2f are evenly distributed around 3.9 nN. Therefore, it is reasonable to assume that the PFPE coated surface is chemically uniform and there is no exposed polar group on *M-glass-1*(Rq=4.01 nm, Fig. 3.2b) or *M-glass-2*(Rq=3.47 nm, Fig. 3.2c) surfaces.

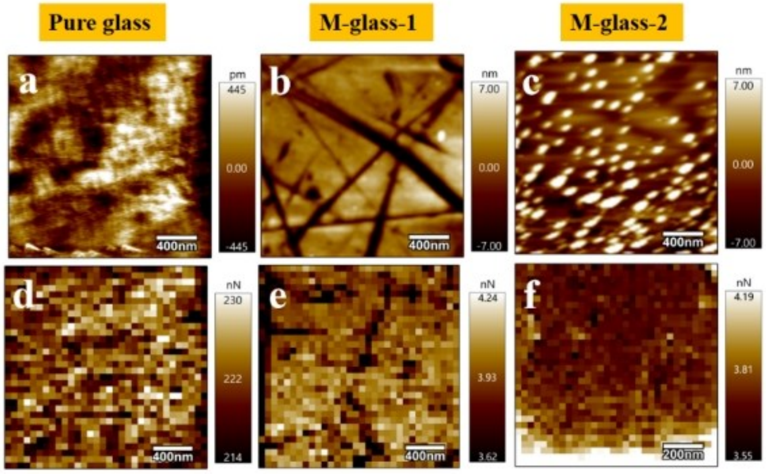

Figure 3.2: Topography of three surfaces (a) pure glass (b) *M-glass-1* (c) *M-glass-2* through contact mode AFM scanning. The corresponding in-situ force mapping of (d) pure glass (e) *M-glass-1* and (f) *M-glass-2* surfaces.

Glass surface (M-glass-1) fabrication. The pretreated glass was rinsed by deionized (DI) water, immersed in ethanol, vibrated in an ultrasonic bath for 15 minutes, and dried by gently blowing nitrogen gas. A layer of fluorocarbon oil (PFPE) was then coated onto the as-prepared glass by spin coating (r = 2000 r/min, V = 2 ml, t = 2 min). Finally, the hydrophobic and oleophobic *M-glass-1* was obtained by incubating the PFPE-coated glass in an oven at 180°C for 15 minutes.

Silica nanoparticle coated M-glass surface (M-glass-2) fabrication. After cleaning the original concave roughness treated glass using the same steps, spin coating was carried out to coat a layer of SiO_2 nanoparticle (d = 30 nm, C = 40 wt%) on the glass surface (r = 2000 r/min, V = 1 ml, t = 1 min). Then the silica particle coated glass was dried (T = 200°C, t = 15 min) and sintered (T = 680°C, t = 90 s). Finally, *M-glass-2* surface could be obtained by following the same routine during *M-glass-1* preparation, where PFPE layer was coated.

PTFE surface fabrication. After the smooth glass was cleaned by sonication in ethanol solution and dried in nitrogen flow, PTFE was coated onto the glass surface by spin coating (r = 2000 r/min, V = 1 ml, t = 2 min). After that, the as-prepared PTFE surface was dried in oven (T = 60°C, t = 10 min) and sintered in the muffle furnace (T = 380°C, t = 30 min).

3.3 Electrostatic force microscope (EFM)

EFM mapping was conducted on an atomic force microscope (AFM, MFP-3D, Asylum Research) equipped with conductive tips (AC240TM-R3, Asylum Research). EFM measurements were performed using a two-pass technique[97]. The first scan measured the surface topography by scanning the conductive tip near the surface in a non-contact mode (the van der Waals forces domain). In the second scan, the tip was lifted to a specific height where long-range electrostatic forces dominated. Thereby, the corresponding signals only reflected surface charges. It must be denoted that the tip height is of critical importance to isolate electrostatic forces from topographical influence. In this study, the lift height in the second scan was selected as 50 nm above the sample for all EFM imaging. Detailed reasons for this specific lift height are given in below.

Conductive tips used in this research have an oscillation frequency of $f_0 \approx 70$ kHz, spring constant of $K \sim 3.2$ N m^{-1}, and a quality factor of $Q \sim 200$. To avoid any contribution from the sample topography to the measured EFM phase shift, lift height was calibrated in the following manner: (1) the oscillation amplitude of the tip was reduced to 20 mV in the EFM mode; (2) the unbiased tip was gradually lowered until the EFM phase shift showed the topography of the sample (this region corresponds to a purely topographic signal, ~ 20 nm in this research); (3) the unbiased tip was lifted 30 nm above the region of the topographic signal (at this lift height, EFM phase shift due to topography completely diminishes, confirming a topography-free signal). Therefore, a lift height (Δh) of 50 nm above the sample for all EFM imaging was used to maximize the EFM signal and avoid the topography contribution. In the MFP-3D system (Asylum Research, UK), an attractive force results in an increase in phase, and a repulsive force leads to a decrease in phase.

Unless otherwise specified, the EFM experiment was carried out in a closed fluid cell (Asylum Research, United States) with dry argon atmosphere at a fixed temperature 23°C. The tip bias was set to +3 V, while the scan size was 2 µm. The average time for mounting the charged sample to the EFM was about 1 min.

3.4 Electrical measurement

Liquid drops were generated at the tip of an iron needle (d = 1.0 mm), which was earthed and connected to a glass tube filled with the desired liquid. In this study, the pumping speed was controlled by a syringe pump and was set as 2000 µl/min. The releasing height (Δh) of drops was fixed at 0.68 cm to minimize the frictional charging effect between the falling drop and air [98]. In all measurements, the relative humidity and the environmental temperature were kept at approximately 50% and 23.0 °C, respectively.

After contacting with several drops of liquid, sample surfaces were gently blown by N_2 gas to make sure the liquid was all evaporated. EFM mappings were conducted to measure the surface charge property after liquid-solid CE. It is generally assumed in the literature[38, 99] that blowing nitrogen to completely dry the residual water droplets does not cause significant charge difference on the surface, which has been further verified by EFM measurements in this research (Fig. 3.3). For a pristine insulating surface which is free of triboelectric charges, its EFM phase value should be a constant of 90° (with a tip bias at +3 V). It can be seen from the topography (Fig. 3.3a, Fig. 3.3b) and EFM results (Fig. 3.3c, Fig. 3.3d) in the surface of *M-glass-2* is basically uncharged before and after nitrogen blowing.

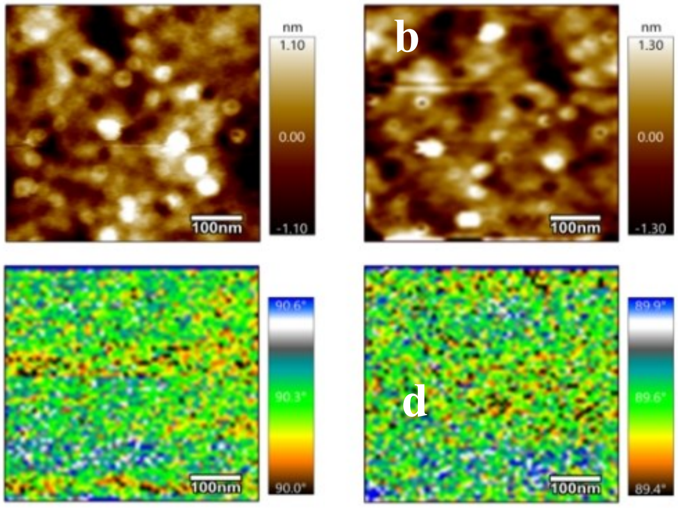

Figure 3.3: Topography (a, c) and EFM image (b, d) of virgin *M-glass-2* surface before and after N_2 blowing

Short-circuit current during liquid-solid CE was also simultaneously measured using a low-noise current preamplifier (Stanford Research System Model SR570), when the liquid drop contacted, bounced, and slid on the surface of the insulating layer.

3.5 Preparation of SLIPS-SE-TENG

The SLIPS was fabricated through dripping and was briefly characterized by its slippery properties. A porous PTFE membrane was selected as the matrix, which features an average pore size of 450 nm and a thickness of 20 μm. This is because PTFE is the most electronegative material in the triboelectric series at ambient conditions.[89, 100, 101] Perfluoropolyether (PFPE) oil (chemical properties in Table 3.1) was chosen as the lubricant because of its unique advantages, such as high wetting affinity with the PTFE membrane, immiscibility with water, high/freezing-temperature stability, low vapour pressure, chemical inertness, and compatibility with various materials.[102]

Table 3. 1 Chemical properties of lubricants

	Density (g/ml)	**Viscosity (25°C， cst)**	**Surface tension (O/A， mN/m)**	**Dielectric constant**	**Vapour pressure (mmHg, 20°C)**
PFPE	1.8	85	12.4	2.9	<5
Silicon oil	0.96	100	39.5	2.3	<5
Mineral oil	0.84	95	31	2.23	<5

To ensure good contact between the PTFE membrane and the glass substrate, the membrane was first wetted by ethanol by using the capillary wicking effect. After the ethanol evaporated, a fixed volume of lubricant oil was dripped onto the membrane to wick into the pores of the PTFE. After the addition of lubricant oil to create the SLIPS-SE-TENG, all the samples were placed horizontally on a flat table for about 12 hours to allow spontaneous impregnation of lubricant before any characterization or measurement. In addition, more reference standards for preparing thermodynamically stable SLIPS can be calculated and found in Table 3.2 and in the literatures. [103, 104]

Table 3. 2 Parameters predicted from surface-energy-based criteria for SLIPS design

Lubricants	$\boldsymbol{S_{ld}}$	$\boldsymbol{S_{ls} + \gamma_1 R}$	$\boldsymbol{\gamma_{dl}}$
PFPE	11.156	-7.49	-109.54
Mineral oil	3.17	-17.01	-105.4

Accordingly, the spreading parameter is defined as $S_{xy} = \gamma_y - (\gamma_{xy} + \gamma_x)$, where $\gamma_x$and γ_y are the surface energies of phases x and y with the surroundings and γ_{xy} is the interfacial energy between phases x and y. In the following discussion regarding SLIPS, the subscript l refers to the lubricant, d is the impinging fluid droplet, and s is the solid. When a single symbol appears in the subscript, it refers to the interface of that phase with its own vapor. Two symbols appearing in the same subscript indicate an interface between two phases, with the symbols referring to the two phases; in the case of the spreading coefficient, the first symbol is the spreading phase, and the second symbol is the reference phase.

If spreading parameter $S_{ld} \geq 0$, the lubricant spontaneously spreads over and “cloaks “the droplet.

$$S_{ld} = \gamma_d - (\gamma_{dl} + \gamma_l) = \gamma_d^{LW} + 2\sqrt{\gamma_d^+\gamma_d^-} - \gamma_l^{LW} - 2\sqrt{\gamma_l^+\gamma_l^-} - \gamma_d^{LW} - \gamma_l^{LW} + 2\sqrt{\gamma_d^{LW}\gamma_l^{LW}} -$$

$$2\sqrt{\gamma_d^+\gamma_d^-} - 2\sqrt{\gamma_l^+\gamma_l^-} + 2\sqrt{\gamma_d^+\gamma_l^-} + 2\sqrt{\gamma_l^+\gamma_d^-} \qquad (3\text{-}1)$$

If $S_{ls} + \gamma_1 R > 0$, the lubricant does infuse in the solid structures in the presence of the impinging fluid, which result in failure of the SLIPS.

$$S_{ls} + \gamma_1 R = \gamma_s - (\gamma_{ls} + \gamma_l) + \gamma_{lR} = \gamma_s^{LW} + 2\sqrt{\gamma_s^+\gamma_s^-} - \gamma_l^{LW} + 2\sqrt{\gamma_l^{LW} - \gamma_s^{LW}} - 2\sqrt{\gamma_l^+\gamma_l^-} -$$

$$2\sqrt{\gamma_s^+\gamma_s^-} + 2\sqrt{\gamma_l^+\gamma_s^-} + 2\sqrt{\gamma_s^+\gamma_l^-} + (R-1)\left(\gamma_l^{LW} + 2\sqrt{\gamma_l^+\gamma_l^-}\right) \quad (3\text{-}2)$$

If $\gamma_{dl} > 0$, the interface between the lubricant and the impinging fluid increases its surface area indefinitely to minimize energy, ultimately resulting in the miscibility of the two fluids;

$$\gamma_{dl} = \gamma_d^{LW} + \gamma_l^{LW} - 2\sqrt{\gamma_d^{LW}\gamma_l^{LW}} + 2\sqrt{\gamma_d^+\gamma_d^-} + 2\sqrt{\gamma_l^+\gamma_l^-} - 2\sqrt{\gamma_d^+\gamma_l^-} - 2\sqrt{\gamma_l^+\gamma_d^-} > 0 \quad (3\text{-}3)$$

Construction principle of SLIPS

- The substrate should be porous, rough or swellable in order to trap lubricants by combining van der Waals forces, and, if the surface is porous or rough, by capillary forces.
- The lubricant must penetrate, wet and adhere to the structure in the air environment, otherwise the substrate would remain dry.
- The substrate must be preferentially wet by the lubricant rather than by the working droplets, thereby ensuring that the latter float on the lubricant interface. In addition, the working fluids should not spread over the SLIPS to ensure that the working fluids can easily slip off.
- The lubricant should be immiscible and non-reactive with the working fluid to maintain a stable lubricant layer.

After the Al electrode was arranged on the SLIPS surfaces of the above-mentioned materials, used the single electrode, the SLIPS-SE-TENG device fabrication was complete. Since the oil layer does not allow a stable electrode installation, we used a fixing method that is illustrated in Fig. 3.4.

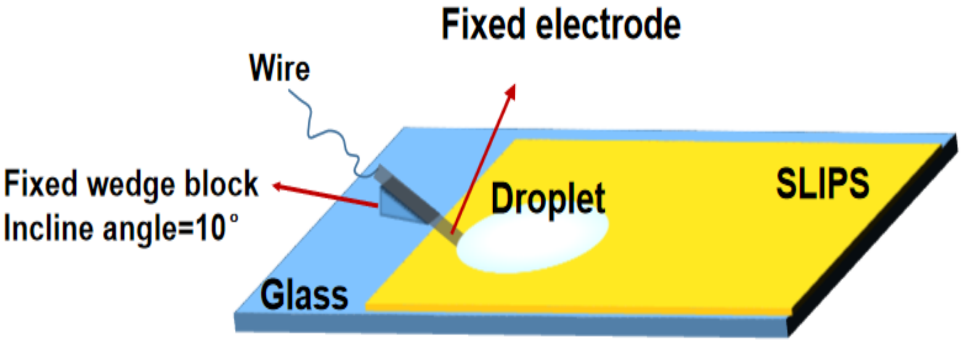

Figure 3.4: Electrode installation diagram

3.6 Characterizing infused lubricant thickness

The lubricant's thickness on the SLIPS surface was characterized using contact mode force spectroscopy on an MFP-3D AFM (Asylum Research) using Multi75Al-G probes (Budget Sensors, resonant frequency: 75−80 kHz, k: 1−7 N/m). Probes with a relatively low force constant were used to ensure a large sensitivity at low forces. The trigger point (the force at which the AFM reverses direction) was set low (at approximately 4 nN) to avoid plastic deformation of the substrate. Datasets were collected using force mapping. Typically, datasets were collected on 2 × 2 μm^2 areas with a resolution of 32 × 32 pixels. The force curves were exported to ASCII and the approach portion of the curve was analyzed using a custom python script (Appendix A). As this manner of data collection is much slower than standard AFM collection time, the scan sizes, speeds, and resolution were optimized to reduce any distortion due to piezo or sample drift. The principle of oil layer thickness detect was described as below: briefly, at large separations (e.g., distance x=0nm), the tip and surface are not interacting and there is no deflection of the cantilever (region ①). When the AFM tip contacts the surface of the lubricant oil surface, there is an abrupt negative deflection, a so-called jump-in (point ②), because of an attractive capillary effect from a meniscus forming as the lubricant wets the tip, drawing it down. This negative deflection continues as the tip continues moving through the lubricant oil (region ③) until the tip makes hard contact with the substrate (seen as a positive deflection, point ④). By taking the difference in distance between point ② and point ④, the thickness of the lubricant is mapped. Representative approach portion of an AFM meniscus force curve as shown in Fig. 3.5.

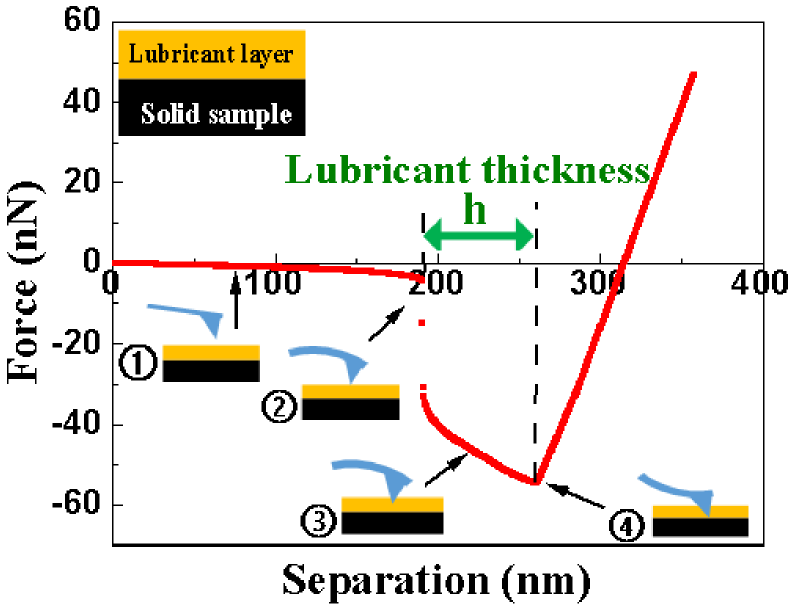

Figure 3.5 Force Map Lubricant Thickness Analysis

3.7 Characterization and electrical measurement

The dynamic behavior of the water droplet was recorded by a Photron FASTCAM SA4 at a rate of 10000 frames per second and analyzed by self-written MATLAB code (Appendix B). A low-noise current preamplifier (Stanford Research System Model SR570) was used to measure the electrical outputs of TENG. If not specified, otherwise, the substrate tilt angle and the release height of the water droplet were fixed at 35° and 4 cm, respectively. All the experiments were carried out at room temperature (23°C) and ambient relative humidity of 40%. To test the behavior of TENGs at low temperatures, samples were stuck to a thermoelectric cooling stage which was used to precisely control the temperature with a cooling rate of around 8 °C/min. Contact angle hysteresis (CAH) was measured using a tensiometer (Fisher scientific). A 5 μL drop was initially dispensed on the surface. 10 μL was added to the drop to measure the advancing angle and 10 μL was removed to measure the receding angle. The presented data are an average of three measurements. The optical transmittance was measured using a Perkin Elmer Lambda 35 UV-VIS spectrometer.

3.8 Adhesive force mapping by AFM

Adhesion force mapping was carried out using an untreated silicon tip mounted on a silicon nitride cantilever (Scanasyst-Air, Bruker, USA; cantilever stiffness 0.5 N/m) in commercial MFP-3D AFM system (Asylum Research, Santa Barbara, CA). More cantilever details are given in the Fig. 3.6. A sinusoidal driving voltage applied to the z-piezo is used to oscillate the cantilever position at frequencies ranging from 10 to 300 Hz. This led to intermittent contact between the probe tip on the cantilever and the sample surface. The frequency of z-piezo modulation was lower than the resonance frequency of the cantilever. For each force curve, the maximum deflection signal, read on the photodetector, is used to calculate the Z height measured by the Z sensor. Maximum force is calculated in real-time and is used as error signal for the Z feedback loop. While the probe position is driven (sinusoidal wave) in the Z-axis, the sample is moving underneath it in a raster pattern in the X-Y plane. One force distance curve could be obtained in one period of the z-piezo modulation. Desired signals, such as pull-off (adhesive force), and jump-in (attractive force) could be measured by using sample and hold circuit with suitable time windows. Deflection of the cantilever was monitored by the optical lever method. The adhesive force mappings were performed in air (humidity, 44%) at room temperature (~ 23 °C). Brighter contrast in an adhesive force map corresponds to a higher adhesive force.

SCANASYST-AIR

Geometry
▼ Triangular

Tip Radius (nm)
Nom: 2
Max: 12

Frequency (KHz)
Nom: 70
Min: 45
Max: 95

Length (µm)
Nom: 115
Min: 100
Max: 130

Spring Const (N/m)
Nom: 0.4
Min: 0.2
Max: 0.8

Width (µm)
Nom: 25
Min: 20
Max: 30

Figure 3.6: Commercial SCANASYST-AIR probe images and relative parameters (product images and information provided by Bruker, USA)

Chapter 4

Curvature effects on liquid–solid contact electrification

Water, as an important resource, can not only sustain life, but also provide abundant energy. In 2013, Lin *et al*. [105] first reported a triboelectric nanogenerator (TENG) based on the liquid-solid contact electrification, which later on was further developed by Wang's group [1, 37, 106-109]. This kind of device can convert the kinetic energy of liquids (e.g., raindrops, ocean waves) into electric energy in an efficient and sustainable manner. One of the main working principles for TENG is contact electrification (CE), where two distinct materials become charged when in contact with each other. Upon contact, triboelectric charges could be generated due to the work function or contact potential difference [110, 111], which is commonly explained by the surface states model [112, 113] or electron-potential well model [72, 111, 114].

Studies have shown that surface characteristics of the triboelectric materials have important effects on the power generation performance of TENG [34, 71]. For example, Xu *et al*. [72] indicated that CE of two pieces of chemically identical materials results in concave surfaces being positively charged and convex surfaces being negatively charged. The authors explained that surfaces with different curvatures have different surface energies due to the stretching or compressing of surface molecules [73].

Although the findings of curvature effect in macroscale is essential for understanding CE, it would be of great scientific value to explore this phenomenon on a smaller scale. In the real world, solid surfaces are not always molecularly smooth. Indeed, nanoscale surface curvatures commonly exist everywhere on a rough surface. Therefore, understanding how nanoscale surface roughness influence local triboelectric charges could broaden the applicability of curvature effect in more universal scenarios.

It is of critical important to choose the appropriate technique that can collect data on both surface curvature and local charge density conveniently and simultaneously. Kelvin probe force microscopy (KPFM) is one of the most widely used techniques to characterize the surface charge density profile in nanoscale[15, 17, 115]. However, the range of surface potential measurement using conventional KPFM (e.g., MFP-3D, Asylum Research) is from -9 V to +9 V, which makes it difficult to determine the surface potential in many cases after CE. For example, Zhan *et al.*[98] measured the surface potential of PTFE surface after CE by an electrostatic voltmeter. The authors indicated that the absolute value of the surface potential on the impact point exceeds 400 V after five consecutive water drops. Fortunately, there are still some analytical methods that can be used for high potential surfaces. Recently, Lin *et al.* proposed a novel "scanning TENG" technique, which uses a scanning triboelectric nanogenerator as a nanoscale probe for measuring the local surface charge density on the dielectric film [40] It can effectively eliminate the interference generated using AC bias in the surface charge density measurement. Meanwhile, the electrostatic force microscope (EFM) is also an effective way to analyze the surface charge density, especially for insulating surfaces with relatively high surface potential after CE. More importantly, EFM not only can provide high-resolution information regarding the uncompensated triboelectric charges on a rough surface but also is easier to operate than other methods mentioned above. Therefore, the EFM technique was applied in this study to quantify the relationship between surface curvature and as-generated triboelectric charges.

In this chapter, we designed surfaces with different nanoscale curvatures (concave-convex) and investigated the generation of triboelectric charges in nanoscale via electrostatic force microscope (EFM) scanning. The working principle of EFM can be found in the literature [116-118]. We assume that the liquid surface is smooth and flat when in contact with a solid surface [119], and thereby the differences of local surface charges should only be attributed to the change of surface curvature. Based on the research findings, a surface states model was proposed to explain the CE mechanism between drops and different curvature surfaces with identical chemistry properties. At last, we tested the performance of a solid-liquid TENG in a contact-separation mode using surfaces with different curvature profiles to illustrate the impact of this fundamental understanding on the future development of TENGs.

4.1. Curvature effect on charge generation

Electrostatic force microscope (EFM, Fig. 4.1a) is a powerful equipment to explore electrical properties of dielectric materials at nanoscale. CE is achieved by the contact of water droplets on the surface, as shown in Fig. 4.1b. It should be noted that all the pristine insulating surfaces were first scanned by EFM, and it could be confirmed that the surface is free of triboelectric charges before CE tests, as shown in Fig. 4.1c and 4.1d.

Electrostatic force microscope (EFM) is a powerful equipment to explore electrical properties of dielectric materials at nanoscale. For a pristine insulating surface which is free of triboelectric charges, its EFM phase value should be a constant of 90° (with a tip bias at

+3 V), as shown by the black solid curve in Fig. 4.1c. If the surface becomes negatively charged after liquid-solid CE, it will result in an attractive electrostatic force to the positive-charged biased tip. Consequently, the measured phase value increases under the same frequency (ω0), indicating a phase value (φ) greater than 90°. For the same reason, EFM phase value is less than 90° for positively charged surface [120].

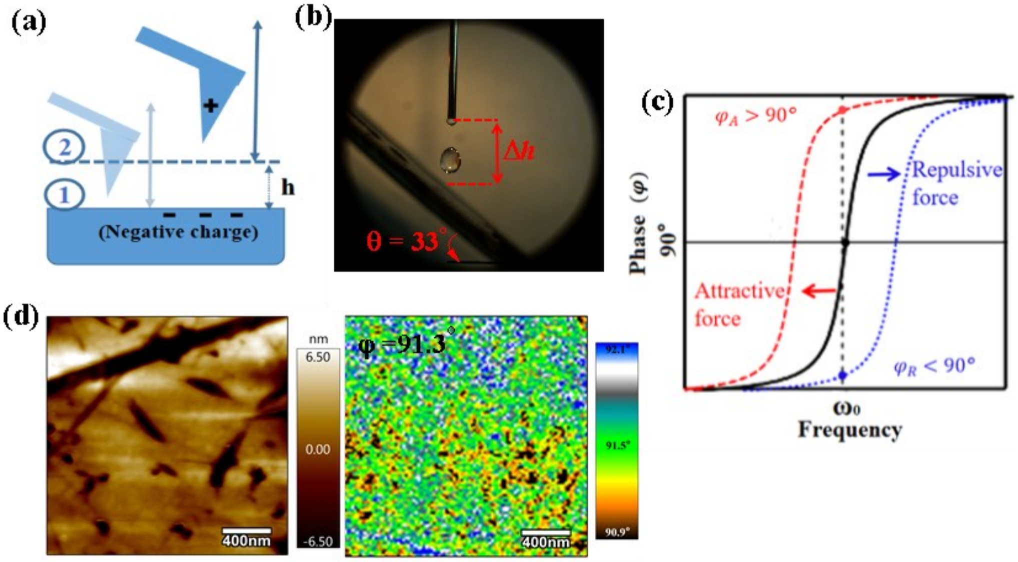

Figure 4.1: Schematic diagram of (a) EFM two-pass scanning model, (b) liquid-solid surface contact model, and (c) principle of EFM phase value. (d) EFM images of virgin *M-glass-1* surface without CE: surface morphology (left) and EFM phase distribution (right).

Pristine *M-glass-1* surface was first characterized by their topography and EFM phase before CE, and the results are shown in Fig. 4.1d. The EFM phase of the uncharged *M-glass-1* surface was stabilized at around at 91.3°, which slightly deviated from the phase value (φ_0 = 90°) at the resonance frequency (ω_0). This marginal shift of the EFM phase value was most likely due to the image charge (q_i) generated by the biased tip (+3 V, charged q_0), which led to an charge-induced charge interaction (yielding an attractive electrical force which is proportional to q^2) between the tip and the insulating surface [121]. Despite this inevitable but marginal phase shift, the virgin surface was electrically neutral. Similarly, the EFM tests are performed on *M-glass-2*, PTFE and parafilm virgin surfaces before CE experiment, respectively. The phase value is about 90°, indicating that all surfaces are electrically neutral at the beginning.

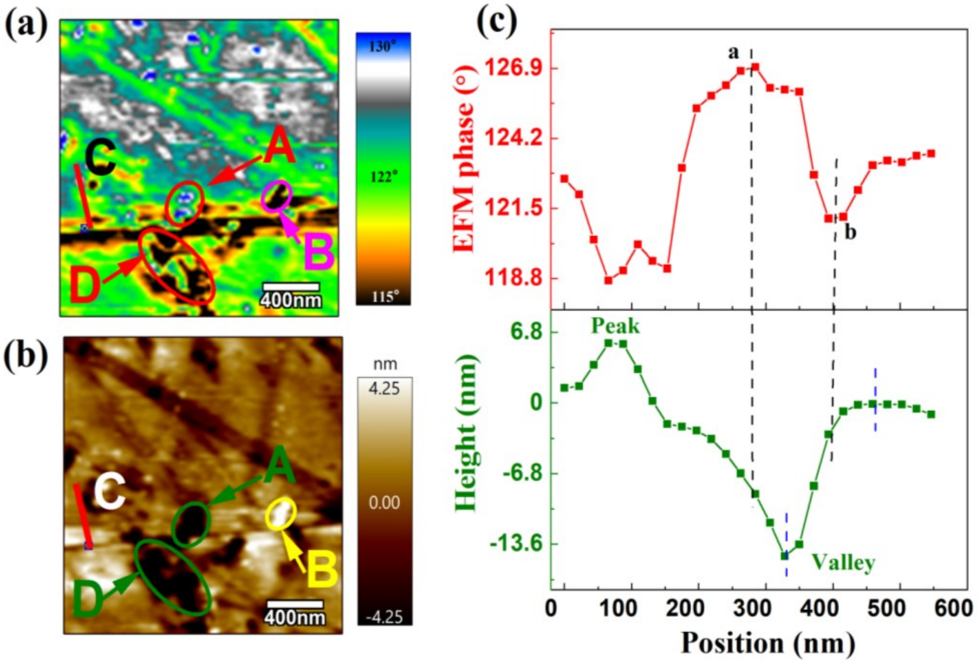

Figure 4.2: (a) EFM phase distribution and (b) morphology of *M-glass-1* surface after CE with water drops. (c) EFM phase value and AFM topographical height function with surface positions.

M-glass-1 surface showed significant changes in EFM phases after CE of five consecutive water drops, as demonstrated in Fig. 4.2a. The EFM phase value of the *M-glass-1* surface after CE became much greater than 90°, which means that there was an attractive electrostatic force between the water-contacted surface and the positive-charged biased tip.

Therefore, one could identify that the surface of *M-glass-1* was negatively charged after CE with water drops. These results are consistent with previous reports [19, 122, 123].

Interestingly, there appears to exist a general correlation between the shifts of EFM phase and the surface morphology, when comparing the EFM phase (Fig. 4.2a) and surface morphology distribution (Fig. 4.2b) after CE. For example, region *A* was a "valley" with a low height profile (~ -4.25 nm). Its corresponding EFM phase value was relatively greater than its surroundings (~ 130°). An opposite example could be found in region *B*, where the local "peak" led to low EFM phases. To evaluate the relationship between local morphology and triboelectric charge, the profiles of height and EFM phase were analyzed across the line "*C*" in Fig. 4.2b, which went through a peak and a valley in turn. Their comparison is shown in Fig. 4.2c. Obviously, EFM phase values around the peak region were much lower than those around the valley region. In other words, fewer triboelectric charges were generated at the peak than in the valley. Since the EFM phase on the virgin *M-glass-1* surface was mostly homogeneous regardless of local morphology (EFM variation < 2°) (Fig. 4.2d), it is thereby deduced that the differences of EFM phase values should be attributed to the impact of local morphology on water-solid CE, even if the microstructures on the surface were in nanoscale sizes.

However, it is also recognized that the optimum EFM phase values did not match up with the exact peak and valley points in the height curve (points *a* & *b* in Fig. 4.2c), despite the intuitive hypothesis that a rough correlation might exist between local heights and EFM phases. Such a mismatch hints that morphology defined by height is not the main determinant of the strength of triboelectric charges in nanoscale. Indeed, a more refined comparison between the height and EFM phase reveals that their relationship is sometimes suspectable. Using Figs. 4.2a & 4.2b as examples again, region D was obviously the basin of this surface, but its corresponding EFM profile was mixed by low to intermediate phases, instead of being a uniform region with high phase degrees. This abnormal result further convinces us that it is insufficient to describe how triboelectric charges are affected by nanoscale morphology as a function of local height.

In this study, we propose that the strength of triboelectric charges after liquid-solid CE is correlated with surface morphology through local curvature profiles. Previously, Wang's group reported that curvature could influence the generation of triboelectric charge between two surfaces made of identical materials [72, 73]. By preparing a contact-separation mode triboelectric nanogenerator using two pieces of an identical material, they pointed out that the direction of charge transfer during contact-electrification relied on its dependence on curvatures of the sample surfaces. However, their results were obtained using surfaces in macroscale sizes (i.e., a couple of centimeters) and did not go deep into nano-level. Based on our observations in Fig. 4.2, we hypothesize that such a curvature effect on triboelectric charges could be extended in nanoscale sizes, e.g., the nano-curvatures caused by non-smooth surfaces.

Curvatures were calculated from the morphology height in Fig. 4.2c. From the mathematical definition, the concave-convex function is determined by the curvature, as shown in Fig. 4.3. Here, the functional relationship between surface topography height (H) and position (x) is assumed to be H = f(x), and the curvature (K)-position(x) function with the relationship of K = g(x) can be derived according to the curvature equation:

$$\mathrm{K} = \frac{\mathrm{H}''}{(1+\mathrm{H}'^{2})^{3/2}} \qquad (4\text{-}1)$$

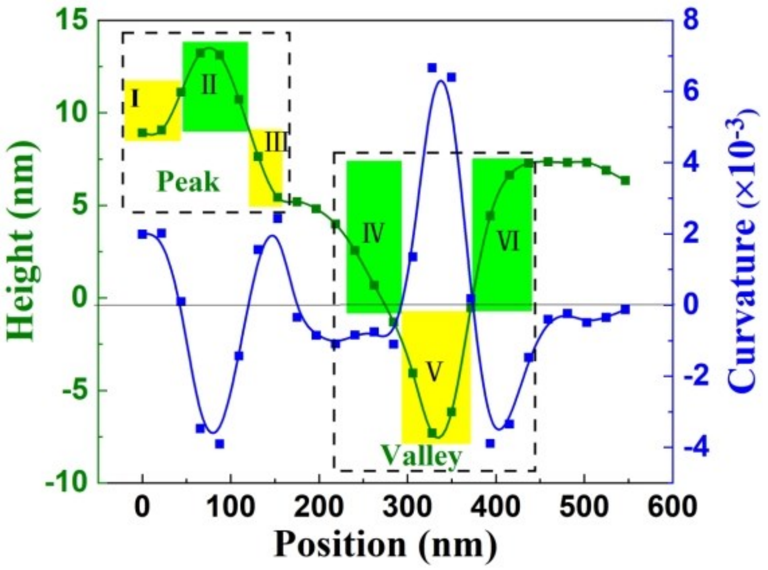

Figure 4.3: Curvature transformation from the height difference according to curvature equation.

Fig. 4.4 shows the comparison between the curvature profile and its corresponding EFM phases after liquid-solid CE. The surface topography is defined as convex when its curvature has a positive value, while is referred as a concave surface when the curvature is negative. The curvature of a flat surface is zero. When expressed by curvatures, surface topography appeared to have a decent connection to the EFM phase, as shown in Fig. 4.4a. EFM phase tends to decrease on concave surfaces but increase on convex surfaces with negative curvature. For example, the EFM phase increases gradually from *a* to *b* in Fig. 4.4a (top). The same local area was shown to display a negative curvature from position *a′* to position *b′* in Fig. 4.4a (bottom). On the contrary, the EFM phase tends to decrease (from *b* to *c*) once the corresponding local curvature turns positive (from *b′* to *c′*). Among them, points *a′*, *b′*, and *c′* are the inflection points (curvature = 0), which perfectly matched the optimum value of the EFM phase (at the positions of a, b, and c, respectively).

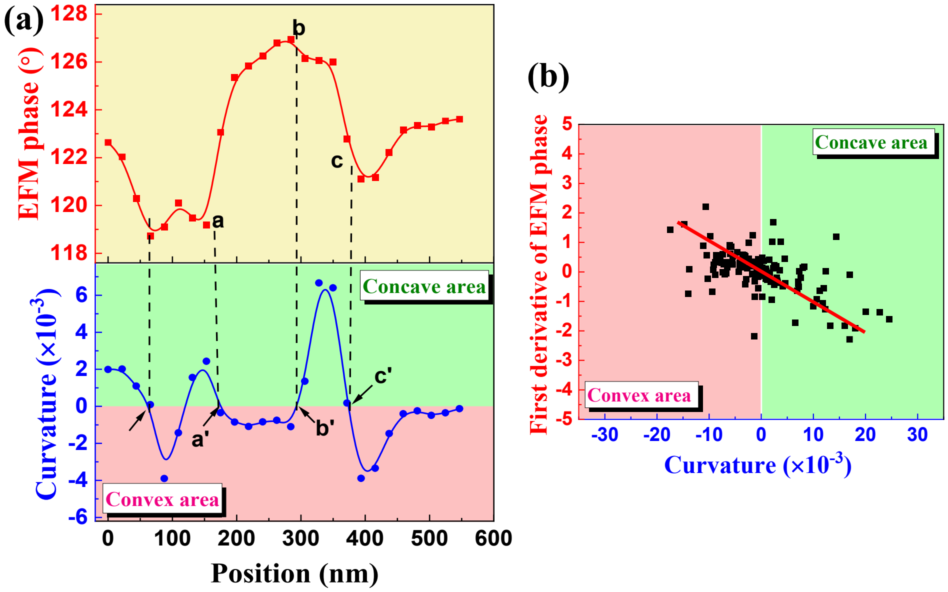

Figure 4.4: (a) Curvature and EFM phase changes at different surface positions; (b) First derivative of EFM phase as a function of curvature. The solid line is used to guide the eyes.

The effect of curvature on triboelectric charges was further analyzed over the whole testing surface. Different areas were selected arbitrarily on the insulating surface, while the local site curvature was plotted against the first derivative of its corresponding EFM phase. Fig. 4.4b reveals a statistical conclusion that the first derivative of the EFM phase is generally greater than zero for convex surfaces, while is typically less than zero for concave surfaces. That is to say, the EFM phase of the convex surface increases monotonously, whereas that of the concave surface decreases monotonously after CE. Besides, a statistical trend was found that smaller curvature value would typically lead to a higher charge rate of negative charges after CE.

To further explore the influence of surface curvature on the charge transfer capacity after liquid-solid CE, EFM analyses were also conducted on different insulating surfaces (e.g., PTFE and parafilm), or using non-polar solvents (e.g., heptane and decane). These results verified the general applicability of the above conclusions (Fig. 4.5). It is thereby concluded that the charge transfer ability after CE is related with the surface curvature at the nanoscale. For local regions with negative curvature (convex area), it is much easier to be charged by liquid drop after CE than the surface with positive curvature (concave area).

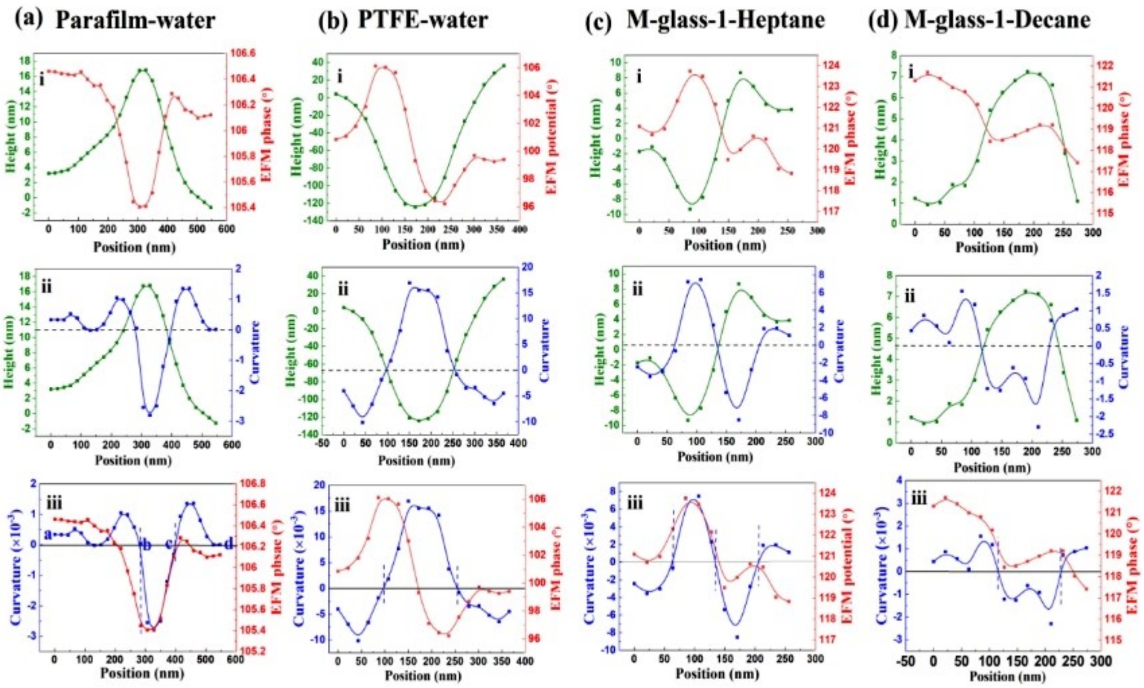

Figure 4.5: Relationship between morphology and EFM phase distribution of (a) parafilm (b) PTFE surface after CE with water droplets; and *M-glass-1* surface contact electrification with (c) heptane and (d) decane.

Importantly, the difference in droplet size had no apparent effect on the relationship of curvature to contact electrification (Figs. 4.6a & 4.6b). That is to say, the electron-accepting ability of the convex region (curvature < 0) on the solid surface is stronger than that of the concave region (curvature > 0), and the EFM phase value gradually increases. as shown in Figs. 4.6c & 4.6d. At the same time, the experimental results in Fig. 4.6e also show that the falling height of the drop also have no significant effect on the rate of electron transfer at the solid-liquid interface. However, it is worth noting that either increasing the diameter of the droplet or the droplet height can increase the contact area of the liquid-solid interface, thereby increasing the total amount of electron (or ion) transfer at the solid-liquid interface (Fig. 4.6a & 4.6b).

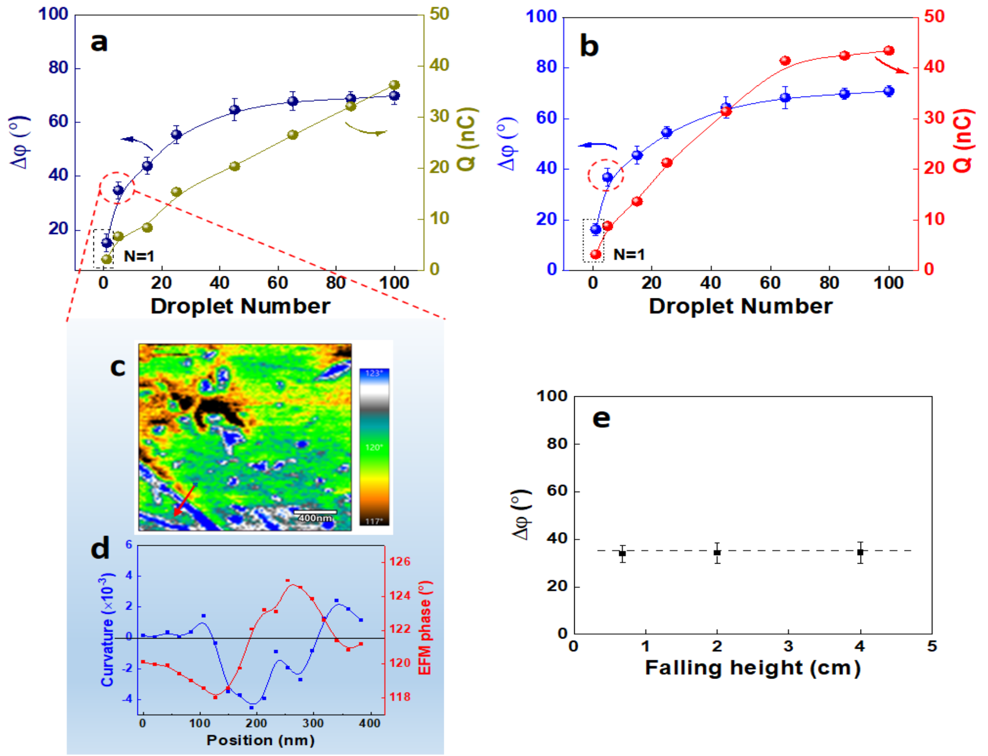

Figure 4.6: EFM phase difference and accumulated charges after multiple water droplets, (a) 0.014 mL per water drop and (b) 0.037 mL per water drop, separated from the end of the solid surface and then fell into a Faraday cup. (c) EFM phase distribution image and (d) curvature-EFM phase relationship at different surface positions after contact electrification (0.014 mL per water drop). (e) The relationship between EFM phase difference and droplet falling height (0.014 mL per water drop).

4.2. Curvature effect on charge emission

Once the liquid drop separates from the insulating layer after liquid-solid CE, the electrons generated on the insulating surface will be thermodynamically emitted to the environment [124]. Since nanoscale morphology has readily been demonstrated to affect the generation of triboelectric charges, making the charge density inhomogeneous over the surface, we believe that the curvature might also play a role on charge emission. Therefore, EFM was used to explore the curvature effect on the charge emission in the argon atmosphere at a fixed temperature of 140 °C.

It is first assumed that the cantilever of EFM is a spring vibrator (Fig. 4.7a). When there is an electrostatic force between the tip and the surface, electrostatic force gradient ($F' = \partial F/\partial Z$) changes the effective spring constant *K* [125]. Hence, the driving frequency (ω_*) of the tip can be derived from its resonance frequency (ω_0):

$$\omega_* \approx \omega_0 \left(1 - \frac{F\prime}{2K}\right) \qquad (4\text{-}2)$$

Based on such an assumption, the detected shift of EFM phase ($\Delta\varphi$) should follow the exponential decay:

$$\Delta\varphi_i = e^{-SAt}\Delta\varphi_0 \qquad (4\text{-}3)$$

where *A* is the surface area and *S* is constant for a specific material, *t* is the decay time, *i* represents distinct points in time. Detailed derivation and interpretation are provided as below:

It should be noted that whether the phase value measured by EFM can be directly used to quantify the decay process of electrons still needs a careful verification. Here, we assume that the AFM cantilever and tip together act as a simple driven harmonic oscillator, the resonance frequency of an oscillator

$$\omega_0 = \sqrt{\frac{K}{m^*}} \qquad (4\text{-}4)$$

The EFM measurement process is analogous to the movement of a spring vibrator when there is no external force. The driving frequency (ω_*) of the spring vibrator is equal to the resonance frequency of the cantilever (ω_0). When there is an electrostatic force between the tip and the surface, the force gradient ($F' = \frac{\partial_F}{\partial_Z}$) changes the effective spring constant *K*. Hence, the driving frequency of the tip can be obtained from the resonance frequency:

$$\omega_* = \sqrt{\frac{K-F\prime}{m^*}} = \omega_0\sqrt{1-\frac{F\prime}{K}} \approx \omega_0\left(1-\frac{F\prime}{2K}\right) \qquad (4\text{-}5)$$

Applying Taylor series expansion, the square-root term in Eq. B-3 can be approximated into the following form: $\sqrt{1-\frac{F\prime}{K}} \approx 1-\frac{F\prime}{2K}$. According to the mathematical relationship between vibration frequency (ω) and EFM phase value (φ)[24], one could derive the following equation:

$$\tan\varphi = \frac{\omega_0\omega_*/\mathrm{Q}}{\omega_0{}^2-\omega_*{}^2} \qquad (4\text{-}6)$$

where *Q* is the quality factor of the cantilever. Among them, $\omega_* = \omega_0\sqrt{1-\frac{\mathrm{F}\prime}{\mathrm{K}}}$ and $\mathrm{F}' \ll \mathrm{K}$.

Hence:

$$\tan\varphi = \frac{\omega_0{}^2\left(\sqrt{1-\frac{\mathrm{F}'}{\mathrm{K}}}\right)/\mathrm{Q}}{\omega_0{}^2-\omega_0{}^2\left(1-\frac{\mathrm{F}'}{\mathrm{K}}\right)} = \frac{\sqrt{\left(1-\frac{\mathrm{F}'}{\mathrm{K}}\right)/\mathrm{Q}}}{\frac{\mathrm{F}'}{\mathrm{K}}} \approx \frac{\mathrm{K}}{\mathrm{QF}'} \qquad (4\text{-}7)$$

The geometric relationship is shown in following illustration,

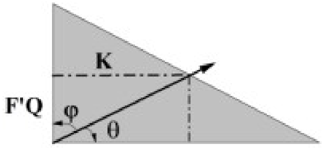

which gives us the relationship that $\tan\theta = \frac{\mathrm{QF}'}{K}$. For a small angle θ, $\tan\theta$ could be approximated into the following:

$$\tan\theta = \frac{\mathrm{QF}'}{K} \approx \theta \qquad (4\text{-}8)$$

so,

$$\varphi = \frac{\pi}{2} - \theta \approx \frac{\pi}{2} - \frac{\mathrm{QF}'}{K} \qquad (4\text{-}9)$$

and the EFM phase shift becomes:

$$\Delta\varphi = \frac{\pi}{2} - \frac{\mathrm{QF}'}{K} - \frac{\pi}{2} = -\frac{\mathrm{QF}'}{K} \qquad (4\text{-}10)$$

Hence, the relationship between the EFM phase value and the electrostatic force gradient can be obtained as below:

$$\Delta\varphi = -QF'/K = CF' \qquad (4\text{-}11)$$

where *C* is a constant ($\mathrm{C} = -\mathrm{Q}/\mathrm{K}$). Besides, it should be noted that with a fixed EFM scanning distance (Δh = 50 nm), the electrostatic force gradient *F' is* proportional to the electric force F between the tip and the insulating surface after CE. Therefore, it is reasonable to propose that $\Delta\varphi \propto F' \propto F \propto Q_N$, where Q_N is the total negative charge in its insulating surface after CE. To estimate whether the charge decays are consistent with the electron thermionic emission model, the measured Q_N values are fitted according to the thermionic emission equation

$$Q_N = e^{-SAt} Q_{N_0} \qquad (4\text{-}12)$$

where A is the surface area and S is constant for a specific material, t is the decay time.

Therefore, if the phase change describes the decay process of surface charge is reasonable, the Eq. 4-3 in the main text should be valid.

As shown in Fig. 4.7b, experimental results strongly support our theory that the EFM phases decayed exponentially over elapsed time (coefficient of determination $R^2 > 0.99$). After the same decay period, the EFM phase change ($\Delta\varphi_i$) of the surface after CE with the water drops is significantly lower than that of the same surface contacting with the oil drops. On the other hand, the amount of residue charges was obviously higher in the case of water-solid CE (φ_E = 112°) compared to oil-solid CE (φ_E = 102°), as shown in the inset picture in Fig. 4.7b. The reason for this difference is that there are ions (e.g., H^+ and OH^-) that exist in the water drops, but non-polar solvents are completely excluded of extra ions. After CE, part of electrons remaining on the insulating surface will be thermodynamic emitted except for the adsorbed ion (e.g., OH-), which would adsorb stably on the surface throughout [34, 38, 99, 126, 127].

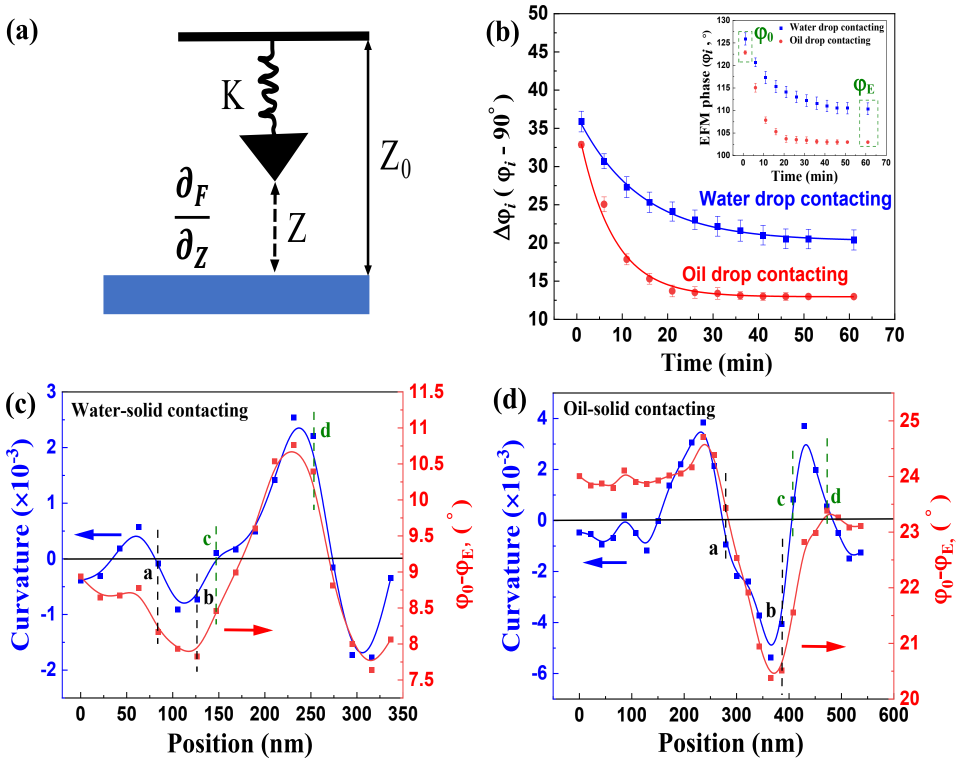

Figure 4.7: (a) Schematic diagram of a simple harmonic oscillator (EFM cantilever and tip). (b) Thermodynamic emission decay of the surface charge on the insulating layer (φ_0 refers to the initial state and φ_E refers to equilibrium state). Relationship between the surface curvature and the EFM phase shift in (c) water-solid CE and (d) oil-solid CE.

Interestingly, local curvature also showed a significant influence on the dissipation of triboelectric charges. Thermodynamic emission of surface electrons is assessed by their EFM phase shift (φ_0 - φ_E) over time. EFM phase shifts are displayed in Figs. 4.7c & 4.7d for the cases of contacting water drop and contacting oil drop, respectively. Differently from the curvature effect on triboelectric charge generation, the values of EFM phase shift tend to decrease on convex region (e.g., negative curvature region a − b) and start to increase once the surface turns concave (e.g., positive curvature region c − d). This means that the charges on the concave surface are more likely to be emitted into the atmosphere than those on the convex surface. Such a conclusion is universal for the electron emission regardless the type of liquid. It is worth pointing out that this curvature effect is probably also applicable to the contact electrification between the same materials at the nanoscale (Fig. 4.8), which is consistent with the previously published results[72]. On the macro level, Xu *et al*. [72] have fully revealed the basic principle of tribo electrification of the same material, which is due to the curvature effect. However, there is no relevant research at the nano level. According to the preliminary results, it is possible that the same material also follows this curvature effect at the nanometer level (take the concave surface as an example, as shown in Fig. 4.8). After CE with the convex surface *M-glass-2*, the concave surface (*M-glass-1*) becomes positively charged (EFM phase is below 90°).

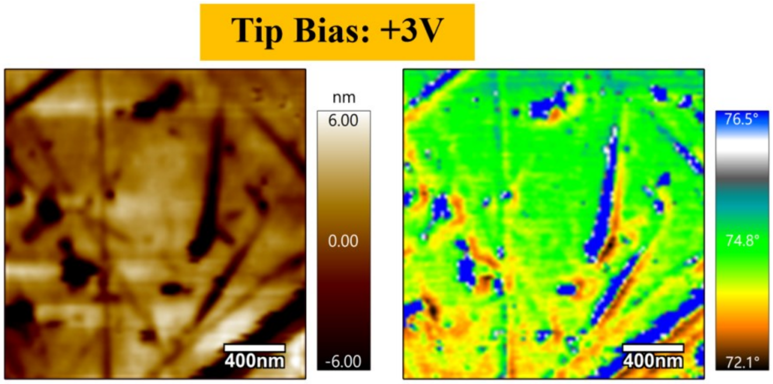

Figure 4.8: Topography and EFM phase image of the *M-glass-1* (Concave) surface after CE with 20N impacting force at room temperature (~23 °C)

4.3 Mechanisms of curvature effect

A surface state model is proposed to obtain a deeper understanding of the curvature effect on the generation and emission of triboelectric charges. Fig. 4.9 provides a schematic illustration of the electron transfer process between liquid and insulating surface with distinct curvature characteristics. First, it is important to point out that the curvature difference could result in different surface energy [72]. Before liquid contact, concave regions ($E_n^{C>0}$, curvature > 0) readily contain a higher energy level than the flat surface ($E_n^{C=0}$), whereas convex surface ($E_n^{C<0}$) configurations lead energy shifting to lower levels, as shown in Fig. 4.9a. In other words, the relationship between the three surface energy levels is $E_n^{C>0} > E_n^{C=0} > E_n^{C<0}$. To some extent, this is similar to a well-studied phenomenon that charge density in conductors is greater at regions of large curvature and lower in small curvature regions [128].

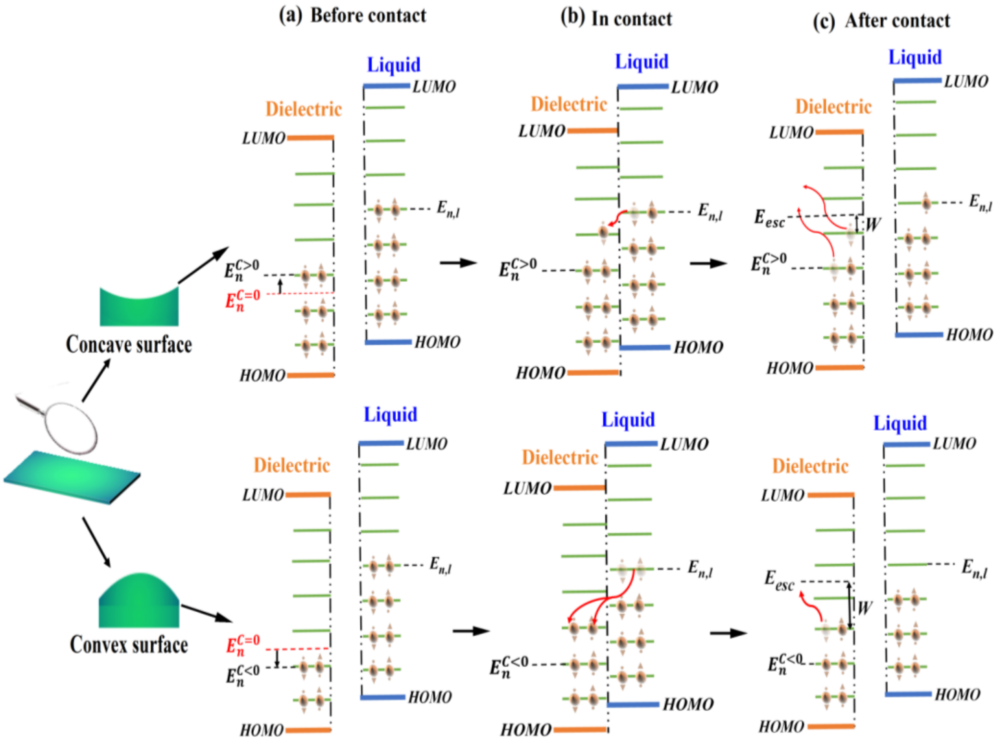

Figure 4.9: Mechanism of contact electrification between liquid and dielectric surfaces of different curvatures. Charge transfer between the dielectric and liquid with different surface curvatures (depicted by green shapes) are explained by the surface states models for (a) before contact, (b) in contact, and (c) after contact. (*LUMO*, lowest unoccupied molecular

orbital; $E_n^{C>0}$, $E_n^{C=0}$and $E_n^{C<0}$ represent the neutral level of surface states for concave area (curvature > 0), flat area (curvature = 0) and convex area (curvature < 0) of the insulator; $E_{n,l}$, the neutral level of surface states of liquid drop; E_{esc}, minimum energy to trigger electron escape from the surface; W, energy barrier; *HOMO*, highest occupied molecular orbital.)

Due to the natural characteristics in the energy level for convex and concave surfaces, the energy difference between convex surface ($E_n^{C<0}$) and the liquid drop ($E_{n,l}$) is more significant than that between concave surface ($E_n^{C>0}$) and liquid. When the liquid drops in contact with the solid surface (Fig. 4.9b), greater differences in surface energy level would cause more electrons to be transferred from the high energy level surface (e.g., liquid drop) to the low energy level surface (e.g., dielectric). Consequently, convex regions can accommodate more electrons during CE. In other words, the number of electrons being transferred to the convex surface (Fig. 4.9b-bottom) is more than that to the concave surface (Fig. 4.9b-top), thereby resulting a higher EFM phase value and higher triboelectric charge density after CE.

Fig. 4.9c shows the charge emission process at a fixed temperature T after the liquid drop left the insulating surface. During this process, the energy fluctuations of electrons are in the order of magnitude of several kT. When the energy barrier W of maintaining electrons in the orbitals is lower than the energy fluctuation, part of electrons would hop out of the solid surface. These escaped electrons either go back to the orbitals of the material where they came from, or emit into atmosphere [114, 129]. Since concave surface has a higher surface state than the convex surface, electrons only need a smaller fluctuation to surpass the energy barrier and escape into surroundings. This is most likely the main reason why the concave surface emits electrons easier than the convex surface. Besides, this model also clarifies the existence of residue charges. Part of the electrons generated from CE can be maintained on the insulating surface when the energy barrier W has a higher order of magnitude than several kT. If the surrounding temperature increased further, i.e., increasing the kT value, more residual electrons would emit from the insulating surface.

4.4 TENG performance

In the previous sections, we have demonstrated the curvature effect on the liquid-solid CE in nanoscale. Owing to these results and fundamental understanding, it is reasonable to assume that the charging performance of liquid-solid triboelectric nanogenerator (TENG) could be improved by increasing the coverage of convex regions on the insulating surface. Following this concept, *M-glass-1* (Fig. 4.10a) was modified to increase the coverage of the convex area on the surface, which then became *M-glass-2* (Fig. 4.10b). EFM tests were carried out to analyze the surface charge of both surfaces after water-solid CE. To fabricate a TENG, copper tape was used as an electrode to stick to the bottom of the target insulator, and the ground terminal (GND) was applied as another working electrode. Finally, this designed TENG was used for short-circuiting current measurement to check the influence of curvature on CE.

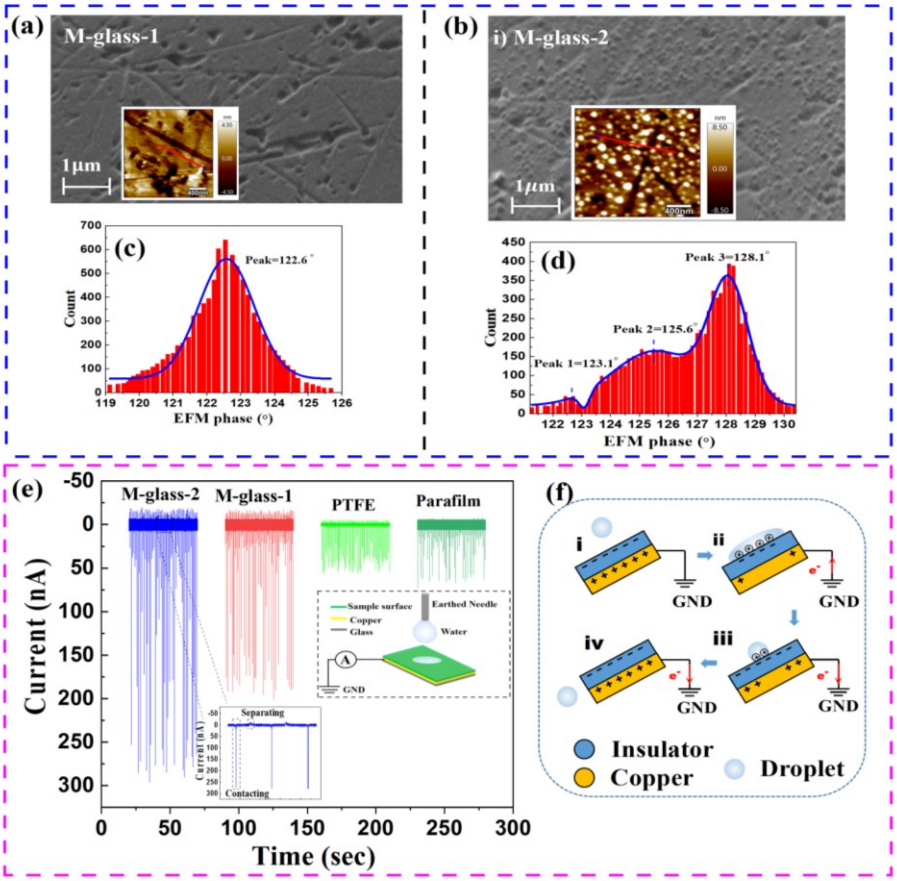

Figure 4.10: (a – b) Surface morphology and (c – d) EFM phase of *M-glass-1* and *M-glass-2* after liquid-solid CE, respectively; (e) TENG short-circuit current of different insulating surfaces; and (f) Working mechanism of the TENG driven by the contact electrification between water and insulating surface: (i) Falling of the 500th water drop, (ii) Drop spreading, (iii) Drop rebounding, and (iv) Drop leaving.

Compared to the SEM image of *M-glass-1* surface (Fig. 4.10a), *M-glass-2* (Fig. 4.10b) with silica nanoparticle coatings exhibited a higher convex coverage area. For both insulating surfaces, the chemical properties are identical. However, their curvature profiles were significantly distinct from each other, although it is worth noting that the heights of the roughness of the surfaces were nearly the same (~ 4 nm). Figs. 4.10c & 4.10d show the histogram of EFM phase distribution for *M-glass-1* and *M-glass-2* after CE with water drops, respectively. The EFM phase of *M-glass-1* had only one peak value centered at about 122.5°, whereas that of *M-glass-2* split into three peaks and every peak shows a higher phase value (φ_1= 122.7°, φ_2 = 125.6°, φ_3 = 128.1°). This means more charges could be transferred from water drops onto *M-glass-2* surface after CE, which led to the peak value of EFM phase positive shift. Such a conclusion is consistent with our hypothesis that surface with a higher convex coverage would have denser surface charge after CE.

Short-circuit current measurements were carried out on these surfaces through the specific designed TENG device. Their short-circuit currents are shown in Fig. 4.10e. It was found that TENG device fabricated by *M-glass-1* generated a short-circuit current of 180 nA, while the device made from *M-glass-2* exhibited a current of 280 nA. This finding is consistent with our theory that the short-circuit current increased when the surface contained a higher convex coverage. Working mechanism of the TENG driven by the contact electrification between water and insulating surface is illustrated in Fig. 4.10f. After CE by 500 consecutive water drops, the surface of the insulating layer reached a state of negative charged saturation (Fig. 4.10f(i)). Once the next liquid drop spreads on the surface, an appropriate amount of positive charge would be induced on the water drop surface to keep the solid-liquid contact interface electrically neutral (Fig. 4.10f(ii)). Meanwhile, the charge of the whole TENG system (water-insulating surface-copper electrode) is not neutral at that moment, due to the existence of the induced positive charges on the spread water surface. Therefore, more free electrons are required to compensate the copper electrode from the ground (GND, usually regarded as a negative electrode) to make the whole TENG system electrically neutral again. This process generates a positive current signal between the copper electrode and GND terminal (Fig. 4.10f(ii)). Since the convex surface can get more electrons from water drops, the saturated charge density on the surface of *M-glass-2* should be greater than *M-glass-1*. Therefore, when one water drop is spreading on the charge saturated surface of the *M-glass-2*, the induced charge intensity on water surface is much higher, thereby generating a stronger positive current output through the TENG device.

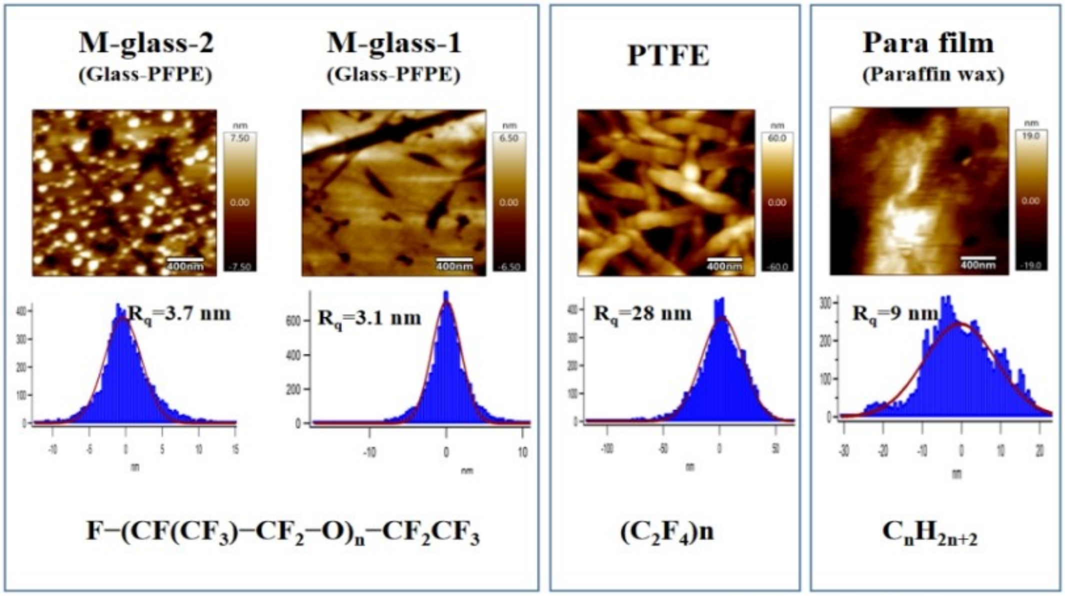

Rq: Standard deviation

Figure 4.11: Surface roughness of sample surfaces.

In addition, compared with the other insulating materials (PTFE and Parafilm), both M-glass surfaces had a stronger liquid-solid CE performance in TENG tests. This may be related to the nature (e.g., electronegativity) of the material surface [14, 101] and the modifications on surface roughness [122, 130] (Fig. 4.11). In conclusion, it can be inferred that the power generation performance of the solid-liquid TENG could be significantly improved by increasing the convex coverage on the surface due to the increase of surface capacity for negative charges. On the other hand, it is necessary to further explore the curvature effect of special nano-patterns with different shapes on CE, such as cones and spheres, which is still under investigation by our group.

4.5 Summary

In this chapter, we revealed the influence of the curvature effect on contact electrification in the liquid-solid made TENG at the nanoscale level. EFM results showed that convex surface (negative curvature) is more conducive to the electron transfer with liquid drops than that of the concave surface (positive curvature). A statistical trend was found that a smaller curvature would typically lead to a higher charging rate of negative charges after CE. After contact separating, the charge transfer from the surface to the atmosphere followed an exponential decay at a fixed temperature. Differently from the curvature effect on triboelectric charge generation, the charges on the concave surface were more likely to be emitted into the atmosphere than those on the convex surface. Based on these experimental results, we propose a curvature-dependent charge transfer model for distinct materials CE by introducing the curvature-induced energy shifts of the surface states. The short-circuit current output performance of TENG was found to be greatly improved by introducing more nano-layer structure on the insulating surface, which increases the convex coverage of the surface. TENG using the surface with more negative curvatures showed the best performance, suggesting that convex surface led to more electrons negatively charging the surface. These results strongly supported our theory about the curvature effect in nanoscale sizes. Our study has not only provided a new sight for understanding the CE, but also found an effective way to enhance the output performance of drop based TENG.

Chapter 5

Liquid-solid triboelectric nanogenerator for a wide operation window based on slippery lubricant-infused surfaces (SLIPS)

Modern civilization has entered the new era of "Internet of Things (IoT)", where numerous devices connect and exchange data with each other to work more efficiently and powerfully. With the increasing number of smart devices, it is urgent to develop new technologies and methods to harvest energy cost-effectively and at different scales, such that the power supply for IoT is ensured in all-weather conditions.

Water energy-harvesting techniques that rely on the generation and transfer of interfacial charges have drawn significant attention in the past decade, for example, by using triboelectric nanogenerators (TENG).[37, 39, 44, 131-136] Wang *et al.* reported on the development of nanogenerators and inspired scientists efforts in collecting sustainable blue energy.[133] TENG designs include those that rely on the triboelectric effect and/or electrostatic induction,[137-140] which takes place either at solid/solid or solid/liquid interfaces. Currently, for solid-water TENGs, the solid phase has been typically a hydrophobic or superhydrophobic surface (SHS), so that water droplets can be repelled rapidly to refresh the contact points, leading to continuous power generation.[74, 76, 141]

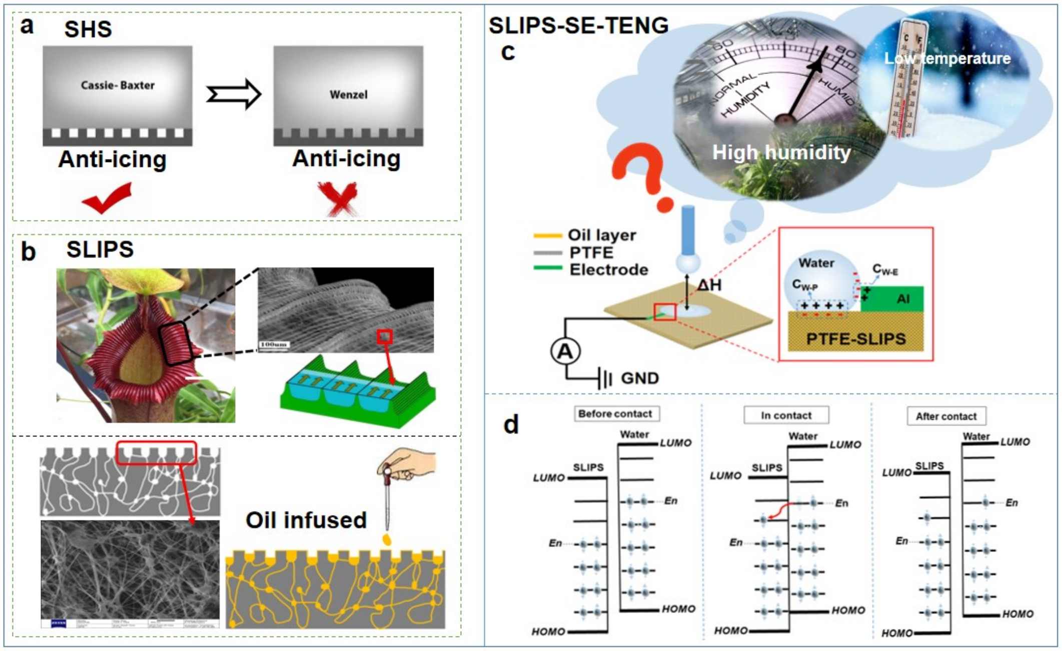

Figure 5.1: (a) Wetting transition from the Cassie-Baxter to the Wenzel states on superhydrophobic surfaces (SHS). (b) Nepenthes pitcher plant leaves trap a thin layer of water in its peristome, creating a slippery liquid layer. SLIPS imitates this latter mechanism by trapping a lubricant layer on hydrophobic surfaces, such as that of polytetrafluoroethylene (PTFE), making the surface slippery to droplets, and affording desirable properties. (c) A conceptual drawing of SLIPS-based TENG's adaptability in harsh environments. A SLIPS-SE-TENG is assembled by placing an electrode on the top surface of SLIPS. As an open circuit (in the disconnected state), only capacitance $C_{W\text{-}P}$ is relevant. When the droplet contacts the electrode, $C_{W\text{-}E}$ (existing between the water/electrode interfaces) is added to the connected circuit. R_W and R_L are the impedance of the water droplet and the load, respectively and GND means "ground". (d) Mechanism of contact electrification between liquid and SLIPS. (LUMO, a lowest unoccupied molecular orbital; E_n, the neutral level of surface states of SLIPS or liquid drop; HOMO, highest occupied molecular orbital)

However, common SHS are fabricated through the lotus effect and are limited by their long-term stability, for instance upon being impacted continuously by water or being scratched during usage, as shown in Fig. 5.1a. This is mostly attributed to the gradual degradation of microstructures.[142, 143] In addition, challenges arise for these SHS to be applied in varied environments, including high humidity and freezing temperatures. In both cases, the nucleation of nano-scale water droplets or ice/frost greatly inhibits the fluidity of the impacting droplets, which ultimately lead to the freezing of the entire surface and prevents the generation and transmission of effective charges.[144, 145] Therefore, in an effort to implement TENG power-supplied IOT devices in a wider range of scenarios, they need to be integrated with novel SHS for long-term stable hydrophobicity and robustness in harsh environments.

Inspired by the Nepenthes pitcher plant, slippery liquid infused porous surface (SLIPS) was first introduced in 2011[146] and quickly drawn attention as a novel SHS. For clarity, all lubricant infused surfaces are referred to as SLIPS in the following discussion. SLIPS could be fabricated by trapping a layer of lubricant oil at the surface of a porous medium, which leads to superhydrophobicity and low water droplet friction (Fig. 5.1b). It is worth noting that the thickness and distribution of oil layer on SLIPS need to be determined by the type and volume of oil injected, this will be discussed in detail later. SLIPS allows for the creation of unique properties, such as anti-fouling[147], anti-icing[148], and drag reduction[149]. Although both SLIPS and TENG have been reported as separate topics, only two experimental studies have considered their combination at the time of writing.[150, 151] For instance Xu *et al.*[151] demonstrated the feasibility of SLIPS-TENG and reported relatively low instantaneous power output (~0.2 μW). This relatively low performance can be explained by the challenges that exist in synergizing the advantages of SLIPS and TENG. Recently, a new transistor-inspired single electrode triboelectric nanogenerator (SE-TENG) was designed with ultra-high efficiency for harvesting water energy.[152] SE-TENG highlights the energy harvest directly from a bulk effect, which is substantially more efficient than the conventional interfacial effect of traditional designs. Therefore, as shown in this effort, the combination of SLIPS and SE-TENG can greatly improve the power output (Fig. 5.1c).

It is generally accepted that SLIPS involves a layer of spreading lubricant oil.[153, 154] The failure of SLIPS in the present context is likely caused by the limited thickness of the oil layer on the substrate. Hence, a standing question is related to the critical thickness that will make SLIPS efficient in the operation. There are many unresolved questions as far as ow the properties of the lubricant (*e.g.*, lubricant type, lubricant layer thickness) influence the output performance of SLIPS-SE-TENG. Hence, it is necessary to understand the role of the lubricant on both SLIPS properties and SLIPS-SE-TENG performance, i.e., to provide theoretical support to the fabrication and optimization of SLIPS-SE-TENG.

In this chapter, we integrated the slippery lubricant infused porous surface with a transistor-inspired architecture to develop a robust triboelectric nanogenerator (SLIPS-SE-TENG). Our results indicated that the use of PFPE (4 $\mu L/cm^2$) as lubricant enables a stable high-power output in SLIPS-SE-TENG. A maximum output power of about 5 μW was measured, representing a 25-fold improvement over the recently reported value.[151] Importantly, experimental results confirmed that PFPE-infused SLIPS showed the best output performance using an oil layer thickness as low as 20 nm. This SLIPS-SE-TENG showed strong environmental adaptability and output stability under harsh conditions, e.g., at high

(T~ 55°C)/low temperature (T~ -5°C), or with high relative humidity (RH~ 90%). In general, our findings provide new insights into the construction of SLIPS and make SLIPS-SE-TENG feasible for operation under all-weather working conditions.

5.1 Performance of SLIPS-SE-TENG

The PFPE was dripped on the PTFE surface, where the oil spontaneously spread and infused into the porous membrane matrix *via* capillary wicking, owing to the preferential affinity between the lubricant oil and PTFE membrane.[103] The robustness of the as-fabricated lubricant-infused surface was assessed by the criterion that water drops could easily slide on the surface with a low contact angle hysteresis (CAH).[155] It can be confirmed that the PFPE-infused surface in this study fulfilled the criteria for SLIPS, with an ultralow CAH, ~5 ° (Contact angle= 121.3°, Fig. 5.2).

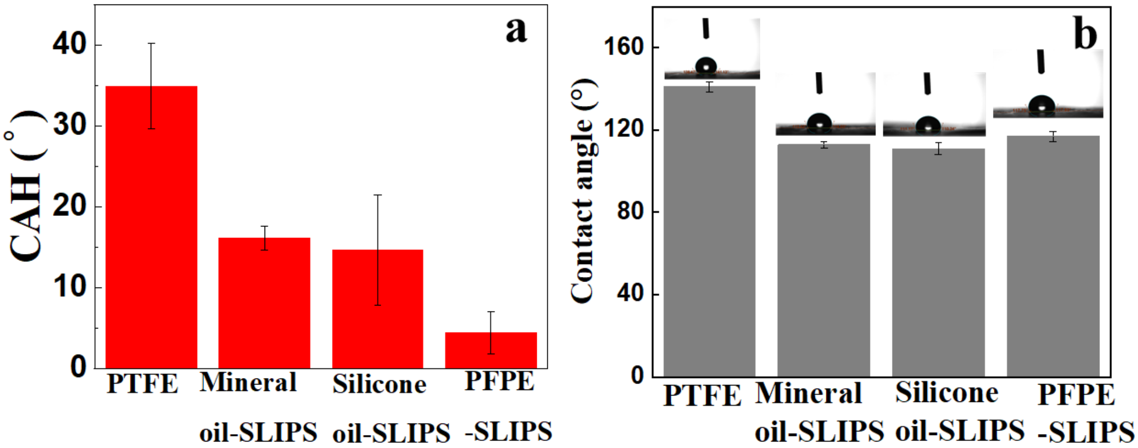

Figure 5.2: Contact angle hysteresis (CAH) and contact angle (CA) of virgin PTFE and 4 μL/cm^2 lubricants infused SLIPS.

Contact electrification (CE) surface, SLIPS, was integrated with the transistor-inspired architecture SE-TENG, as shown in Fig. 5.1c. When the liquid drops in contact with the solid surface (Fig. 5.1d), differences in surface energy level (E_n) would cause electrons to transfer from the high energy (e.g., water drop) to the low energy level surface (e.g., SLIPS). After contact, electrons generated from CE can be maintained on the SLIPS when the energy barrier has a higher magnitude than energy fluctuation. Therefore, the surface of SLIPS should be negatively charged after rubbing against water droplets. More detailed discussion about the working principle of such SLIPS-SE-TENG is provided in Fig. 5.3.

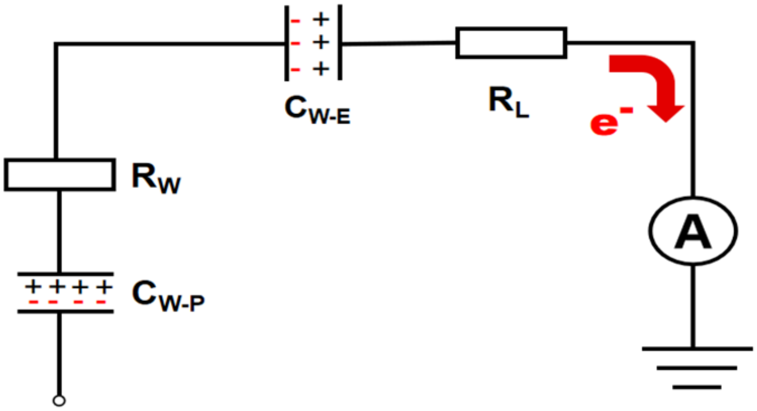

Figure 5.3: The equivalent circuit model of the TENG

As an open circuit (in the disconnected state), only the capacitance C_{W-P} is relevant. A droplet contacting the electrode, C_{W-E} (existing between the water/electrode interfaces) is added to the connected circuit. R_W and R_L are the impedance of the water droplet and the load, respectively and GND means "ground". When the impinging droplet contacts the electrode, the droplet bridges the originally disconnected components such as the solid surface and the single electrode into connection. A large number of negative or positive charges accumulate around the single electrode following an electrical signal output between the electrode and the ground. The direction of electron transfer depends on the charge polarity of the surface.

The as-fabricated SLIPS-SE-TENG could generate a short-circuit current of ~3.0 μA (Fig. 5.4a) when using a PFPE-infused (4 μL/cm^2) SLIPS. The current output is sufficient to drive small electronic devices. The performance of the SLIPS integrated SE-TENG was greatly affected by the properties of the SLIPS, especially by the volume of infused lubricant. Increasing the lubricant volume to 20 μL/cm^2 caused a sharp decrease in the short-circuit currents down to about 0.5 μA (Fig. 5.4b), whereas the prototype SE-TENG using PTFE surface, with no lubricant coating, exhibited a maximum output current ~4 μA (Fig. 5.5). In general, the presence of lubricant oil endows SLIPS properties on the PTFE surface but weakens the output current. This is most likely because the water-SLIPS CE is a combination of water-lubricant and water-PTFE CEs, where the triboelectric charges generated from liquid-liquid CE are weaker than a water drop impacting on a solid[156]. Nevertheless, the SLIPS possesses various advantages over typical superhydrophobic surfaces based on the lotus effect, thus making the SLIPS-SE-TENG attractive in many applications which will be discussed in the following sections.

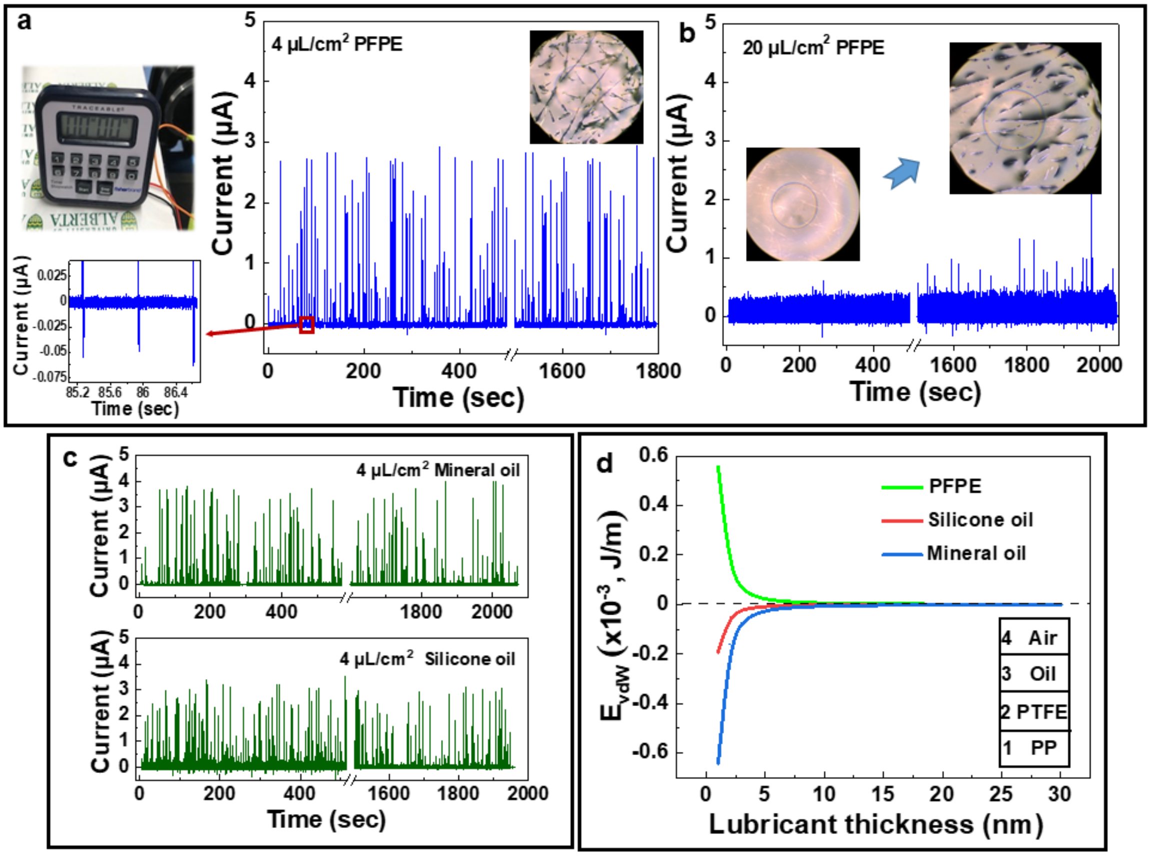

Figure 5.4: Influence of PFPE lubricant infusion (a) 4 μL/cm^2 (the inset is a partial enlargement of the SLIPS surface after the droplet sliding, pictures on the side correspond to a small electronic driving by SLIPS-SE-TENG and an enlarged view of the negative current value, respectively) and (b) 20 μL/cm^2 on the SLIPS-SE-TENG output performance. Insets show the partial enlargement of the SLIPS surface before (completely covered) and after (partially covered) the droplet sliding. (c) Effect of lubricant type (silicone oil, mineral oil) on the performance of the SLIPS-SE-TENG (infusion volume kept at 4 μL/cm^2). (d) Calculated van der Waals interaction as a function of the lubricant's oil thickness for PTFE. Insert image shows a simplified illustration of SLIPS structures. (PP: polypropylene)

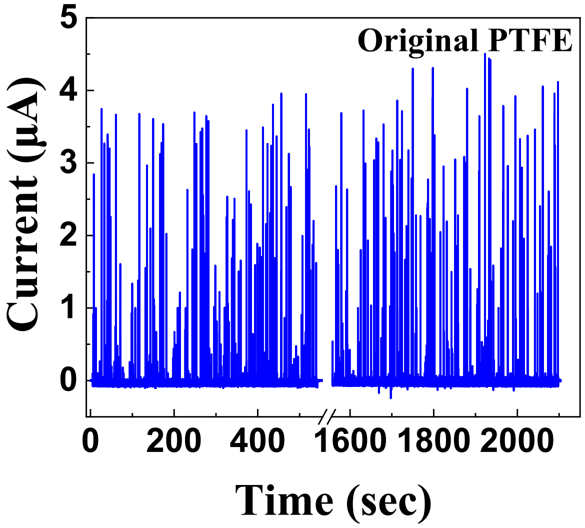

Figure 5.5: SE-TENG output performance fabricated by virgin PTFE (H= 4cm, tilt angle= 35°, Temperature= 23℃，Humidity= 40%)

Interestingly, the over-coated lubricant layer could be peeled off gradually with water drop impact and sliding. The inhibition of lubricant oil on TENG performance was most severe in the early stage ($t < 600$ s), but there appeared to be some restoration of the short-circuit current after a consecutive dipping for more than 1600 s (Fig. 5.4b). It is most likely that the continuous movement of water drops washed away the excess oil from the SLIPS, as evidenced by the inset picture in Fig. 5.4b. It is worth noting that the thin oil layer near the surface could be trapped by van der Waals and capillary effects, whereas the bulk of lubricant is only held by cohesion interactions when the oil layer is thick (> 20 nm). The thick-layer lubricant oil was easy to wash out when the droplet slid on the surface. This result was further verified by the difference in weight of the SLIPS before and after the SE-TENG tests, as shown in Fig. 5.6. Lubricant depletion was observed in either case by monitoring the mass change of the SLIPS before and after the triboelectric nanogeneration. This unavoidable consumption is due to the spontaneous oil spreading on the water droplet when the latter is in contact with the SLIPS. Therefore, the spread oil will be carried away as the water droplet leaves the system. However, it has been reported that this dissipation process (for thin layers) is much slower compared to the consumption of excess oil on the surface, for thick lubricant layers.

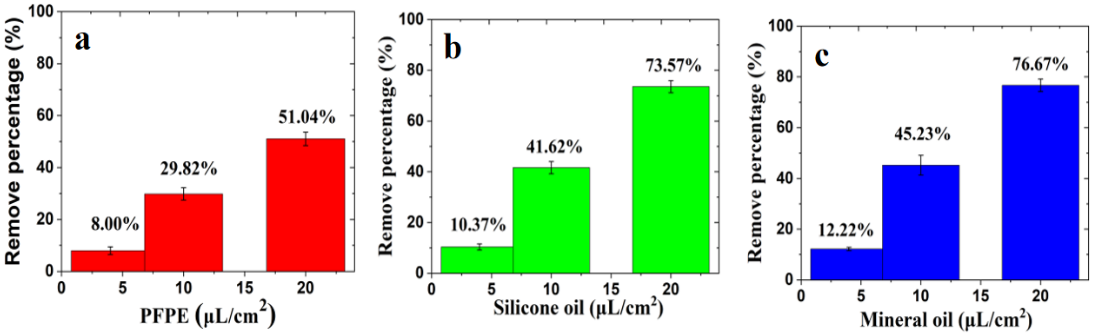

Figure 5.6: Weight difference of various SLIPS (PFPE, Silicone oil and Mineral oil) before and after the TENG tests (4000 μL/min drop continues falling from a pumping syringe for 60 min)

It should be pointed out that many features might influence the performance of SLIPS-SE-TENG fabricated with given oil layer thickness or oil types. For instance, the transition from liquid-liquid CE [127, 157] to liquid-solid CE[1] may affect SLIPS-SE-TENG performance. As shown in Fig. 5.4c, the short-circuit current of mineral oil- (or silicone oil-) infused SLIPS-SE-TENG was higher than that of the PFPE-infused surface. However, the two surfaces were considered as robust SLIPS due to their relatively higher CAH (Fig. 5.2a). Peppou-Chapman *et al.* [154]pointed out that for silicone oil-infused SLIPS, PTFE showed a discontinuous layer thickness with the lubricant meeting the surface at a finite contact angle (60 ± 2°). Therefore, it is assumed that the coverage characteristics of the lubricant have a distinct effect on the performance of the SE-TENG. In an effort to prove our hypothesis, we calculated the van der Waals interaction as a function of oil layer thickness for PTFE according to Eq. (5-1) as below, and the results are given in Fig. 5.4d.

This system is a four-layer system where the bottom layer (1) is the shrinkable Polypropylene substrate (PP), the second layer (2) is the rigid polymer layer (PFPE), the third layer (3) is lubricant oil, and the last layer (4) is air; see Fig. 5.4d for a schematic of this stack. The overall expression for this is:

$$\mathrm{E_{vdw}(d)} = -\frac{\mathrm{A_{234}}}{12\pi \mathrm{d}^2} + \frac{(\mathrm{A_{234}} - \mathrm{A_{132}})}{12\pi(\mathrm{d}+\mathrm{h})^2} \tag{5-1}$$

where $\mathrm{A_{xyz}}$ is the Hamaker constant for the three-layer system, d is the thickness of the lubricant oil layer and h is the thickness of the PTFE coating. The three-layer Hamaker constant can be calculated using the following expression:

$$A_{132} = \frac{3}{4} k_B T \left(\frac{\varepsilon_1 - \varepsilon_3}{\varepsilon_1 + \varepsilon_3}\right)\left(\frac{\varepsilon_2 - \varepsilon_3}{\varepsilon_2 + \varepsilon_3}\right) + \frac{3 h v_e}{8\sqrt{2}} \times \frac{({n_1}^2 - {n_3}^2)({n_2}^2 - {n_3}^2)}{\sqrt{({n_1}^2 + {n_3}^2)({n_2}^2 + {n_3}^2)}\left[\sqrt{({n_1}^2 + {n_3}^2)} + \sqrt{({n_2}^2 + {n_3}^2)}\right]} \tag{5-2}$$

where ε_i and n_i are the dielectric constant and the refractive index of material *i*, respectively, k_B is the Boltzmann's constant, *T* is the absolute temperature, *h* is Planck's constant, and v_e is the plasma frequency of free-electron gas. The following values were used to calculate the interface potential for PTFE:

	n	**ε**
Air	1	1
PFPE	1.24	2.9
Mineral oil	1.47	2.23
Silicon oil	1.41	2.3
PTFE	1.31	1.93
Polypropylene	1.49	2.1

A positive potential was calculated for all film thicknesses when PTFE matrix was infused by PFPE. This result indicates that there is a repulsion between PTFE and air; it also demonstrates that it is favorable in terms of energy production to have a stable PFPE layer spread between the PTFE and the air. Conversely, mineral oil (or silicone oil) would result in negative potentials, indicating that there is an attraction between PTFE and air. This means the resulting film was not stable for all film thicknesses, and bare PTFE surfaces have the advantage of being exposed to air. As mentioned, the exposed area of PTFE leads to more liquid-solid CE, which is the main reason explaining that the performance of mineral oil-infused SLIPS-SE-TENG was better than that of the PFPE-infused surface with the same oil infusion volume (4 $\mu L/cm^2$). However, such surfaces with partial solid exposure are improper to be classified as robust SLIPS since they cannot provide slippery conditions over the entire surface. When water droplets slide across these solid surfaces, it is possible that the three-phase contact line pins at the lubricant-free areas, thereby causing an apparent increase in lateral friction.

In general, it can be concluded that the performance of SLIPS-SE-TENG was highly related to the SLIPS, including both the volume and type of the infusion lubricant. These factors affected the distribution of lubricant oil on the solid substrate, which then influenced the water-SLIPS CE upon contact and sliding. In the next section, we further strengthen this conclusion by describing the lateral force of water droplets sliding on different SLIPS surfaces and by discussing the lubricant distribution on PTFE substrates.

5.2 Characteristics of SLIPS

The lateral forces of water drop sliding on SLIPS were measured using an AFM water drop probe through "Friction Loop" module. As for AFM water drop probe fabrication, Custom-made rectangular silicon cantilever (400 × 70 × 2 μm) with a circular gold patch at one end (diameter 65 μm, thickness 30 nm) was used for force measurement. The gold patch was modified to be hydrophilic by immersing the cantilever in 10mM 11-mercapto-1-undecanol in ethanol solution for 2 h for safe anchoring of water drop[158]. For each experiment, water drop was first injected into an AFM fluid cell filled with toluene using an ultra-sharp glass pipette, and then a drop was picked up by the cantilever to create a drop probe. The spring constant of the cantilever was determined to be 0.3-0.4 N/m using the Hutter and Bechhoefer thermal tune method before loading of drop. The drop was then lifted from fluid cell. Remove the cell and replace it with SLIPS. Lowing the drop-loaded cantilever until drop attachment occurred as soon as possible. After the water droplets come into contact with SLIPS, the water droplet surface will be cloaked by a very thin layer of lubricant oil immediately [159], thereby sharply slowing down the evaporation rate of the water droplets. It should be noted that slowing down the evaporation rate of water is the key to the successful implementation of lateral force determination. The lateral force measurement was conducted within 1 minute. For each experiment, force curves of at least 3 water drops were measured and similar results were obtained. Lateral force of SLIPS with water drop (Diameter~100 μm) in air was measured using an MFP-3D AFM (Asylum Research, Santa Barbara, CA) mounted on an inverted microscope (Nikon Ti-U). The method of performing LFM measurements in this research is through something called a "Friction Loop". This is a non-imaging technique where the "slow axis" of the scan is disabled, and the cantilever is simply rastered back and forth over the same line on the sample. The Friction Loop Panel will ramp the Y-axis of the AFM Scanner to move orthogonal to the long axis of the cantilever, while the tip is engaged in contact on the surface. It will record the Lateral signal as a function of the Y-sensor position during this.

The differences in droplet mobility were compared between PFPE-infused and mineral oil-infused SLIPS (Fig. 5.7a). For the 4 μL/cm^2 mineral oil-infused surface, the exposed solid surface provided enough sites to pin and drag the water droplet, as shown by the relatively high lateral force. As expected, the lateral force (F_L) of the mineral oil-infused surface was independent of the scanning speed (V_s), as high as 1.5 μN. On the other hand, PFPE oil had a preferential wetting on PTFE, and therefore the as-prepared SLIPS was fully covered by the lubricant if there was a sufficient volume of oil. Experimental results demonstrated that the droplet moved easily on PFPE-infused SLIPS. Especially, when the V_s was larger than 0.3 mm/s, the lateral force for a water droplet (diameter ~ 100 μm) to slide was indistinguishable for all PFPE-infused surfaces investigated. If the lubricant layer was too thin (4 μL/cm^2 PFPE infused surface), the droplet became more likely to be pinned by the PTFE substrate at a low V_s (< 0.3 mm/s), resulting in a maximum F_L ~1 μN. The lateral force plummeted from 1 μN to 0 μN when the droplet moving speed V_s surpassed a threshold, suggesting the occurrence of a state transition where the magnitude relates to the infused lubricant volume and solid structure.[159] Note that for a lubrication surface with 20 μL/cm^2 PFPE, there was no dragging of the droplet even at the lowest V_s of 0.05mm/s (scanning speed 1 Hz), and F_L basically equaled zero. Daniel *et al.*[160] attributed this behavior to a stable lubricant layer that prevented pinning and gave rise to a velocity-independent, viscous, dissipation force. The above experimental results show that the mobility of droplets on SLIPS was not only related to the type of lubricant oil, but also to its volume. Collectively, both factors affected the final performance of SLIPS-SE-TENG.

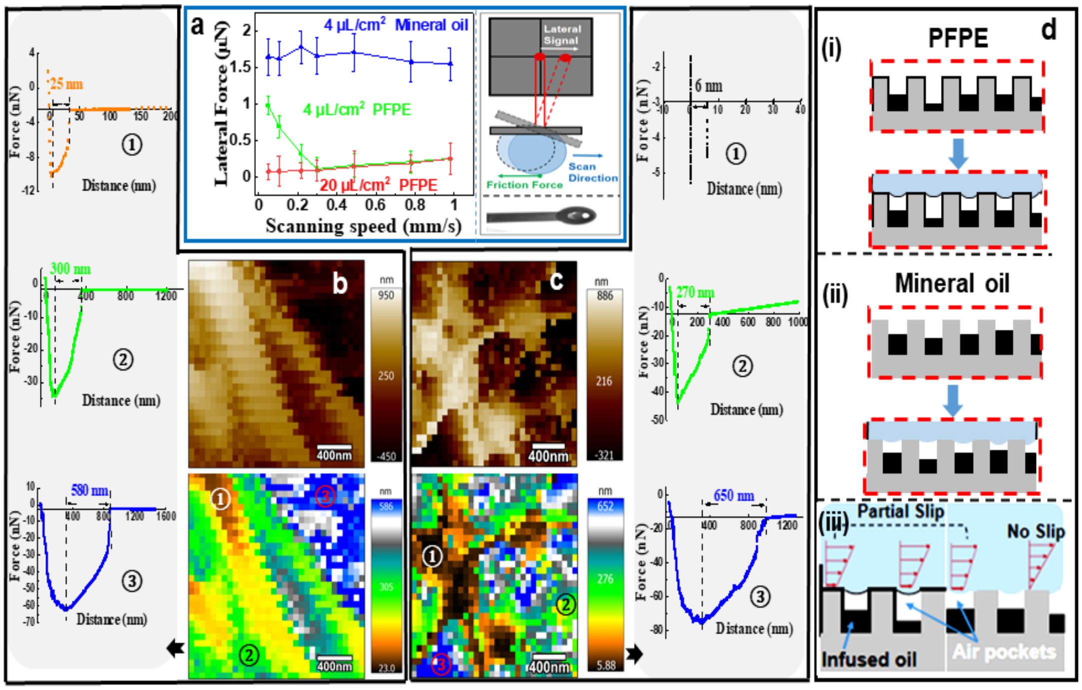

Figure 5.7: (a) Lateral forces acting on water droplets on flat, lubricated substrates (PFPE and Mineral oil). Schematic of the AFM water-probe to measure lateral forces. Topography (top), lubricant thickness (bottom) of (b) PFPE or (c) mineral oil-infused PTFE wrinkled surfaces. The force-displacement curve represented by the corresponding orange (①), cyan (②) and blue (③) points in the thickness distribution diagram is provided beside each point. The resulting distribution map is composed of squares, each with a color that represents a different value. (d) Thermodynamic configuration of lubricant in air and underwater, respectively. (i) PFPE (4μL/cm^2) configuration of SLIPS in air and underwater (ii) Mineral oil (4μL/cm^2) configuration of SLIPS in air and underwater (iii) Schematic of flow over two lubricant-infused porous surface containing air pockets, with definition of variables.

Meanwhile, from a more fundamental point of view, the type and volume of lubricant determined how oil was distributed on the substrates. Although the van der Waals interaction energy could roughly estimate the thermodynamic preference of liquid configurations, it was more straightforward to measure the thickness distribution of the oil layer on the SLIPS directly. This could be useful to achieve a better understanding of the SLIPS-SE-TENG performance. Hence, the thickness distribution of the infused lubricant layer was investigated using force mapping on two different SLIPS. First, a series of experiments was carried out to guarantee the accuracy of these thickness results which: (1) confirmed that the surface topography did not affect the measured lubricant thickness, (2) determined the influence of water vapour adsorption thickness (approximately 6.0 nm), and (3) confirmed that the oil layer on the SLIPS did not adhere to the probe and generally did not affect the measured lubricant thickness, as shown in Fig. 5.8. From Fig. 5.8a or 5.8b (i) and (ii), it can be seen that the solid surface morphology has no significant effect on the thickness measurement. In addition, after using the new or the used AFM probes to measure the thickness on the virgin PTFE surface in the air, it is obvious that the value at the maximum thickness is basically the same, which can eliminate the influence of oil sticking to the probe on the thickness measurement. In addition, it should be noted that the maximum thickness of both measurements is not equal to 0 (The thickness value is about 6~7 nm). This result is most likely to be the effect of air vapor adsorption, which needs to be considered in subsequent experiments.

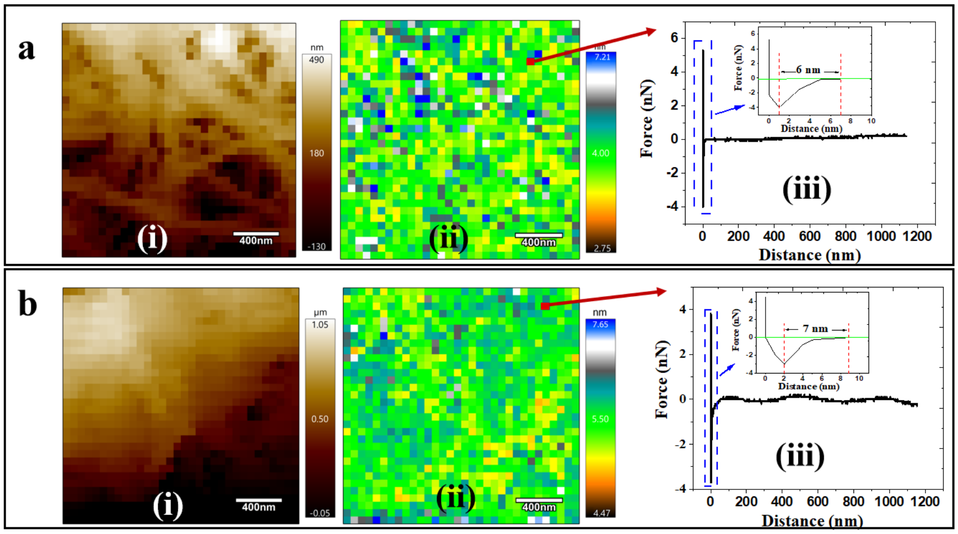

Figure 5.8: Effect of water vapour on thickness analysis of virgin PTFE by (a) a new and (b) a used AFM probe in the air. The first panel is topography (i), and the second is a reconstructed map of lubricant thickness (ii) and the point force curve on the thickness map (iii). (T=23°C，Humidity=40%)

The lubricant thickness analyses are presented in Figs. 5.7b and 5.7c, shown in two panels for each sample. The first panel corresponds to the topography (top), and the second is a reconstructed map of thickness of lubricant (bottom) according to the force curve. For both lubricant-infused SLIPS, the concave surface (such as the blue area) displayed a thicker oil layer owing to capillary forces, a result that was anticipated. Obvious differences in the oil layer thickness can be observed in some convex areas (*e.g.*, the orange area). The minimum oil layer thickness of PFPE-infused SLIPS was maintained at about 20 nm (after subtracting 6 nm caused by water vapour adsorption, Fig. 5.7.b-①), while mineral oil-infused SLIPS have part of its surface exposed to air (thickness equal to 0 nm, Fig. 5.7c-①). Unambiguous evidence was verified by scanning the oil layer thickness over a wider range (Fig. 5.9).

These results indicated that the infused PFPE lubricant layer stayed on the PTFE membrane surface in a much more stable way than mineral oil.

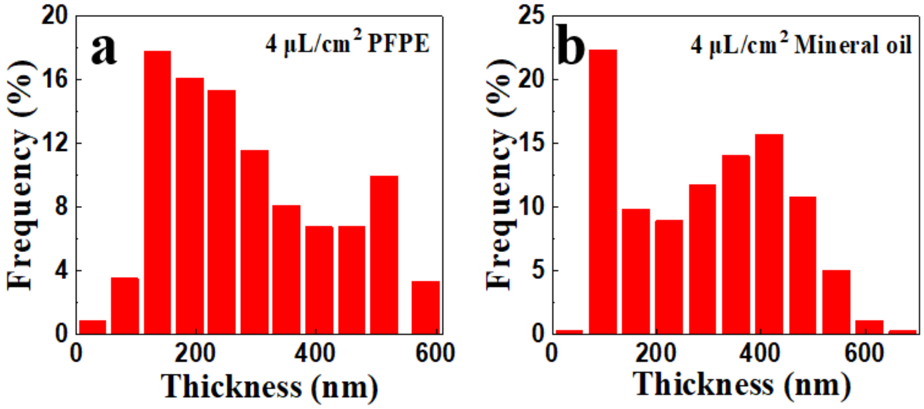

Figure 5.9: The lubricant thickness statistics histogram for ten distinct positions on (a) PFPE-infused and (b) Mineral oil- infused SLIPS.

One can now consider the possible configurations of lubricant oil on the SLIPS upon contact with water, which is critical during water sliding. When underneath the droplet, the interface attained one of three different states (impaled, impregnated, encapsulated), depending on which had the lowest energy.[104] Theoretical calculations about the most likely configuration in a specified system have been performed by Smith *et.al*.[153] In our research, when the droplet slid on the PFPE-infused SLIPS, there was always a continuous layer of lubricant oil with a certain thickness (van der Waals force and capillary force domain) between the droplet and the PTFE substrate, as shown in Fig. 5.7d(i). This continuous layer ensured a robust, slippery, sliding motion of water drops, which is essential to the continuous generation of triboelectric energy. On the other hand, PTFE surfaces were partially exposed to air when mineral oil was the infusion layer (Fig. 5.7d(ii)), which means that part of the PTFE surface was directly in contact with water drops.

Therefore, mineral oil-infused SLIPS might exhibit a discontinuous triboelectric generation problem. For example, the exposure of rough PTFE surfaces provided active sites for ice nucleation, and the surface thereby became gradually covered by ice under low temperatures, thereafter, making the TENG completely ineffective at the end.

On the other hand, it is possible that as water drops falling from a certain distance and impacting the solid surface, a high spreading velocity V_s resulted in this process. Under a high moving velocity V_s, it is expected that the F_L between the water drop and the 4 μL/cm^2 PFPE-infused surface was much lower than that of the 4 μL/cm^2 mineral oil infused surface. This is because the lubricant oil fully spread on the substrate, allowing no exposure of solid surfaces, while the air pockets trapped on the porous of surface greatly increased the slip length of the flowing fluid on the SLIPS[161], as illustrated in Fig. 5.7d(iii). The goal of integrating the SLIPS and the SE-TENG was to construct a new device endowing SLIPS advantages, such as self-healing, low friction resistance, *etc*. Therefore, combining the output performance and surface superiority of the SLIPS-SE-TENG, 4 μL/cm^2 PFPE-infused SLIPS was the best choice for SE-TENG fabrication.

5.3 Device optimization for SLIPS-SE-TENG

In the previous sections, we investigated the influence of SLIPS on SE-TENG performance and showed that a PFPE-infused SLIPS-SE-TENG harvested triboelectric energy efficiently, because it simultaneously possessed the SLIPS characteristics and maintained a stable electric output performance. After determining the most appropriate SLIP surface for SE-TENG fabrication, the next objective was to optimize the as-fabricated SLIPS-SE-

TENG by adjusting the device setups, e.g., the placements of the electrode and the falling height of the water droplets.

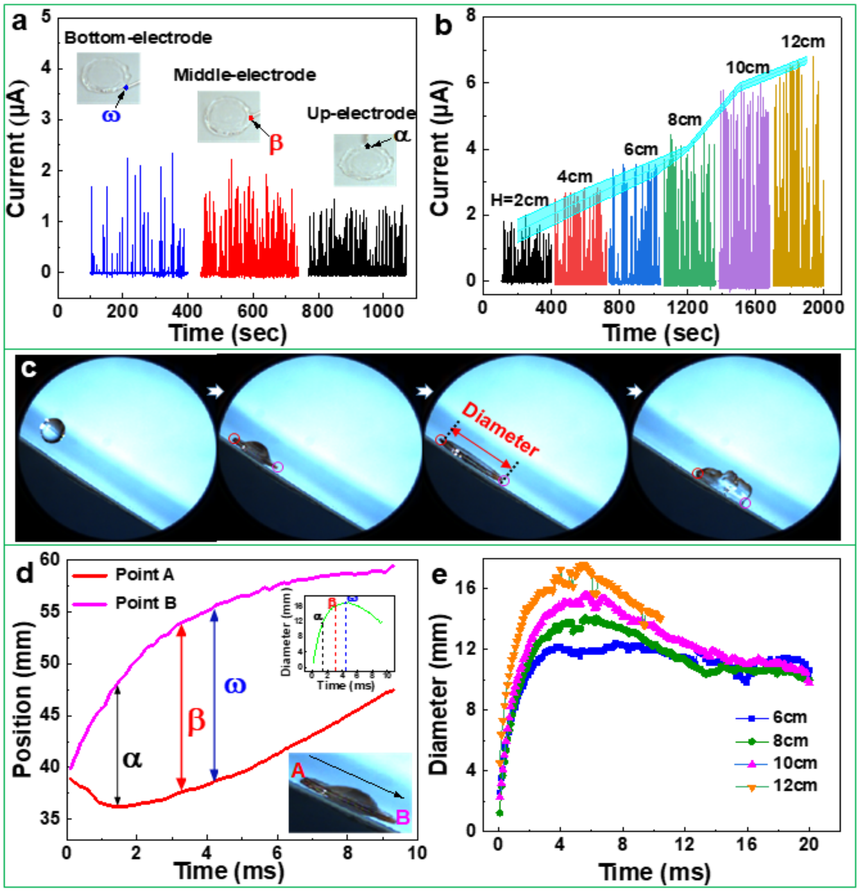

Figure 5.10: Influence of (a) placements of the electrode and (b) falling height of water droplets on the performance of the SLIPS-SE-TENG (default at the middle-electrode position, the shaded part represents the error bar). (c) Tracking and (d) analyzing of the water droplets sliding process on the surface. Inset shows the dynamic diameter of the droplet on the surface during the spreading-rebounding process. Point A and B represent the upper and lower pole positions of the droplet in the moving process respectively. (e) Dynamic diameter of a droplet spreading-rebounding on the SLIPS under different drop heights (4 μL/cm^2 PFPE-infused PTFE surface).

The effect of electrode placement on the output performance of SLIPS-SE-TENG was initially investigated, and the results are displayed in Fig. 5.10a. Water droplets were released from a height (*H)* of 4 cm in this set of experiments. Position 'α' was the upper boundary where the water drop could reach by spreading, whereas position 'ω' was the spot where the water drop had the largest contact area (*i.e.,* spreading area) with the SLIPS surface. Experimental results indicate that the maximum outputs of the SLIPS-SE-TENG at electrode placement 'β' and 'ω' were relatively higher than when the electrode was placed at position 'α'. Among the three different electrode positions, position 'ω' provided the highest current of maximum output, but also showed severe stability problems on triboelectric generation, as indicated by the inconsistent current peaks throughout. This issue was not found in the neat PTFE-SE-TENG test results (Fig. 5.11), so it was most likely due to the SLIPS layer.

To understand the basic principles underlying the effect of the electrode placement and drop height on the SE-TENG output, water droplets were tracked and analyzed during the sliding process on SLIPS by a high-speed camera (Fig. 5.10c) and a custom-made MATLAB code (Appendix B). The position changes of point '*A*' and point '*B*' over time during the droplet spreading-rebounding process on the SLIPS were analyzed by MATLAB, as shown in Fig. 5.10d, where the inset picture is the dynamic diameter of the water drop during the spreading-rebounding process on the SLIPS surface (obtained by the distance between points *A* and *B*). If the electrode was fixed at position 'α', the maximum spreading diameter of the water droplet was much lower than the diameter detected at positions 'β' and 'ω', when water and the electrode were connected. This is the main reason for the lowest TENG output observed when the electrode was placed at position 'α'. In addition, water droplets spreading on the soft SLIPS would cause random viscous energy dissipation.[162] Therefore, it was almost impossible to guarantee that each water droplet could spread up to the original maximum diameter, where it can connect to the electrode fixed at point "ω" and provide a maximum current output. If the water droplet and the electrode did not touch, the SE-TENG would not be able to work during this period, which explains the low peak frequency of the short-circuit current when the electrode is fixed at position 'ω'. Consequently, the optimum electrode position is at point 'β', which offered the best compromise between spreading area and stability.

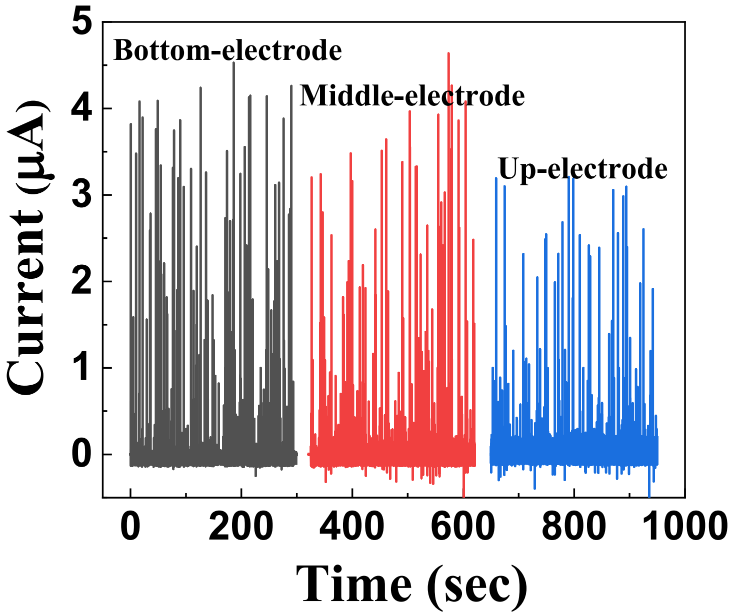

Figure 5.11: Influence of electrodeposition on the performance of virgin hydrophobic PTFE-TENG. (Falling height 4 cm, Tilt angle 35°, Temperature 23 ºC, Humidity 40%)

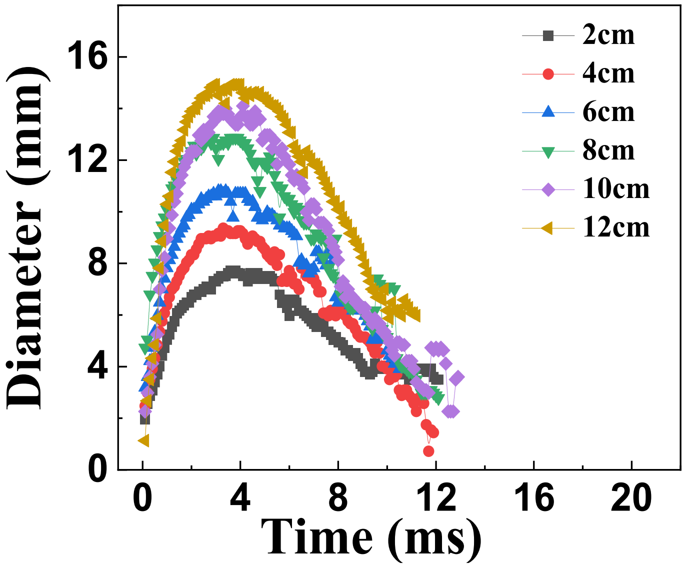

Figure 5.12: The dynamic diameter of a droplet spreading-rebounding on the virgin PTFE surface under different drop height. (Tilt angle 35°, Temperature 23 ºC, Humidity 40%)

On the other hand, the falling height of the water drop also showed a significant impact on the performance of the SLIPS-SE-TENG. As illustrated in Fig. 5.10b, the output of the SLIPS-SE-TENG gradually improved as the falling height was increased. For example, when the height was 12 cm, the maximum output of the SE-TENG (~6.2 μA) was about three times higher than it was when the height was 2 cm (~2 μA). It is worth noting that the distance from the end of the needle to the point where the droplet hits the interface was taken as the default falling height. However, it is difficult to accurately distinguish the hitting position of the droplet with the naked eye. Only a rough impact position can be estimated, which leads to a certain error between the actual droplet falling height and the experimental setting value. Obviously, the error of the height measurement caused uncertainty (Fig. 5.10b) in the measured value of the short-circuit current. Lift the falling height would increase the maximum contact area between the droplets and the SLIPS, thereby improving the output performance of the SLIPS-SE-TENG. As shown in Fig.

5.10e, the short-circuit current value of the SLIPS-SE-TENG gradually improved as the effective contact area increased. Due to the low CAH of the SLIPS, the maximum spreading diameter of the water droplets on the SLIPS (D ~ 17 mm) was higher than that of neat PTFE (e.g., D ~ 15 mm at drop height = 12 cm, Fig. 5.12), which was beneficial to the improved performance of the SLIPS-SE-TENG.

5.4 SLIPS-SE-TENG in harsh environments

The SLIPS are notorious for their superiority as far as surface characteristics, including self-healing, self-cleaning, high light transmission[163, 164], and strong resistance to harsh environments[165] (such as extremely low temperatures and high humidity). Therefore, it is therein proposed that the SLIPS-SE-TENG devices should also incorporate these SLIPS advantages and be capable of working normally and stably in harsh environments.

The SLIPS-SE-TENG exhibited a robust triboelectric generation performance in low temperature environments, such as during winter months or in arctic areas. Figs. 5.13a-5.13c displayed the short-circuit current of the SE-TENG fabricated by various surfaces at room temperature (~23°C) and low temperature (-5°C). In these experiments, ambient humidity (40%) was maintained. At room temperature, the electric output of the SLIPS-SE-TENG remained stable for more than half an hour. Interestingly, in a low-temperature environment, there appeared to be robust short-circuit current outputs at about 3 μA (the maximum output power and charge density are about 5.0 μW and 8.8 nC/cm^2, respectively, for a maximum contact area of 0.79 cm^2 Fig. 5.14 and Fig. 5.15) for the PFPE-infused SLIPS-SE-TENG. As a direct comparison, the current output quickly decayed to nearly negligible (~0.2 μA) for both neat PTFE and mineral oil-infused SLIPS integrated SE-TENG after being placed in a frozen environment.

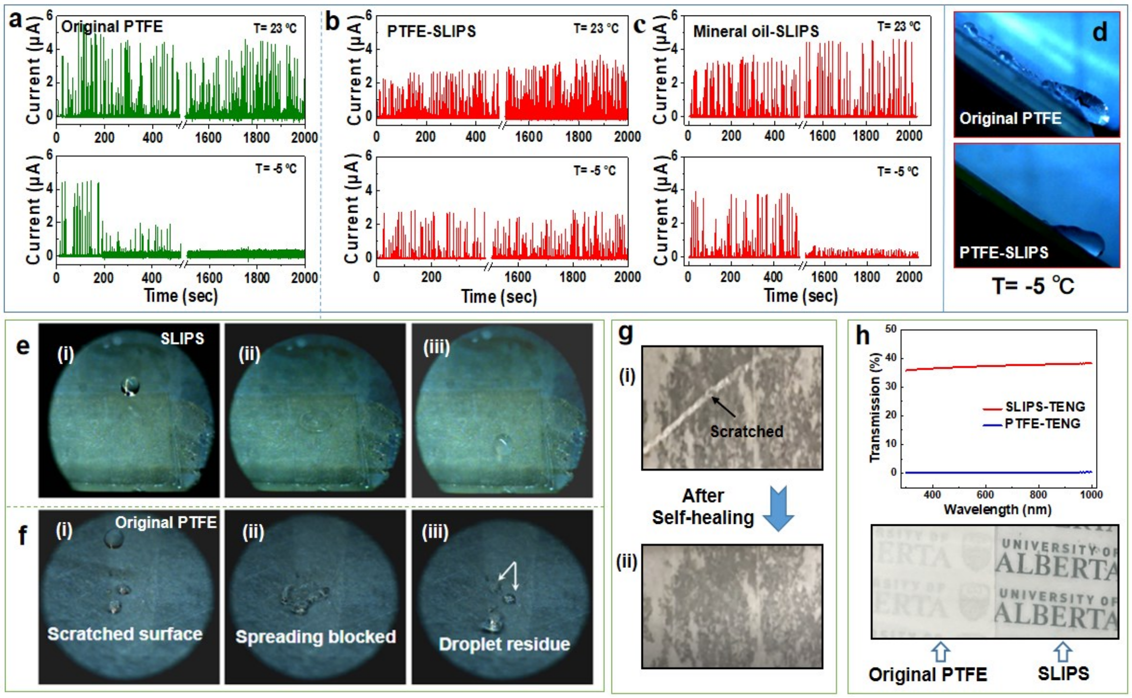

Figure 5.13: Influence of environmental temperature (23 °C and -5 °C) on the performance of the SE-TENG integrated with (a) original PTFE surface, (b) PFPE-infused SLIPS, and (c) Mineral oil-infused SLIPS (4 μL/cm^2 lubricant infusion). (d) Comparison of water droplet movement on the neat PTFE surface and PFPE-infused SLIPS under low temperature. Water droplet movement on the damaged (e) SLIPS and (f) original PTFE surface. (g) PTFE matrix is first damaged with scratches (top) but within 1 s, the smooth interface and optical property of the SLIPS-SE-TENG was restored (bottom). (h) Comparison of optical transmittance between the SLIPS and the neat PTFE.

As shown in Fig. 5.13d, for the original PTFE surface (T = -5°C), there were scattered small residual droplets on the surface when they hit or bounce off the surface. These daughter droplets would gradually freeze on the surface and became larger ice nucleation sites. As the icing area on the surface increased to a certain extent, the water droplets could no longer bounce and slid on the surface. This is one of the issues for the PTFE-TENG working in low temperature environments. As expected, PFPE-infused SLIPS provided a low contact hysteresis owing to a high spreading velocity, which greatly reduced the possibility of ice nucleation in the movement process. Meanwhile, the SLIPS surface was covered by a layer of protective lubricant, which further reduced nucleation on the surface. These are the main reasons why PFPE-infused SLIPS-SE-TENG can work normally in low-temperature environments. However, it should be noted that this type of surface is might subject to failure under extreme temperatures, as tested at -13℃ (Fig. 5.16).

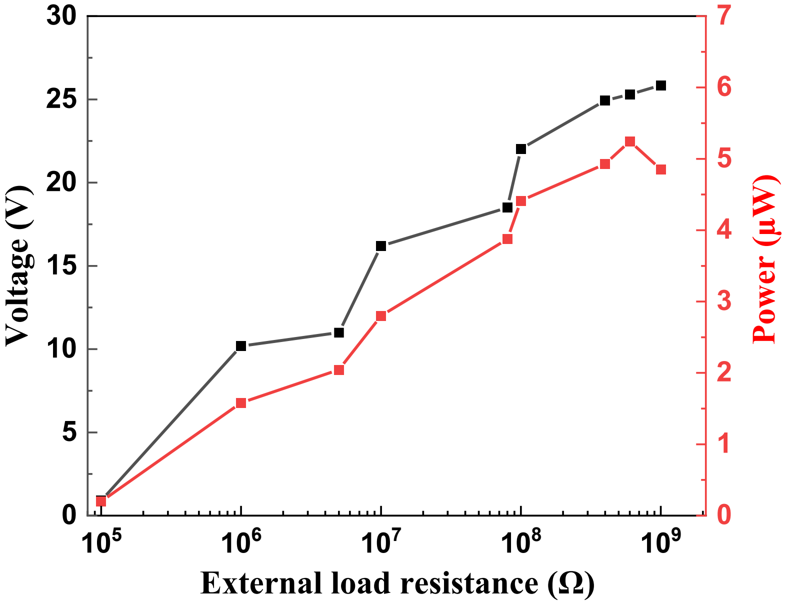

Figure 5.14: Output voltage and output power of SLIPS-SE-TENG as a function of load resistance. (4 μL/cm^2 PFPE, Height=4 cm, T=-5℃, Humidity=40%)

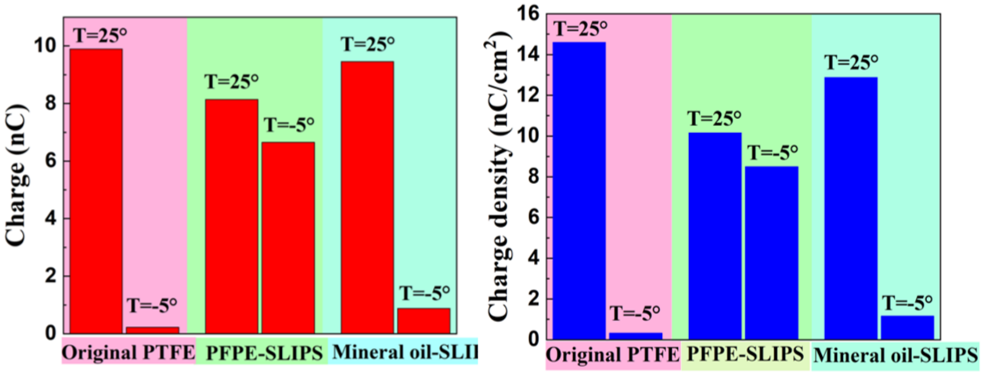

Figure 5.15: The transferred charges (left) and charge density (right) of water droplet on surfaces with various environmental temperatures. (4 μL/cm^2 PFPE, Height=4cm, Humidity=40%)

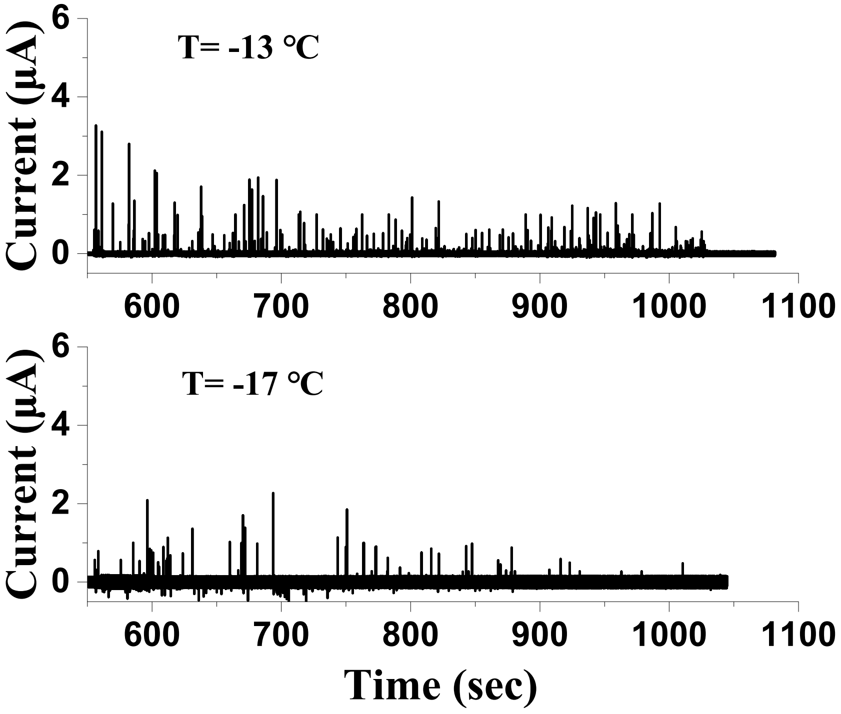

Figure 5.16: SLIPS-SE-TENG short-circuit current output at extra low temperatures.

Within the extension of the test time, the frequency of the current peaks decreased slightly at lower temperature, -5°C (Fig. 5.13b) compared to that at room temperature. This phenomenon is possibly attributed to the consumption of surface lubricant. Icing can occur in some PTFE-exposed areas, which reduced the probability for the droplet to reach its maximum spreading radius. Even so, it needs to be emphasized that PFPE-SLIPS-TENG can still maintain a relatively stable working state under low temperature conditions. On the other hand, the output current of PFPE-SLIPS-TENG was slightly improved at room temperature (23°C) but remained basically unchanged at low temperature (-5°C), as shown in Fig. 5.13b. This can be explained by the results discussed next part that showed that the decrease of lubricant on the porous surface led to the enhancement of the performance of SLIPS-TENG because of a stronger CE strength between water-PTFE than water-lubricant. Therefore, it is most likely that the lubricant loss rate was related to temperature (Fig. 5.17). Nonetheless, the reason behind is out of the scope of this study but worth studying by in-depth exploration in the future. On the other hand, it is worth noting that operation at high temperature (e.g., T=55 ℃) did not affect the output efficiency of SLIPS-SE-TENG (Fig. 5.18). SLIPS also has been known to perform well under high/low pressure conditions, as reported in the literature.[146, 166] Therefore, it is reasonable to assume that SLIPS-SE-TENG should function normally under high/low pressure although further research is necessary for a detailed confirmation and discussion.

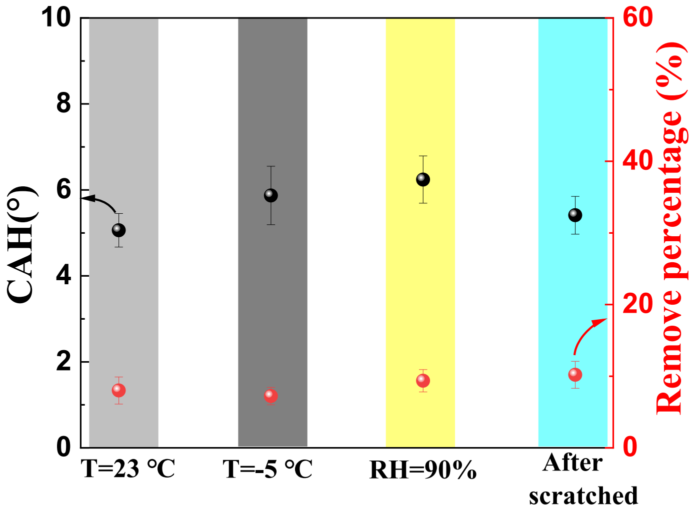

Figure 5.17: Contact angle hysteresis (CAH) and weight difference of PFPE-infused SLIPS after the continues drop sliding for 60 min.

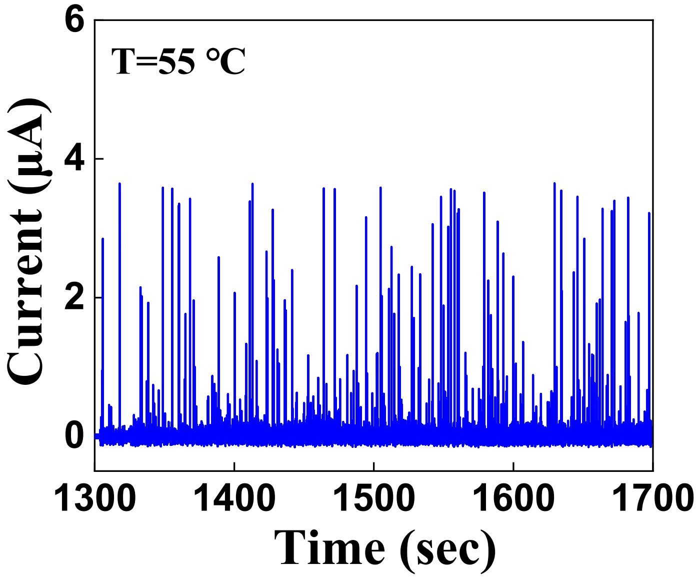

Figure 5.18: PFPE-infused SLIPS-SE-TENG short-circuit current at T= 55°C (H=4 cm, RH=40%)

SLIPS shows advanced performance that are normally associated with conventional gas-cushioned superhydrophobic surfaces. However, SLIPS can lose their novel properties if the infused liquid drains out, leaving uncovered substrates exposed to air. Therefore, tremendous efforts have been made to maintain the durability of SLIPS. One common strategy would be the construction of 3-dimensional lubricant infused surface (3D-SLIPS), where inherent porosity of a 3D molecular network is used to trap and to store the lubricant liquid[103, 167]. By using 3D-SLIPS, the stored lubricant can replenish the lubricant lost on the surface during the time when the falling water drops impact and consume lubricant oils. On the other hand, a recent theory also suggests a method by which any existing patterned surface may be made resistant to shear-driven lubricant drainage.[168] Both approaches mentioned above have great potential to improve the durability of SLIPS, which also requires more fundamental and systematic research in the future.

Surface self-healing is one of the most important capabilities to improve the applicability of the TENG in an outdoor work environment. Especially, in harsh geographical environments—such as deserts or even Mars—inhospitable for human activity. Figs. 5.13e & 5.13f recorded the movements of water drop on the PFPE-infused SLIPS and the pristine PTFE surface after those surfaces were scratched at the same degree, respectively. As shown in Fig. 5.13e, there was no obvious hindrance to the movement of the water drops on the scratched PFPE-infused SLIPS. On the contrary, the scratch of the original PTFE surface directly impeded the fully spreading of the water drops, and parts of the small residual droplets were pinned at the scratched positions after leaving (Fig. 5.13)). Owing to the instability of the spread of the water drops, there was no stable, consistent current output in the scratched PTFE surface, while the output behaved as usual for the SLIPS-SE-TENG after being scratched. (Fig. 5.19) The main reason for this difference is that PFPE-infused SLIPS showed a strong surface self-healing ability, as shown in Fig. 5.13g. The SLIPS surface repaired quickly after being scratched, without any adverse effect on the movement of water droplets on its surface. Moreover, the transmittance of the PFPE-infused SLIPS used above was significantly higher than that of neat PTFE, as shown in Fig. 5.13g. The transparent TENG device exhibited promising potential to cooperate with photovoltaic power generation for working in all-climate environments. Dust proofing is also an important aspect when considering applications in harsh environments. However, due to the nature of SLIPS, comprising an oil layer, the system would show self-cleaning against hydrophilic dust while hydrophobic dust would produce a negative impact. The development of dust-proof, all-weather SLIPS-SE-TENG is a topic that requires further investigation.

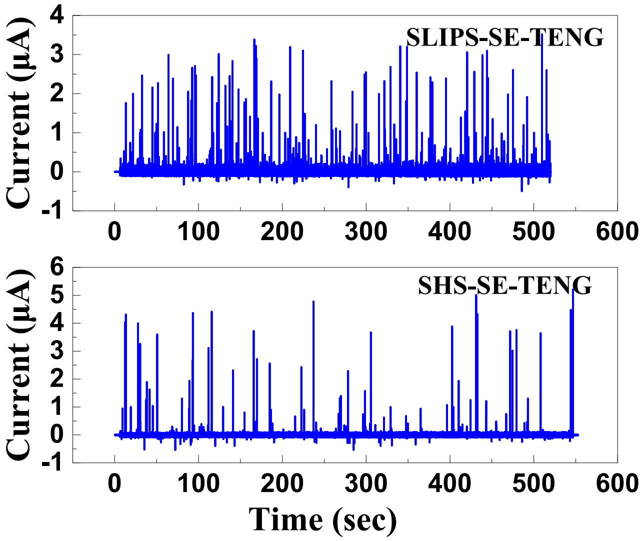

Figure 5.19: The short-circuit current of SLIPS-SE-TENG and SHS-SE-TENG with CE surface after being scratched. (H=4 cm, tilt angle=35°, temperature=23°C, humidity=40%)

SLIPS-SE-TENG also displayed significant advantages over the traditional TENG in high-humidity environments, making it attractive for applications applied in rainforest areas.

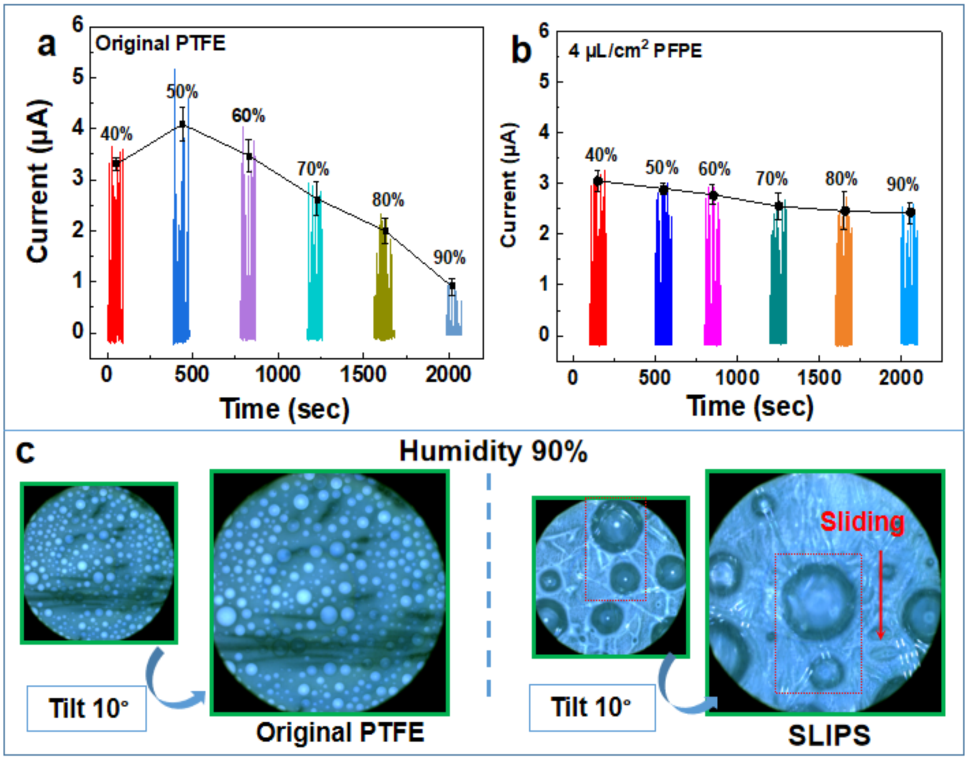

Figure 5.20: Influence of environmental humidity on the performance of the SE-TENG formed by the (a) original PTFE surface and (b) 4 µL/cm^2 PFPE-infused SLIPS. (c) Distribution of residual micro-droplets on the surface in a high-humidity environment (~90%) before and after surface tilt by 10°.

Humidity has a significant influence on the output performance of the SE-TENG integrated by different surfaces, as shown in Fig. 5.20. For the pristine PTFE surface (Fig. 5.20a), the performance of the SE-TENG was significantly deteriorated with an increase in the air humidity, especially when the humidity became greater than 50%. The short-circuit current decreased from 4 µA (humidity ~50%) to about 1 µA (humidity ~90%). The slight increase in neat PTFE performance at a humidity in the 40% – 50% range was consistent with the results reported by Hu *et al.*[169] In suitable humidity conditions (*e.g.*, humidity ~50%), a small amount of water molecules possibly adsorbed onto the neat PTFE surface,[170] which is beneficial for reducing the frictional resistance between water drops and the surface, thereby increasing the contact area between water and the SLIPS (Fig. 5.21).However, there was still a clear trend showing that performance of the SE-TENG using neat PTFE was inhibited in conditions of high humidity.

Meanwhile, humidity variances showed negligible influence on the performance of the PFPE-infused SLIPS-SE-TENG, as shown in Fig. 5.20b. This is because the SLIPS has an extremely low lateral force on water drops, which prevents their accumulation. As shown in Fig. 5.20c, the surface of the neat PTFE was always densely covered with nano-micron droplets. As a comparison, (Fig. 5.20c), only a few large-size water droplets were visible on the PFPE-infused SLIPS under high humidity conditions. Even if a small number of droplets stayed on the surface, these droplets condensed quickly[160] then slipped off the surface with an incline angle of 10° (or tilt angle of 90° in Fig. 5.22). Fewer water droplets condensed and pinned on PFPE-infused SLIPS even at a high air humidity (~90%), which is one of the possible reasons why the performance of PFPE-infused the SLIPS-SE-TENG remained generally unaffected by the environmental humidity. On the other hand, it is worth noting the low friction and easily removable water droplets on the surface of PFPE-SLIPS, which also may also contribute to the superior current output of PFPE-SE-TENG. High adaptability in harsh environments and high light transmittance enabled the use of a slippery surface, making it possible to integrate the SLIPS-SE-TENG with other devices such as solar cells to simultaneously collect both the droplet and solar energy.

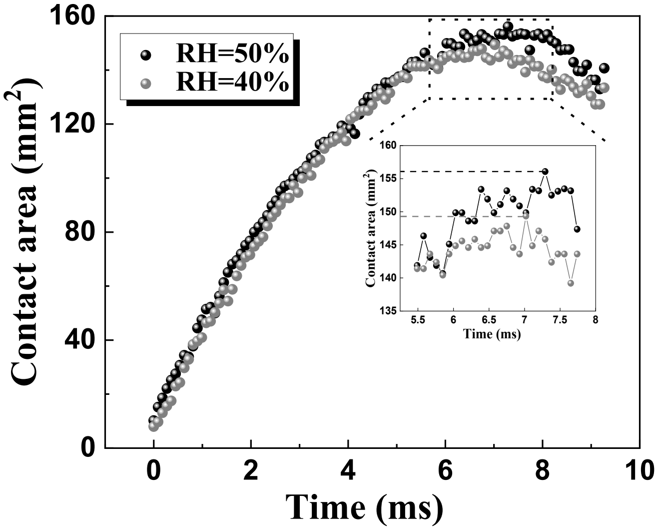

Figure 5.21: Relationship between air humidity and contact diameter of sliding water droplets on SLIPS (Height=8 cm, 4 μL/cm^2 PFPE-infused SLIPS, T=23°C)

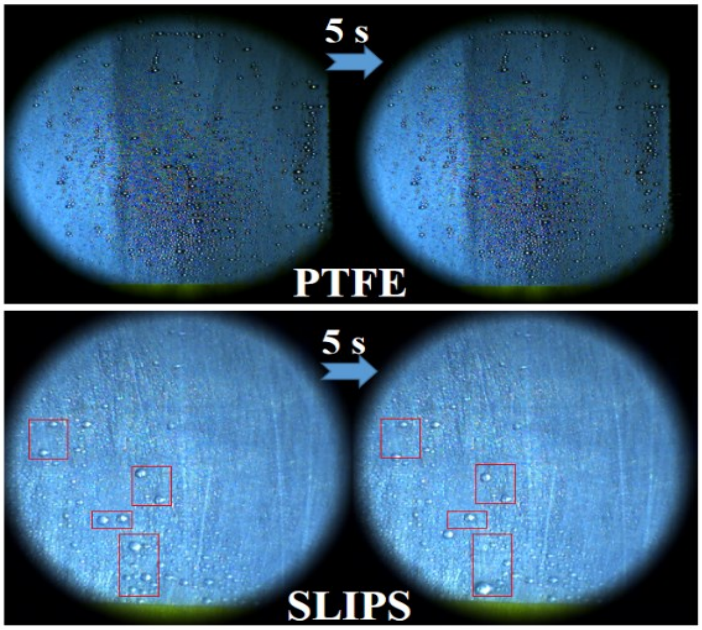

Figure 5.22: Water droplets distribution on virgin PTFE and PFPE-SLIPS (4 μL/cm^2 PFPE) in a custom humidity-controlled chamber (RH = 90%). The sample is with 90° tilt angle.

5.5 Summary

In summary, in this chapter, we developed an all-weather triboelectric nanogenerator based on slippery surfaces. Our theoretical calculations and experimental results showed that the volume and type of the infusing lubricant are key factors for achieving an optimal SLIPS-SE-TENG performance. PTFE substrates (thickness 20 μm and average pore size 450 nm) infused with 4 $\mu L/cm^2$ PFPE were shown to be the best choice for fabricating the SLIPS system for operation at a droplet's moving velocity > 0.3 mm/s. Such conditions afforded low CAH, self-healing and high light transmittance. The output performance of SLIPS-SE-TENG was further improved when the electrode was connected to the middle position of the maximum spread droplet and the falling drop height was increased. The integrated transistor-inspired architecture SLIPS-SE-TENG collected an instantaneous short-circuit current, in the microampere level, and provided a maximum power output of 5 μW, a considerably higher value compared to recent reports, 0.2 μW [151]. More importantly, by contrast to SHS-SE-TENG, our introduced SLIPS-SE-TENG device worked normally and stably in harsh environments, such as in low temperatures (T~ -5°C) and high relative humidity (RH~ 90%). The combination of SLIPS and SE-TENG is expected to open a new way for the rational design of durable energy harvesting devices.

Chapter 6

Conclusions

6.1 Contributions to knowledge

The major contributions of this thesis to science and engineering are listed in this chapter. We revealed the influence of the curvature effect on contact electrification in the liquid-solid made TENG at the nanoscale level. EFM results showed that the convex surface (negative curvature) is more conducive to the electron transfer with liquid drops than that of the concave surface (positive curvature). A statistical trend was found that a smaller curvature would typically lead to a higher charging rate of negative charges after CE. After contact separation, the charge transfer from the surface to the atmosphere followed an exponential decay at a fixed temperature. Differently from the curvature effect on triboelectric charge generation, the charges on the concave surface were more likely to be emitted into the atmosphere than those on the convex surface. Based on these experimental results, we proposed a curvature-dependent charge transfer model for distinct materials CE by introducing the curvature-induced energy shifts of the surface states. The short-circuit current output performance of TENG was found to be greatly improved by introducing more nano-layer structure on the insulating surface, which increases the convex coverage of the surface. TENG using the surface with more negative curvatures showed the best performance, suggesting that the convex surface led to more electrons negatively charging the surface. These results strongly supported our theory about the curvature effect in the nanoscale. Our study has not only provided a new insight on the understanding the CE but also found an effective way to enhance the output performance of drop-based TENG.

We also integrated the slippery interface with transistor-inspired architecture for a robust triboelectric nanogenerator. Theoretical calculations and experimental results showed that the property and volume of infused lubricants are the key factors for achieving excellent SLIPS-SE-TENG performance. When PTFE is used as the substrate, 4 μL/cm^2 PFPE is the best choice for fabricating SLIPS, which had characteristics of low CAH, self-healing, high light transmittance, and strong resistance to harsh environments. The integrated transistor-inspired architecture SLIPS-SE-TENG directly enhanced the instantaneous short-circuit current (~3 μA) by two orders of magnitude over equivalent devices (~0.02 μA) that are limited by interfacial effects. More importantly, compared to SHS-TENG, this novel SLIPS-SE-TENG device can work normally and stably in harsh environments, such as low temperature and high humidity. The combination of SLIPS and TENG may open a new way for the rational design of new energy equipment, which can harvest a large amount of energy under a harsh environment and has good stability and durability.

6.2 Suggestions for future work

According to the laboratory's equipment configuration and existing experimental results, it allows us to further study the surface properties of SLIPS and its application in various fields, such as TENG, ship hull corrosion resistance and so on. The specific proposed research are as follows:

For SLIPS with an extra-low contact angle hysteresis, which was hypothesized to arise from a thin lubricant overlayer film sandwiched between the droplet and solid substrate but has not been observed experimentally. In our lab, using thin-film interference (dynamic force apparatus, DFA), we can visualize the interfacial film under both static and dynamic conditions. When the droplets come into contact with SLIPS in free fall, under the impact of huge potential energy, will the oil layer on the surface of SLIPS be squeezed out by the water droplets, so that the droplets directly contact the substrate? The specific experimental and theoretical analysis ideas are given as:

Through the displacement control module of DFA, the droplet is controlled to descend at different displacement speeds (simulating the free fall of the droplet) to contact the SLIPS. The dynamic changes of thin film fringes between SLIPS and droplets can be recorded by a high-speed camera, and then the thickness of the oil layer during the droplet impact on SLIPS can be calculated using MATLAB based on thin film interference theory.

Obviously, if the droplet hits the SLIPS with a high displacement velocity, the water droplet dislodges the oil layer and directly contacts the substrate, which will lead to the failure of the SLIPS. Therefore, studying the variation of SLIPS oil layer thickness under different conditions (temperature, pressure, etc.) by DFA is an important feature for evaluating SLIPS performance.

One of the other urgently needed features for further improvements of SLIPS is that the surface oil layer will always dissipate to varying degrees, which hinders the commercial application of SLIPS. Based on our existing research, 1D-SLIS was found to be a potentially effective option for lubricating surfaces. 1D-SLIS is a class of self-assembly monolayer surface (SAMs), e.g., PDMS coating. Such coatings are highly lubricated and durable. However, there are currently unresolved problems in the development and production of such 1D-SLIS surfaces. For example, due to the influence of air humidity, the adsorption layer of SAMs tends to be disordered, which seriously affects the lubricating performance of the 1D-SLIS. A completely dry environment was proved to be a perfect solution to solve this problem, but the high cost has hindered the industrialization of this technology. Therefore, finding low cost and efficient method for chemically uniform 1D-SLIS production is one of the priorities of our work in the future.

References

[1] S. Lin, X. Chen, Z.L. Wang, Contact Electrification at the Liquid–Solid Interface, Chemical Reviews (2021).

[2] B. Terris, J. Stern, D. Rugar, H. Mamin, Contact electrification using force microscopy, Physical Review Letters 63(24) (1989) 2669.

[3] H.W. Gibson, Linear free energy relations. V. triboelectric charging of organic solids, Journal of the American Chemical Society 97(13) (1975) 3832-3833.

[4] C. Liu, A.J. Bard, Electrostatic electrochemistry at insulators, Nature materials 7(6) (2008) 505-509.

[5] L.S. McCarty, G.M. Whitesides, Electrostatic charging due to separation of ions at interfaces: contact electrification of ionic electrets, Angewandte Chemie International Edition 47(12) (2008) 2188-2207.

[6] C. Duke, T. Fabish, Contact electrification of polymers: A quantitative model, Journal of Applied Physics 49(1) (1978) 315-321.

[7] A. Šutka, K. Mālnieks, L. Lapčinskis, P. Kaufelde, A. Linarts, A. Bērziņa, R. Zābels, V. Jurķāns, I. Gorņevs, J. Blūms, The role of intermolecular forces in contact electrification on polymer surfaces and triboelectric nanogenerators, Energy & Environmental Science 12(8) (2019) 2417-2421.

[8] H. Baytekin, A. Patashinski, M. Branicki, B. Baytekin, S. Soh, B.A. Grzybowski, The mosaic of surface charge in contact electrification, Science 333(6040) (2011) 308-312.

[9] S. Li, Y. Zhou, Y. Zi, G. Zhang, Z.L. Wang, Excluding contact electrification in surface potential measurement using kelvin probe force microscopy, ACS nano 10(2) (2016) 2528-2535.

[10] H. Sun, H. Chu, J. Wang, L. Ding, Y. Li, Kelvin probe force microscopy study on nanotriboelectrification, Applied Physics Letters 96(8) (2010) 083112.

[11] R. Sanikop, N. Arya, V. Balakrishnan, C. Sudakar, Charge Pumping by Contact Electrification Using Electrostatic Force Microscopy in Bi-and Trilayered MoS2 Nanosheets, The Journal of Physical Chemistry C (2021).

[12] G. Wang, Y. Xi, H. Xuan, R. Liu, X. Chen, L. Cheng, Hybrid nanogenerators based on triboelectrification of a dielectric composite made of lead-free ZnSnO3 nanocubes, Nano Energy 18 (2015) 28-36.

[13] L. Zhang, X. Li, Y. Zhang, Y. Feng, F. Zhou, D. Wang, Regulation and influence factors of triboelectricity at the solid-liquid interface, Nano Energy 78 (2020) 105370.

[14] X. Li, L. Zhang, Y. Feng, X. Zhang, D. Wang, F. Zhou, Solid–liquid triboelectrification control and antistatic materials design based on interface wettability control, Advanced Functional Materials 29(35) (2019) 1903587.

[15] S. Lin, L. Xu, L. Zhu, X. Chen, Z.L. Wang, Electron transfer in nanoscale contact electrification: photon excitation effect, Advanced Materials 31(27) (2019) 1901418.

[16] B.J. Brenny, A. Polman, F.J.G. de Abajo, Femtosecond plasmon and photon wave packets excited by a high-energy electron on a metal or dielectric surface, Physical Review B 94(15) (2016) 155412.

[17] S. Lin, L. Xu, C. Xu, X. Chen, A.C. Wang, B. Zhang, P. Lin, Y. Yang, H. Zhao, Z.L. Wang, Electron transfer in nanoscale contact electrification: effect of temperature in the metal–dielectric case, Advanced Materials 31(17) (2019) 1808197.

[18] C. Xu, A.C. Wang, H. Zou, B. Zhang, C. Zhang, Y. Zi, L. Pan, P. Wang, P. Feng, Z. Lin, Raising the working temperature of a triboelectric nanogenerator by quenching down electron thermionic emission in contact-electrification, Advanced Materials 30(38) (2018) 1803968.

[19] P. Wang, S. Zhang, L. Zhang, L. Wang, H. Xue, Z.L. Wang, Non-contact and liquid–liquid interfacing triboelectric nanogenerator for self-powered water/liquid level sensing, Nano Energy 72 (2020) 104703.

[20] J. Zhang, S. Lin, M. Zheng, Z.L. Wang, Triboelectric Nanogenerator as a Probe for Measuring the Charge Transfer between Liquid and Solid Surfaces, ACS nano (2021).

[21] M.F. Hsu, E.R. Dufresne, D.A. Weitz, Charge stabilization in nonpolar solvents, Langmuir 21(11) (2005) 4881-4887.

[22] S.K. Sainis, V. Germain, C.O. Mejean, E.R. Dufresne, Electrostatic interactions of colloidal particles in nonpolar solvents: Role of surface chemistry and charge control agents, Langmuir 24(4) (2008) 1160-1164.

[23] J. Wang, H. Wang, X. Li, Y. Zi, Self-powered electrowetting optical switch driven by a triboelectric nanogenerator for wireless sensing, Nano Energy 66 (2019) 104140.

[24] N. Mendel, H. Wu, F. Mugele, Electrowetting-assisted generation of ultrastable high charge densities in composite silicon oxide–fluoropolymer electret samples for electric nanogenerators, Advanced Functional Materials 31(11) (2021) 2007872.

[25] S. Chen, N. Wang, L. Ma, T. Li, M. Willander, Y. Jie, X. Cao, Z.L. Wang, Triboelectric nanogenerator for sustainable wastewater treatment via a self-powered electrochemical process, Advanced Energy Materials 6(8) (2016) 1501778.

[26] J. Zhang, M.L. Coote, S. Ciampi, Electrostatics and Electrochemistry: Mechanism and Scope of Charge-Transfer Reactions on the Surface of Tribocharged Insulators, Journal of the American Chemical Society 143(8) (2021) 3019-3032.

[27] Y. Wang, X. Yang, X. Yu, J. Duan, Q. Yang, Y. Duan, Q. Tang, Triboelectric charging behaviors and photoinduced enhancement of alkaline earth ions doped inorganic perovskite triboelectric nanogenerators, Nano Energy 77 (2020) 105280.

[28] L. Han, X. Zhao, M. Ma, F. Gao, X. Xun, Q. Liao, Z. Zhang, Z. Kang, Y. Zhang, Self-powered visualization system by conjunction of photovoltaic effect and contact-electrification, Nano Energy 57 (2019) 528-534.

[29] A. El-Kazzaz, A. Rose-Innes, Contact charging of insulators by liquid metals, Journal of Electrostatics 16(2-3) (1985) 157-163.

[30] M. Matsui, N. Murasaki, K. Fujibayashi, P.Y. Bao, Y. Kishimoto, Electrification of pure water flowing down a trough set up with a resin sheet, Journal of electrostatics 31(1) (1993) 1-10.

[31] K. Yatsuzuka, Y. Mizuno, K. Asano, Electrification phenomena of pure water droplets dripping and sliding on a polymer surface, Journal of electrostatics 32(2) (1994) 157-171.

[32] T.A. Burgo, F. Galembeck, G.H. Pollack, Where is water in the triboelectric series?, Journal of Electrostatics 80 (2016) 30-33.

[33] F. Galembeck, T.A. Burgo, L.B. Balestrin, R.F. Gouveia, C.A. Silva, A. Galembeck, Friction, tribochemistry and triboelectricity: recent progress and perspectives, Rsc Advances 4(109) (2014) 64280-64298.

[34] Z.L. Wang, A.C. Wang, On the origin of contact-electrification, Materials Today 30 (2019) 34-51.

[35] V. Vallem, Y. Sargolzaeiaval, M. Ozturk, Y.C. Lai, M.D. Dickey, Energy harvesting and storage with soft and stretchable materials, Advanced Materials 33(19) (2021) 2004832.

[36] A. Andrawis, J. Santiago, Development of a hydrazine/nitrogen dioxide fiber optic sensor, John F. Kennedy Space Center/University of Central Florida 2003 NASA/ASEE Summer Faculty Fellowship Reports (2003).

[37] F.-R. Fan, Z.-Q. Tian, Z.L. Wang, Flexible triboelectric generator, Nano energy 1(2) (2012) 328-334.

[38] S. Lin, L. Xu, A.C. Wang, Z.L. Wang, Quantifying electron-transfer in liquid-solid contact electrification and the formation of electric double-layer, Nature communications 11(1) (2020) 1-8.

[39] Z. Chen, Y. Lu, R. Manica, Q. Liu, Curvature effect in liquid-solid contact electrification, Nano Energy (2021) 106456.

[40] S. Lin, Z.L. Wang, Scanning triboelectric nanogenerator as a nanoscale probe for measuring local surface charge density on a dielectric film, Applied Physics Letters 118(19) (2021) 193901.

[41] M. Willatzen, L.C. Lew Yan Voon, Z.L. Wang, Quantum theory of contact electrification for fluids and solids, Advanced Functional Materials 30(17) (2020) 1910461.

[42] M. Sun, Q. Lu, Z.L. Wang, B. Huang, Understanding contact electrification at liquid–solid interfaces from surface electronic structure, Nature communications 12(1) (2021) 1-11.

[43] P. Degen, E. Zwar, M. Paulus, M. Tolan, H. Rehage, About the Role of Surfactants on the Magnetic Control over Liquid Interfaces, Langmuir 30(39) (2014) 11563-11566. https://doi.org/10.1021/la503142q.

[44] Z.L. Wang, Triboelectric nanogenerators as new energy technology for self-powered systems and as active mechanical and chemical sensors, ACS nano 7(11) (2013) 9533-9557.

[45] W. Tang, B. Meng, H. Zhang, Investigation of power generation based on stacked triboelectric nanogenerator, Nano Energy 2(6) (2013) 1164-1171.

[46] K.Y. Lee, M.K. Gupta, S.-W. Kim, Transparent flexible stretchable piezoelectric and triboelectric nanogenerators for powering portable electronics, Nano Energy 14 (2015) 139-160.

[47] Z.L. Wang, J. Chen, L. Lin, Progress in triboelectric nanogenerators as a new energy technology and self-powered sensors, Energy & Environmental Science 8(8) (2015) 2250-2282.

[48] S. Kim, M.K. Gupta, K.Y. Lee, A. Sohn, T.Y. Kim, K.S. Shin, D. Kim, S.K. Kim, K.H. Lee, H.J. Shin, Transparent flexible graphene triboelectric nanogenerators, Advanced materials 26(23) (2014) 3918-3925.

[49] S. Park, H. Kim, M. Vosgueritchian, S. Cheon, H. Kim, J.H. Koo, T.R. Kim, S. Lee, G. Schwartz, H. Chang, Stretchable energy-harvesting tactile electronic skin capable of differentiating multiple mechanical stimuli modes, Advanced Materials 26(43) (2014) 7324-7332.

[50] Z.H. Lin, G. Cheng, L. Lin, S. Lee, Z.L. Wang, Water-Solid Surface Contact Electrification and its Use for Harvesting Liquid-Wave Energy, Angewandte Chemie-International Edition 52(48) (2013) 12545-12549. https://doi.org/10.1002/anie.201307249.

[51] X. Li, J. Tao, X. Wang, J. Zhu, C. Pan, Z.L. Wang, Networks of High Performance Triboelectric Nanogenerators Based on Liquid-Solid Interface Contact Electrification for

Harvesting Low-Frequency Blue Energy, Advanced Energy Materials 8(21) (2018). https://doi.org/10.1002/aenm.201800705.

[52] Z.-H. Lin, G. Cheng, L. Lin, S. Lee, Z.L. Wang, Water-Solid Surface Contact Electrification and its Use for Harvesting Liquid-Wave Energy, Angewandte Chemie-International Edition 52(48) (2013) 12545-12549. https://doi.org/10.1002/anie.201307249.

[53] W. Tang, T. Jiang, F.R. Fan, A.F. Yu, C. Zhang, X. Cao, Z.L. Wang, Liquid-Metal Electrode for High-Performance Triboelectric Nanogenerator at an Instantaneous Energy Conversion Efficiency of 70.6%, Advanced Functional Materials 25(24) (2015) 3718-3725. https://doi.org/10.1002/adfm.201501331.

[54] J. Chen, W. Tang, C. Lu, L. Xu, Z. Yang, B. Chen, T. Jiang, Z.L. Wang, Characteristics of triboelectrification on dielectric surfaces contacted with a liquid metal in different gases, Applied Physics Letters 110(20) (2017). https://doi.org/10.1063/1.4983353.

[55] G. Zhu, Y. Su, P. Bai, J. Chen, Q. Jing, W. Yang, Z.L. Wang, Harvesting Water Wave Energy by Asymmetric Screening of Electrostatic Charges on a Nanostructured Hydrophobic Thin-Film Surface, Acs Nano 8(6) (2014) 6031-6037. https://doi.org/10.1021/nn5012732.

[56] Z.-H. Lin, G. Cheng, S. Lee, K.C. Pradel, Z.L. Wang, Harvesting Water Drop Energy by a Sequential Contact-Electrification and Electrostatic-Induction Process, Advanced Materials 26(27) (2014) 4690-+. https://doi.org/10.1002/adma.201400373.

[57] B. Ravelo, F. Duval, S. Kane, B. Nsom, Demonstration of the triboelectricity effect by the flow of liquid water in the insulating pipe, Journal of Electrostatics 69(6) (2011) 473-478. https://doi.org/10.1016/j.elstat.2011.06.004.

[58] T. Takahashi, MEASUREMENT OF ELECTRIC CHARGE OF CLOUD DROPLETS, DRIZZLE, AND RAINDROPS, Reviews of Geophysics 11(4) (1973) 903-924. https://doi.org/10.1029/RG011i004p00903.

[59] X.J. Zhao, S.Y. Kuang, Z.L. Wang, G. Zhu, Highly Adaptive Solid-Liquid Interfacing Triboelectric Nanogenerator for Harvesting Diverse Water Wave Energy, Acs Nano 12(5) (2018) 4280-4285. https://doi.org/10.1021/acsnano.7b08716.

[60] W. Xu, H. Zheng, Y. Liu, X. Zhou, C. Zhang, Y. Song, X. Deng, M. Leung, Z. Yang, R.X. Xu, Z.L. Wang, X.C. Zeng, Z. Wang, A droplet-based electricity generator with high instantaneous power density, Nature 578(7795) (2020) 392-+. https://doi.org/10.1038/s41586-020-1985-6.

[61] A.K.M. Newaz, D.A. Markov, D. Prasai, K.I. Bolotin, Graphene Transistor as a Probe for Streaming Potential, Nano Letters 12(6) (2012) 2931-2935. https://doi.org/10.1021/nl300603v.

[62] B. Zhang, L. Zhang, W. Deng, L. Jin, F. Chun, H. Pan, B. Gu, H. Zhang, Z. Lv, W. Yang, Z.L. Wang, Self-Powered Acceleration Sensor Based on Liquid Metal Triboelectric Nanogenerator for Vibration Monitoring, Acs Nano 11(7) (2017) 7440-7446. https://doi.org/10.1021/acsnano.7b03818.

[63] Y. Yang, N. Sun, Z. Wen, P. Cheng, H. Zheng, H. Shao, Y. Xia, C. Chen, H. Lan, X. Xie, C. Zhou, J. Zhong, X. Sun, S.-T. Lee, Liquid-Metal-Based Super-Stretchable and Structure-Designable Triboelectric Nanogenerator for Wearable Electronics, Acs Nano 12(2) (2018) 2027-+. https://doi.org/10.1021/acsnano.8b00147.

[64] L. Zheng, Z.-H. Lin, G. Cheng, W. Wu, X. Wen, S. Lee, Z.L. Wang, Silicon-based hybrid cell for harvesting solar energy and raindrop electrostatic energy, Nano Energy 9 (2014) 291-300. https://doi.org/10.1016/j.nanoen.2014.07.024.

[65] Z.L. Wang, New wave power, Nature 542(7640) (2017) 159-160. https://doi.org/10.1038/542159a.

[66] X.J. Zhao, G. Zhu, Y.J. Fan, H.Y. Li, Z.L. Wang, Triboelectric Charging at the Nanostructured Solid/Liquid Interface for Area-Scalable Wave Energy Conversion and Its Use in Corrosion Protection, Acs Nano 9(7) (2015) 7671-7677. https://doi.org/10.1021/acsnano.5b03093.

[67] X.J. Zhao, J.J. Tian, S.Y. Kuang, H. Ouyang, L. Yan, Z.L. Wang, Z. Li, G. Zhu, Biocide-Free Antifouling on Insulating Surface by Wave-Driven Triboelectrification-Induced Potential Oscillation, Advanced Materials Interfaces 3(17) (2016). https://doi.org/10.1002/admi.201600187.

[68] Y. Xi, H. Guo, Y. Zi, X. Li, J. Wang, J. Deng, S. Li, C. Hu, X. Cao, Z.L. Wang, Multifunctional TENG for Blue Energy Scavenging and Self-Powered Wind-Speed Sensor, Advanced Energy Materials 7(12) (2017). https://doi.org/10.1002/aenm.201602397.

[69] N. Zhai, Z. Wen, X. Chen, A. Wei, M. Sha, J. Fu, Y. Liu, J. Zhong, X. Sun, Blue Energy Collection toward All-Hours Self-Powered Chemical Energy Conversion, Advanced Energy Materials 10(33) (2020). https://doi.org/10.1002/aenm.202001041.

[70] Z. Wen, H. Guo, Y. Zi, M.-H. Yeh, X. Wang, J. Deng, J. Wang, S. Li, C. Hu, L. Zhu, Z.L. Wang, Harvesting Broad Frequency Band Blue Energy by a Triboelectric-Electromagnetic Hybrid Nanogenerator, ACS Nano 10(7) (2016) 6526-6534. https://doi.org/10.1021/acsnano.6b03293.

[71] L. Chen, Q. Shi, Y. Sun, T. Nguyen, C. Lee, S. Soh, Controlling surface charge generated by contact electrification: strategies and applications, Advanced Materials 30(47) (2018) 1802405.

[72] C. Xu, B. Zhang, A.C. Wang, H. Zou, G. Liu, W. Ding, C. Wu, M. Ma, P. Feng, Z. Lin, Contact-electrification between two identical materials: curvature effect, ACS nano 13(2) (2019) 2034-2041.

[73] D. Tan, M. Willatzen, Z.L. Wang, Electron transfer in the contact-electrification between corrugated 2D materials: A first-principles study, Nano Energy 79 (2021) 105386.

[74] K. Zhao, Z.L. Wang, Y. Yang, Self-powered wireless smart sensor node enabled by an ultrastable, highly efficient, and superhydrophobic-surface-based triboelectric nanogenerator, ACS nano 10(9) (2016) 9044-9052.

[75] J. Ahn, Z.-J. Zhao, J. Choi, Y. Jeong, S. Hwang, J. Ko, J. Gu, S. Jeon, J. Park, M. Kang, D.V. Del Orbe, I. Cho, H. Kang, M. Bok, J.-H. Jeong, I. Park, Morphology-controllable wrinkled hierarchical structure and its application to superhydrophobic

triboelectric nanogenerator, Nano Energy 85 (2021). https://doi.org/10.1016/j.nanoen.2021.105978.

[76] S. Lee, J. Chung, D.Y. Kim, J.-Y. Jung, S.H. Lee, S. Lee, Cylindrical water triboelectric nanogenerator via controlling geometrical shape of anodized aluminum for enhanced electrostatic induction, ACS applied materials & interfaces 8(38) (2016) 25014-25018.

[77] T.-S. Wong, S.H. Kang, S.K.Y. Tang, E.J. Smythe, B.D. Hatton, A. Grinthal, J. Aizenberg, Bioinspired self-repairing slippery surfaces with pressure-stable omniphobicity, Nature 477(7365) (2011) 443-447. https://doi.org/10.1038/nature10447.

[78] H.F. Bohn, W. Federle, Insect aquaplaning: Nepenthes pitcher plants capture prey with the peristome, a fully wettable water-lubricated anisotropic surface, Proceedings of the National Academy of Sciences of the United States of America 101(39) (2004) 14138-14143. https://doi.org/10.1073/pnas.0405885101.

[79] U. Bauer, W. Federle, The insect-trapping rim of Nepenthes pitchers Surface structure and function, Plant Signaling & Behavior 4(11) (2009) 1019-1023. https://doi.org/10.4161/psb.4.11.9664.

[80] A. Lafuma, D. Quere, Slippery pre-suffused surfaces, Epl 96(5) (2011). https://doi.org/10.1209/0295-5075/96/56001.

[81] S.E. Luria, Slippery when wet, Rhode Island medical journal 56(4) (1973) 147-52.

[82] D.J. Preston, Y. Song, Z. Lu, D.S. Antao, E.N. Wang, Design of Lubricant Infused Surfaces, Acs Applied Materials & Interfaces 9(48) (2017) 42383-42392. https://doi.org/10.1021/acsami.7b14311.

[83] S. Anand, A.T. Paxson, R. Dhiman, J.D. Smith, K.K. Varanasi, Enhanced Condensation on Lubricant-Impregnated Nanotextured Surfaces, Acs Nano 6(11) (2012) 10122-10129. https://doi.org/10.1021/nn303867y.

[84] W. Xu, X. Zhou, C. Hao, H. Zheng, Y. Liu, X. Yan, Z. Yang, M. Leung, X.C. Zeng, R.X. Xu, Z. Wang, SLIPS-TENG: robust triboelectric nanogenerator with optical and charge transparency using a slippery interface, National Science Review 6(3) (2019) 540-550. https://doi.org/10.1093/nsr/nwz025.

[85] M.D. Croucher, K.P. Lok, R.W. Wong, S. Drappel, J.M. Duff, A.L. Pundsack, M.L. Hair, USE OF STERICALLY STABILIZED POLYMER COLLOIDS AS ELECTROSTATICALLY-BASED LIQUID DEVELOPERS, Journal of Applied Polymer Science 30(2) (1985) 593-607. https://doi.org/10.1002/app.1985.070300212.

[86] L. Xie, C. Shi, X. Cui, H. Zeng, Surface Forces and Interaction Mechanisms of Emulsion Drops and Gas Bubbles in Complex Fluids, Langmuir 33(16) (2017) 3911-3925. https://doi.org/10.1021/acs.langmuir.6b04669.

[87] J.C. Janson, L. Ryden, PROTEIN PURIFICATION PRINCIPLES HIGH RESOLUTION METHODS AND APPLICATIONS, 1989.

[88] W.H. Briscoe, R.G. Horn, Direct measurement of surface forces due to charging of solids immersed in a nonpolar liquid, Langmuir 18(10) (2002) 3945-3956. https://doi.org/10.1021/la015657s.

[89] M. Farrokhbin, B. Stojimirovic, M. Galli, M.K. Aminian, Y. Hallez, G. Trefalt, Surfactant mediated particle aggregation in nonpolar solvents, Physical Chemistry Chemical Physics 21(35) (2019) 18866-18876. https://doi.org/10.1039/c9cp01985e.

[90] H. Cao, Y. Cheng, P. Huang, M. Qi, Investigation of charging behavior of PS particles in nonpolar solvents, Nanotechnology 22(44) (2011). https://doi.org/10.1088/0957-4484/22/44/445709.

[91] G.N. Smith, J. Eastoe, Controlling colloid charge in nonpolar liquids with surfactants, Physical Chemistry Chemical Physics 15(2) (2013) 424-439. https://doi.org/10.1039/c2cp42625k.

[92] I.D. Morrison, ELECTRICAL CHARGES IN NONAQUEOUS MEDIA, Colloids and Surfaces a-Physicochemical and Engineering Aspects 71(1) (1993) 1-37. https://doi.org/10.1016/0927-7757(93)80026-b.

[93] R.J. Pugh, T. Matsunaga, F.M. Fowkes, THE DISPERSIBILITY AND STABILITY OF CARBON-BLACK IN MEDIA OF LOW DIELECTRIC-CONSTANT .1. ELECTROSTATIC AND STERIC CONTRIBUTIONS TO COLLOIDAL STABILITY, Colloids and Surfaces 7(3) (1983) 183-207. https://doi.org/10.1016/0166-6622(83)80046-8.

[94] S. Poovarodom, J.C. Berg, Effect of particle and surfactant acid-base properties on charging of colloids in apolar media, Journal of Colloid and Interface Science 346(2) (2010) 370-377. https://doi.org/10.1016/j.jcis.2010.03.012.

[95] C.E. McNamee, Y. Tsujii, H. Ohshima, M. Matsumoto, Interaction forces between two hard surfaces in particle-containing aqueous systems, Langmuir 20(5) (2004) 1953-1962. https://doi.org/10.1021/la0357763.

[96] L. Peltonen, J. Hirvonen, J. Yliruusi, The behavior of sorbitan surfactants at the water-oil interface: Straight-chained hydrocarbons from pentane to dodecane as an oil phase, Journal of Colloid and Interface Science 240(1) (2001) 272-276. https://doi.org/10.1006/jcis.2001.7612.

[97] N. Knorr, S. Vinzelberg, Charge writing and detection by EFM and KPFM scanning probe techniques, Microsc Microanal 26 (2012) 7-12.

[98] F. Zhan, A.C. Wang, L. Xu, S. Lin, J. Shao, X. Chen, Z.L. Wang, Electron transfer as a liquid droplet contacting a polymer surface, ACS nano 14(12) (2020) 17565-17573.

[99] S. Lin, M. Zheng, J. Luo, Z.L. Wang, Effects of Surface Functional Groups on Electron Transfer at Liquid–Solid Interfacial Contact Electrification, ACS nano 14(8) (2020) 10733-10741.

[100] H. Zou, L. Guo, H. Xue, Y. Zhang, X. Shen, X. Liu, P. Wang, X. He, G. Dai, P. Jiang, Quantifying and understanding the triboelectric series of inorganic non-metallic materials, Nature communications 11(1) (2020) 1-7.

[101] H. Zou, Y. Zhang, L. Guo, P. Wang, X. He, G. Dai, H. Zheng, C. Chen, A.C. Wang, C. Xu, Quantifying the triboelectric series, Nature communications 10(1) (2019) 1-9.

[102] P. Gupta, B. Kandasubramanian, Directional fluid gating by janus membranes with heterogeneous wetting properties for selective oil–water separation, ACS applied materials & interfaces 9(22) (2017) 19102-19113.

[103] S. Peppou-Chapman, J.K. Hong, A. Waterhouse, C. Neto, Life and death of liquid-infused surfaces: a review on the choice, analysis and fate of the infused liquid layer, Chemical Society Reviews 49(11) (2020) 3688-3715.

[104] X. Chen, G. Wen, Z. Guo, What are the design principles, from the choice of lubricants and structures to the preparation method, for a stable slippery lubricant-infused porous surface?, Materials Horizons 7(7) (2020) 1697-1726.

[105] Z.H. Lin, G. Cheng, L. Lin, S. Lee, Z.L. Wang, Water–solid surface contact electrification and its use for harvesting liquid-wave energy, Angewandte Chemie International Edition 52(48) (2013) 12545-12549.

[106] S. Wang, L. Lin, Z.L. Wang, Nanoscale triboelectric-effect-enabled energy conversion for sustainably powering portable electronics, Nano letters 12(12) (2012) 6339-6346.

[107] S. Wang, L. Lin, Z.L. Wang, Triboelectric nanogenerators as self-powered active sensors, Nano Energy 11 (2015) 436-462.

[108] W. Tang, B.D. Chen, Z.L. Wang, Recent progress in power generation from water/liquid droplet interaction with solid surfaces, Advanced Functional Materials 29(41) (2019) 1901069.

[109] S. Lin, M. Zheng, Z.L. Wang, Detecting the Liquid–Solid Contact Electrification Charges in a Liquid Environment, The Journal of Physical Chemistry C (2021).

[110] W. Harper, The Volta effect as a cause of static electrification, Proceedings of the Royal Society of London. Series A. Mathematical and Physical Sciences 205(1080) (1951) 83-103.

[111] J. Lowell, Contact electrification of metals, Journal of Physics D: Applied Physics 8(1) (1975) 53.

[112] D.A. Hays, Contact electrification between mercury and polyethylene: Effect of surface oxidation, The Journal of Chemical Physics 61(4) (1974) 1455-1462.

[113] C.-y. Liu, A.J. Bard, Electrons on dielectrics and contact electrification, Chemical physics letters 480(4-6) (2009) 145-156.

[114] C. Xu, Y. Zi, A.C. Wang, H. Zou, Y. Dai, X. He, P. Wang, Y.C. Wang, P. Feng, D. Li, On the electron-transfer mechanism in the contact-electrification effect, Advanced materials 30(15) (2018) 1706790.

[115] S.-q. Lin, T.-m. Shao, Bipolar charge transfer induced by water: experimental and first-principles studies, Physical Chemistry Chemical Physics 19(43) (2017) 29418-29423.

[116] T. Burnett, R. Yakimova, O. Kazakova, Mapping of local electrical properties in epitaxial graphene using electrostatic force microscopy, Nano letters 11(6) (2011) 2324-2328.

[117] J. Colchero, A. Gil, A. Baró, Resolution enhancement and improved data interpretation in electrostatic force microscopy, Physical Review B 64(24) (2001) 245403.

[118] S. Sadewasser, T. Glatzel, Kelvin probe force microscopy, Springer2012.

[119] G. Walrafen, Raman and infrared spectral investigations of water structure, The Physics and Physical Chemistry of Water, Springer1972, pp. 151-214.

[120] Y. Sun, X. Huang, S. Soh, Solid-to-Liquid Charge Transfer for Generating Droplets with Tunable Charge, Angewandte Chemie International Edition 55(34) (2016) 9956-9960.

[121] C. Lei, A. Das, M. Elliott, J.E. Macdonald, Quantitative electrostatic force microscopy-phase measurements, Nanotechnology 15(5) (2004) 627.

[122] J.-W. Lee, W. Hwang, Theoretical study of micro/nano roughness effect on water-solid triboelectrification with experimental approach, Nano Energy 52 (2018) 315-322.

[123] Y. Liu, Y. Zheng, T. Li, D. Wang, F. Zhou, Water-solid triboelectrification with self-repairable surfaces for water-flow energy harvesting, Nano Energy 61 (2019) 454-461.

[124] X. Li, L. Zhang, Y. Feng, Y. Zheng, Z. Wu, X. Zhang, N. Wang, D. Wang, F. Zhou, Reversible Temperature-Sensitive Liquid–Solid Triboelectrification with Polycaprolactone Material for Wetting Monitoring and Temperature Sensing, Advanced Functional Materials 31(17) (2021) 2010220.

[125] P. Girard, Electrostatic force microscopy: principles and some applications to semiconductors, Nanotechnology 12(4) (2001) 485.

[126] J. Nie, Z. Ren, L. Xu, S. Lin, F. Zhan, X. Chen, Z.L. Wang, Probing contact-electrification-induced electron and ion transfers at a liquid–solid interface, Advanced Materials 32(2) (2020) 1905696.

[127] X. Zhao, X. Lu, Q. Zheng, L. Fang, L. Zheng, X. Chen, Z.L. Wang, Studying of contact electrification and electron transfer at liquid-liquid interface, Nano Energy (2021) 106191.

[128] K.M. Liu, Relation between charge density and curvature of surface of charged conductor, American Journal of Physics 55(9) (1987) 849-852.

[129] C.X. Lu, C.B. Han, G.Q. Gu, J. Chen, Z.W. Yang, T. Jiang, C. He, Z.L. Wang, Temperature effect on performance of triboelectric nanogenerator, Advanced Engineering Materials 19(12) (2017) 1700275.

[130] L.E. Helseth, The influence of microscale surface roughness on water-droplet contact electrification, Langmuir 35(25) (2019) 8268-8275.

[131] Z.L. Wang, Triboelectric nanogenerators as new energy technology and self-powered sensors–Principles, problems and perspectives, Faraday discussions 176 (2015) 447-458.

[132] U. Khan, S.-W. Kim, Triboelectric nanogenerators for blue energy harvesting, ACS nano 10(7) (2016) 6429-6432.

[133] J. Chen, J. Yang, Z. Li, X. Fan, Y. Zi, Q. Jing, H. Guo, Z. Wen, K.C. Pradel, S. Niu, Networks of triboelectric nanogenerators for harvesting water wave energy: a potential approach toward blue energy, ACS nano 9(3) (2015) 3324-3331.

[134] C. Rodrigues, D. Nunes, D. Clemente, N. Mathias, J. Correia, P. Rosa-Santos, F. Taveira-Pinto, T. Morais, A. Pereira, J. Ventura, Emerging triboelectric nanogenerators for ocean wave energy harvesting: state of the art and future perspectives, Energy & Environmental Science 13(9) (2020) 2657-2683.

[135] K. Dong, X. Peng, Z.L. Wang, Fiber/fabric-based piezoelectric and triboelectric nanogenerators for flexible/stretchable and wearable electronics and artificial intelligence, Advanced Materials 32(5) (2020) 1902549.

[136] K. Dong, Z.L. Wang, Self-charging power textiles integrating energy harvesting triboelectric nanogenerators with energy storage batteries/supercapacitors, Journal of Semiconductors 42(10) (2021) 101601.

[137] X. Chen, Z. Ren, M. Han, J. Wan, H. Zhang, Hybrid energy cells based on triboelectric nanogenerator: from principle to system, Nano Energy 75 (2020) 104980.

[138] G. Zhu, B. Peng, J. Chen, Q. Jing, Z.L. Wang, Triboelectric nanogenerators as a new energy technology: from fundamentals, devices, to applications, Nano Energy 14 (2015) 126-138.

[139] K. Dong, Y. Hu, J. Yang, S.-W. Kim, W. Hu, Z.L. Wang, Smart textile triboelectric nanogenerators: Current status and perspectives, MRS Bulletin (2021) 1-10.

[140] K. Dong, X. Peng, J. An, A.C. Wang, J. Luo, B. Sun, J. Wang, Z.L. Wang, Shape adaptable and highly resilient 3D braided triboelectric nanogenerators as e-textiles for power and sensing, Nature communications 11(1) (2020) 1-11.

[141] J. Ahn, Z.-J. Zhao, J. Choi, Y. Jeong, S. Hwang, J. Ko, J. Gu, S. Jeon, J. Park, M. Kang, Morphology-controllable wrinkled hierarchical structure and its application to superhydrophobic triboelectric nanogenerator, Nano Energy 85 (2021) 105978.

[142] J. Xiong, H. Luo, D. Gao, X. Zhou, P. Cui, G. Thangavel, K. Parida, P.S. Lee, Self-restoring, waterproof, tunable microstructural shape memory triboelectric nanogenerator for self-powered water temperature sensor, Nano Energy 61 (2019) 584-593.

[143] L. Zhao, Q. Zheng, H. Ouyang, H. Li, L. Yan, B. Shi, Z. Li, A size-unlimited surface microstructure modification method for achieving high performance triboelectric nanogenerator, Nano Energy 28 (2016) 172-178.

[144] D. Bao, Z. Wen, J. Shi, L. Xie, H. Jiang, J. Jiang, Y. Yang, W. Liao, X. Sun, An anti-freezing hydrogel based stretchable triboelectric nanogenerator for biomechanical energy harvesting at sub-zero temperature, Journal of Materials Chemistry A 8(27) (2020) 13787-13794.

[145] A. Khan, S. Ginnaram, C.-H. Wu, H.-W. Lu, Y.-F. Pu, J.I. Wu, D. Gupta, Y.-C. Lai, H.-C. Lin, Fully self-healable, highly stretchable, and anti-freezing supramolecular gels for energy-harvesting triboelectric nanogenerator and self-powered wearable electronics, Nano Energy (2021) 106525.

[146] T.-S. Wong, S.H. Kang, S.K. Tang, E.J. Smythe, B.D. Hatton, A. Grinthal, J. Aizenberg, Bioinspired self-repairing slippery surfaces with pressure-stable omniphobicity, Nature 477(7365) (2011) 443-447.

[147] Q. Rao, Y. Lu, L. Song, Y. Hou, X. Zhan, Q. Zhang, Highly Efficient Self-Repairing Slippery Liquid-Infused Surface with Promising Anti-Icing and Anti-Fouling Performance, ACS Applied Materials & Interfaces (2021).

[148] B. Liu, K. Zhang, C. Tao, Y. Zhao, X. Li, K. Zhu, X. Yuan, Strategies for anti-icing: low surface energy or liquid-infused?, RSC advances 6(74) (2016) 70251-70260.

[149] Y. Wang, H. Zhang, X. Liu, Z. Zhou, Slippery liquid-infused substrates: a versatile preparation, unique anti-wetting and drag-reduction effect on water, Journal of Materials Chemistry A 4(7) (2016) 2524-2529.

[150] J. Chung, H. Cho, H. Yong, D. Heo, Y.S. Rim, S. Lee, Versatile surface for solid–solid/liquid–solid triboelectric nanogenerator based on fluorocarbon liquid infused surfaces, Science and technology of advanced materials 21(1) (2020) 139-146.

[151] W. Xu, X. Zhou, C. Hao, H. Zheng, Y. Liu, X. Yan, Z. Yang, M. Leung, X.C. Zeng, R.X. Xu, SLIPS-TENG: robust triboelectric nanogenerator with optical and charge transparency using a slippery interface, National Science Review 6(3) (2019) 540-550.

[152] W. Xu, H. Zheng, Y. Liu, X. Zhou, C. Zhang, Y. Song, X. Deng, M. Leung, Z. Yang, R.X. Xu, A droplet-based electricity generator with high instantaneous power density, Nature 578(7795) (2020) 392-396.

[153] J.D. Smith, R. Dhiman, S. Anand, E. Reza-Garduno, R.E. Cohen, G.H. McKinley, K.K. Varanasi, Droplet mobility on lubricant-impregnated surfaces, Soft Matter 9(6) (2013) 1772-1780.

[154] S. Peppou-Chapman, C. Neto, Mapping depletion of lubricant films on antibiofouling wrinkled slippery surfaces, ACS applied materials & interfaces 10(39) (2018) 33669-33677.

[155] P. Kim, T.-S. Wong, J. Alvarenga, M.J. Kreder, W.E. Adorno-Martinez, J. Aizenberg, Liquid-infused nanostructured surfaces with extreme anti-ice and anti-frost performance, ACS nano 6(8) (2012) 6569-6577.

[156] Z. Tang, S.Q. Lin, Z.L. Wang, Quantifying Contact-Electrification Induced Charge Transfer on a Liquid Droplet after Contacting with a Liquid or Solid, Advanced Materials. https://doi.org/10.1002/adma.202102886.

[157] Z. Tang, S. Lin, Z.L. Wang, Quantifying Contact-Electrification Induced Charge Transfer on a Liquid Droplet after Contacting with a Liquid or Solid, Advanced Materials 33(42) (2021) 2102886.

[158] C. Shi, B. Yan, L. Xie, L. Zhang, J. Wang, A. Takahara, H. Zeng, Long-range hydrophilic attraction between water and polyelectrolyte surfaces in oil, Angewandte Chemie International Edition 55(48) (2016) 15017-15021.

[159] X. Han, W. Li, H. Zhao, J. Li, X. Tang, L. Wang, Slippery damper of an overlay for arresting and manipulating droplets on nonwetting surfaces, Nature communications 12(1) (2021) 1-9.

[160] D. Daniel, J.V. Timonen, R. Li, S.J. Velling, J. Aizenberg, Oleoplaning droplets on lubricated surfaces, Nature Physics 13(10) (2017) 1020-1025.

[161] C. Vega-Sánchez, S. Peppou-Chapman, L. Zhu, C. Neto, Nanobubbles explain the large slip observed on lubricant-infused surfaces, Nature Communications 13(1) (2022) 1-11.

[162] M.S. Sadullah, C. Semprebon, H. Kusumaatmaja, Drop Dynamics on Liquid-Infused Surfaces: The Role of the Lubricant Ridge, Langmuir 34(27) (2018) 8112-8118. https://doi.org/10.1021/acs.langmuir.8b01660.

[163] M. Liu, Y. Hou, J. Li, L. Tie, Z. Guo, Transparent slippery liquid-infused nanoparticulate coatings, Chemical Engineering Journal 337 (2018) 462-470.

[164] C. Wei, G. Zhang, Q. Zhang, X. Zhan, F. Chen, Silicone oil-infused slippery surfaces based on sol–gel process-induced nanocomposite coatings: a facile approach to highly stable bioinspired surface for biofouling resistance, ACS applied materials & interfaces 8(50) (2016) 34810-34819.

[165] Y. Chen, Z. Guo, An ionic liquid-infused slippery surface for temperature stability, shear resistance and corrosion resistance, Journal of Materials Chemistry A 8(45) (2020) 24075-24085.

[166] P. Wang, D. Zhang, S. Sun, T. Li, Y. Sun, Fabrication of slippery lubricant-infused porous surface with high underwater transparency for the control of marine biofouling, ACS applied materials & interfaces 9(1) (2017) 972-982.

[167] I. Sotiri, A. Tajik, Y. Lai, C.T. Zhang, Y. Kovalenko, C.R. Nemr, H. Ledoux, J. Alvarenga, E. Johnson, H.S. Patanwala, Tunability of liquid-infused silicone materials for biointerfaces, Biointerphases 13(6) (2018) 06D401.

[168] J.S. Wexler, I. Jacobi, H.A. Stone, Shear-driven failure of liquid-infused surfaces, Physical review letters 114(16) (2015) 168301.

[169] Y. Hu, X. Wang, H. Li, H. Li, Z. Li, Effect of humidity on tribological properties and electrification performance of sliding-mode triboelectric nanogenerator, Nano Energy 71 (2020) 104640.

[170] Q. Zhou, K. Lee, K.N. Kim, J.G. Park, J. Pan, J. Bae, J.M. Baik, T. Kim, High humidity-and contamination-resistant triboelectric nanogenerator with superhydrophobic interface, Nano Energy 57 (2019) 903-910.

[171] S. Lin, L. Xu, A. Chi Wang, Z.L. Wang, Quantifying electron-transfer in liquid-solid contact electrification and the formation of electric double-layer, Nature Communications 11(1) (2020). https://doi.org/10.1038/s41467-019-14278-9.

[172] J. Nie, Z. Ren, L. Xu, S. Lin, F. Zhan, X. Chen, Z.L. Wang, Probing Contact-Electrification-Induced Electron and Ion Transfers at a Liquid-Solid Interface, Advanced Materials 32(2) (2020). https://doi.org/10.1002/adma.201905696.

[173] X. Hu, E. Pambou, H. Gong, M. Liao, P. Hollowell, H. Liu, W. Wang, C. Bawn, J. Cooper, M. Campana, K. Ma, P. Li, J.R.P. Webster, F. Padia, G. Bell, J.R. Lu, How does substrate hydrophobicity affect the morphological features of reconstituted wax films and

their interactions with nonionic surfactant and pesticide?, Journal of Colloid and Interface Science 575 (2020) 245-253. https://doi.org/10.1016/j.jcis.2020.04.043.

[174] M.A. Ghattas, S. Al Rawashdeh, N. Atatreh, R.A. Bryce, How Do Small Molecule Aggregates Inhibit Enzyme Activity? A Molecular Dynamics Study, Journal of Chemical Information and Modeling 60(8) (2020) 3901-3909. https://doi.org/10.1021/acs.jcim.0c00540.

[175] M. Khademi, S.S.Y. Cheng, D.P.J. Barz, Charge and Electrical Double Layer Formation in a Nonpolar Solvent Using a Nonionic Surfactant, Langmuir 36(19) (2020) 5156-5164. https://doi.org/10.1021/acs.langmuir.0c00311.

[176] H.F. Eicke, Surfactants in nonpolar solvents. Aggregation and micellization, Topics in current chemistry 87 (1980) 85-145.

[177] P. Alexandridis, K. Andersson, Reverse micelle formation and water solubilization by polyoxyalkylene block copolymers in organic solvent, Journal of Physical Chemistry B 101(41) (1997) 8103-8111. https://doi.org/10.1021/jp971197t.

[178] B.S. Ponto, J.C. Berg, Nanoparticle charging with mixed reverse micelles in apolar media, Colloids and Surfaces a-Physicochemical and Engineering Aspects 586 (2020). https://doi.org/10.1016/j.colsurfa.2019.124275.

[179] S. Poovarodom, S. Poovarodom, J.C. Berg, Effect of alkyl functionalization on charging of colloidal silica in apolar media, Journal of Colloid and Interface Science 351(2) (2010) 415-420. https://doi.org/10.1016/j.jcis.2010.07.058.

[180] M.N. Patel, P.G. Smith, Jr., J. Kim, T.E. Milner, K.P. Johnston, Electrophoretic mobility of concentrated carbon black dispersions in a low-permittivity solvent by optical coherence tomography, Journal of Colloid and Interface Science 345(2) (2010) 194-199. https://doi.org/10.1016/j.jcis.2010.01.055.

[181] P.G. Smith, Jr., M.N. Patel, J. Kim, T.E. Milner, K.P. Johnston, Effect of surface hydrophilicity on charging mechanism of colloids in low-permittivity solvents, Journal of Physical Chemistry C 111(2) (2007) 840-848. https://doi.org/10.1021/jp064573v.

[182] M. Gacek, G. Brooks, J.C. Berg, Characterization of Mineral Oxide Charging in Apolar Media, Langmuir 28(5) (2012) 3032-3036. https://doi.org/10.1021/la204000t.

[183] P. Li, T. Li, M. Ishiguro, Y. Su, Comparison of Same Carbon Chain Length Cationic and Anionic Surfactant Adsorption on Silica, Colloids and Interfaces 4(3) (2020). https://doi.org/10.3390/colloids4030034.

[184] S. Das, A. Katiyar, N. Rohilla, N. Quoc, R.T. Bonnecaze, Universal scaling of adsorption of nonionic surfactants on carbonates using cloud point temperatures, Journal of Colloid and Interface Science 577 (2020) 431-440. https://doi.org/10.1016/j.jcis.2020.05.063.

[185] V.B. Fainerman, E.V. Aksenenko, V.I. Kovalchuk, N. Mucic, A. Javadi, L. Liggieri, F. Ravera, G. Loglio, A.V. Makievski, E. Schneck, R. Miller, New view of the adsorption of surfactants at water/alkane interfaces - Competitive and cooperative effects of surfactant and alkane molecules, Advances in Colloid and Interface Science 279 (2020). https://doi.org/10.1016/j.cis.2020.102143.

[186] A.J. Simnick, C.A. Valencia, R. Liu, A. Chilkoti, Morphing Low-Affinity Ligands into High-Avidity Nanoparticles by Thermally Triggered Self-Assembly of a Genetically Encoded Polymer, Acs Nano 4(4) (2010) 2217-2227. https://doi.org/10.1021/nn901732h.

[187] M. Obersriebnig, J. Konnerth, W. Gindl-Altmutter, Evaluating fundamental position-dependent differences in wood cell wall adhesion using nanoindentation, International Journal of Adhesion and Adhesives 40 (2013) 129-134. https://doi.org/10.1016/j.ijadhadh.2012.08.011.

[188] H. Acharya, S. Vembanur, S.N. Jamadagni, S. Garde, Mapping hydrophobicity at the nanoscale: Applications to heterogeneous surfaces and proteins, Faraday Discussions 146 (2010) 353-365. https://doi.org/10.1039/b927019a.

[189] P. Yatsyshin, A.O. Parry, C. Rascon, S. Kalliadasis, Classical density functional study of wetting transitions on nanopatterned surfaces, Journal of Physics-Condensed Matter 29(9) (2017). https://doi.org/10.1088/1361-648X/aa4fd7.

[190] L. Sirghi, M. Nakamura, Y. Hatanaka, O. Takai, Atomic force microscopy study of the hydrophilicity of TiO2 thin films obtained by radio frequency magnetron sputtering and plasma enhanced chemical vapor depositions, Langmuir 17(26) (2001) 8199-8203. https://doi.org/10.1021/la010916z.

[191] H. Vatanparast, M. Eftekhari, A. Javadi, R. Miller, A. Bahramian, Influence of hydrophilic silica nanoparticles on the adsorption layer properties of non-ionic surfactants at water/heptane interface, Journal of Colloid and Interface Science 545 (2019) 242-250. https://doi.org/10.1016/j.jcis.2019.03.047.

[192] Q. Guo, J. Lee, V. Singh, S.H. Behrens, Surfactant mediated charging of polymer particles in a nonpolar liquid, Journal of Colloid and Interface Science 392 (2013) 83-89. https://doi.org/10.1016/j.jcis.2012.09.070.

[193] J. Schneider, Self-assembly of biomimetic surfactants and peptide amphiphiles in nonpolar solvents, Abstracts of Papers of the American Chemical Society 257 (2019).

[194] C.J. van Oss, Long-range and short-range mechanisms of hydrophobic attraction and hydrophilic repulsion in specific and aspecific interactions, Journal of Molecular Recognition 16(4) (2003) 177-190. https://doi.org/10.1002/jmr.618.

[195] P. Somasundaran, X. Yu, S. Krishnakumar, Role of conformation and orientation of surfactants and polymers in controlling flocculation and dispersion of aqueous and non-aqueous suspensions, Colloids and Surfaces a-Physicochemical and Engineering Aspects 133(1-2) (1998) 125-133. https://doi.org/10.1016/s0927-7757(97)00128-3.

[196] G.S. Roberts, R. Sanchez, R. Kemp, T. Wood, P. Bartlett, Electrostatic charging of nonpolar colloids by reverse micelles, Langmuir 24(13) (2008) 6530-6541. https://doi.org/10.1021/la703908n.

[197] C.E. Espinosa, Q. Guo, V. Singh, S.H. Behrens, Particle Charging and Charge Screening in Nonpolar Dispersions with Nonionic Surfactants, Langmuir 26(22) (2010) 16941-16948. https://doi.org/10.1021/la1033965.

[198] J. Lee, Z.-L. Zhou, S.H. Behrens, Interfaces Charged by a Nonionic Surfactant, Journal of Physical Chemistry B 122(22) (2018) 6101-6106. https://doi.org/10.1021/acs.jpcb.8b02853.

[199] C. Schreuer, S. Vandewiele, F. Strubbe, K. Neyts, F. Beunis, Electric field induced charging of colloidal particles in a nonpolar liquid, Journal of Colloid and Interface Science 515 (2018) 248-254. https://doi.org/10.1016/j.jcis.2018.01.040.

[200] M.M. Ramos-Tejada, F.J. Arroyo, A.V. Delgado, Negative Electrorheological Behavior in Suspensions of Inorganic Particles, Langmuir 26(22) (2010) 16833-16840. https://doi.org/10.1021/la1029036.

[201] T. Hao, Exploring the charging mechanisms in non-aqueous multiphase surfactant solutions, emulsions and colloidal systems via conductivity behaviors predicted with eyring's rate process theory, Physical Chemistry Chemical Physics 18(1) (2016) 476-491. https://doi.org/10.1039/c5cp05026j.

Appendix A: MATLAB code for force curves extraction in the force mapping

Detailed steps of this method

Step 1: In the AFM software, open the Master Force Panel, and then select the folder containing the force curve to be exported.

Step 2: Drag the above program into the AFM software, the software will automatically open this file.

Step 3: Click “Compile” at the bottom of the program window to compile. Do not turn it off during the period.

Step 4: After compiling, the software will add a new menu called "SV", there are three options in the menu, select the data you need.

Step 5: For example, we click on the first option “Export Force Curves”. A window will appear at this time, we need to specify the path to save the txt file. You can click browse to change the path, and then click OK to start exporting the data.

Program details are given below

```
#pragma rtGlobals=1		// Use modern global access method.

 menu "SV"

 "Export Force Curves", ExportForceSV(0)

 "Export Force Curves Extend only", ExportForceSV(1)
```

```
"Export Force Curves Retract only", ExportForceSV(2)

  end

 function ExportForceSV(which)

 variable which

 String SavedDataFolder = GetDataFolder(1)

 SetDataFolder "root:ForceCurves:Parameters"

 KillPath/Z ForceSavePath

 NewPath/O/Q/Z/C/M="Select path to save force curves" ForceSavePath

 string LUList = WaveList ("*LookUpTable", ";", "DIMS:1”)

 string nameStr="", folderName="", fName=""

 String whichStr = StringFromList (which,”; Ext;Ret")

 variable i, j, k, maxLVDTloc, start, stop    // second loop to export all force curves

 string DeflName, RawName, numStr, noteStr

 variable number, count, len, SpringConstant, invOLS, refNum

 for (i=0; i<ItemsInList (LUList); i+=1)          // loop over all basenames

 wave/T wLU = $StringFromList(i,LUlist)

 count = 0                                         // counts all curves with this basename

 for (j=0; j<DimSize(wLU,0); j+=1)                 // loop over all curves with this basename

  nameStr = GetDimLabel (wLU,0, j)                          // name of wave with raw LVDT data

 folderName = wLU[j]

 wave/Z Defl = $(folderName+nameStr+"Defl")          // reference to Deflection wave

wave/Z Raw = $(folderName+nameStr+"Raw")          // reference to LVDT wave
```

```
if (! waveexists (Defl) ||! waveexists (Raw))               // check if Deflection wave exists
print "Error in ExportForce: missing wave: "+nameStr+ " (Raw or Defl)"
continue
End if
noteStr = note (Raw)          // get the wave note
invOLS = NumberByKey ("invOLS", noteStr, ":", "\r”)              // read invOLS from note string
SpringConstant = NumberByKey("SpringConstant", noteStr , ":", "\r" )    // read spring constant from note string
wavestats/Q/M=1 Raw
maxLVDTloc = x2pnt (Raw, V_maxloc) // point of max LVDT extension, separates extend and retract
fName = nameofwave (Raw) [0, strlen (nameofwave (Raw))-4] +whichStr+".txt"
Open /P=ForceSavePath/T=".txt" /Z=2 refNum as fName
if (V_flag==-1)
print "Error in opening “, fName
return 0
endif
start = which! = 2? 0: maxLVDTloc    // if only retract, start exporting from max LVDT location
stop = which! = 1? DimSize (Raw,0): maxLVDTloc+1
// if only extend, stop exporting at max LVDT location
//-------------------- MODIFY HERE IN TWO PLACES TO SELECT DEFL, DEFLVOLTS OR FORCE --------------------------------------
// fprintf refNum, " time/s          LVDT/m          Defl/m"
```

```
// use this for Deflection in m

// fprintf refNum, " time/s          LVDT/m          Defl/V"

// use this for Deflection in V

fprintf refNum, " time/s          LVDT/m          Force/N"   // use this for Force in N

for (k=start; k<stop; k+=1)  // fprintf refNum, "\r\n %e    %e    %e", pnt2x (Raw, k), Raw[k], Defl[k]
// Raw LVDT and Defl

// fprintf refNum, "\r\n %e    %e    %e", pnt2x (Raw, k), Raw[k], Defl[k]/invOLS

// Raw LVDT and DeflVolts fprintf refNum, "\r\n %e    %e    %e", pnt2x (Raw, k), Raw[k],
Defl[k]*SpringConstant                      // Raw LVDT and Force

                              endfor

//----------------------------- END OF SECTION TO MODIFY -------------------------------------------------
-------------------

Close refNum

count += 1

end for

print "Exported “, count," force curves with basename “, nameofwave (Raw) [0, strlen(nameofwave
(Raw))-8]

DoWindow/H

End for

Set Data Folder Saved Data Folder

return 0

End
```

Appendix B: MATLAB code for dynamic diameter analysis of the water droplet during spreading-rebounding process

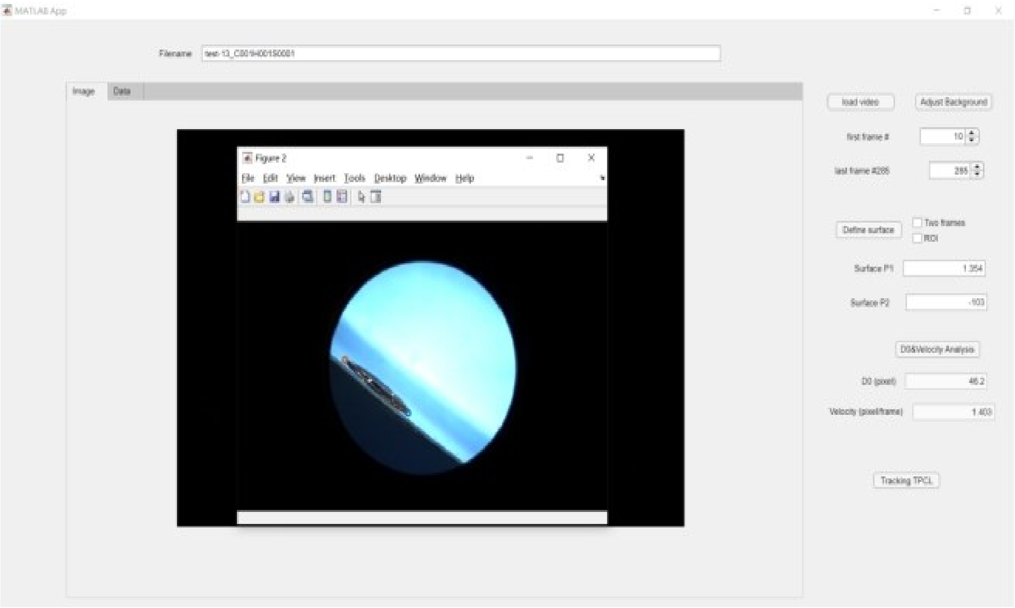

Filename test-13_C001H001S0001

first frame # 10

last frame #285 285

☐ Two frames

☐ ROI

Surface P1 1.354

Surface P2 -103

D0 (pixel) 46.2

Velocity (pixel/frame) 1.403

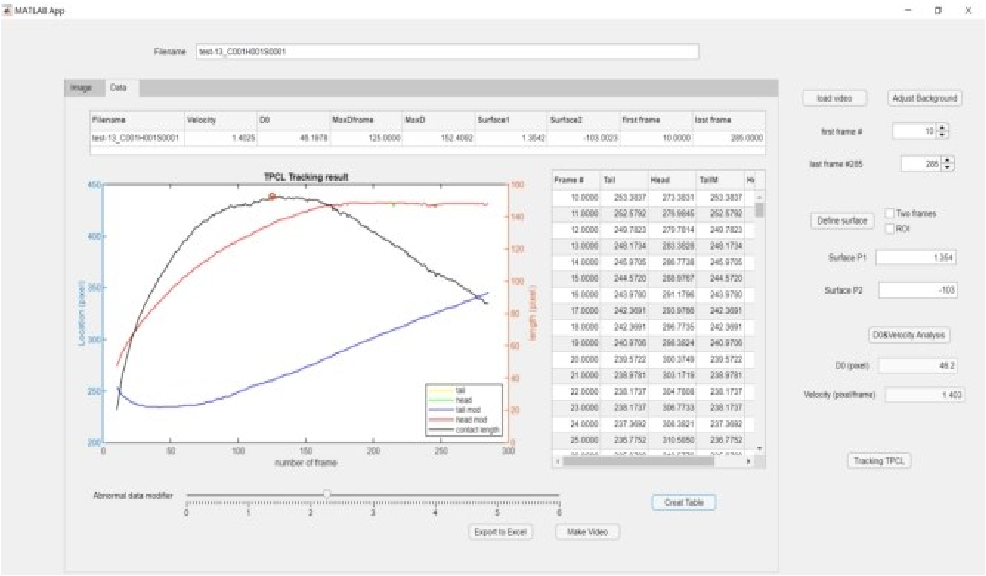

Filename test-13_C001H001S0001

Filename	Velocity	D0	MaxDframe	MaxD	Surface1	Surface2	First frame	last frame
test-13_C001H001S0001	1.4025	46.1678	125.0000	152.4092	1.3542	-103.0023	10.0000	285.0000

Frame #	Tail	Head	TailM	He
10.0000	253.3837	273.3831	253.3837	
11.0000	252.5792	276.9845	252.5792	
12.0000	249.7823	279.7814	249.7823	
13.0000	248.1734	283.3828	248.1734	
14.0000	245.9705	286.7738	245.9705	
15.0000	244.5720	288.9767	244.5720	
16.0000	243.9780	291.1796	243.9780	
17.0000	242.3691	293.9788	242.3691	
18.0000	242.3691	296.7735	242.3691	
19.0000	240.9706	298.3824	240.9706	
20.0000	239.5722	300.3749	239.5722	
21.0000	238.9781	303.1719	238.9781	
22.0000	238.1737	304.7808	238.1737	
23.0000	238.1737	306.7733	238.1737	
24.0000	237.3692	308.3821	237.3692	
25.0000	236.7752	310.5860	236.7752	

☐ Two frames

☐ ROI

first frame # 10

last frame #285 285

Surface P1 1.354

Surface P2 -103

D0 (pixel) 46.2

Velocity (pixel/frame) 1.403

```
%%

%------------------------------------------------------------------------

%                    1.       Reading Video

%------------------------------------------------------------------------

Clear;

clc;

[filename,pathname]=uigetfile('*.*','Please select the video you want to read');

if filename

   vidObj=VideoReader(strcat(pathname,filename));

end

mov= {}.

k=0;

while hasFrame(vidObj)

   frame= readFrame(vidObj);

   k=k+1;

   mov{k}=frame(:,:,:);

end

clear k frame vidObj

%%

%------------------------------------------------------------------------

%           2.       Manual pre-processing

%------------------------------------------------------------------------
```

```
deg=36; % parameter 1
x0=242; % parameter 2
I=mov {80}; % # of frame for check

I0=imrotate(I,deg,'bilinear','crop');
imshow(I0,'InitialMagnification','fit','Border','tight');
hold on
plot ([1, size(I0,2)],[x0,x0],'LineWidth',1,'Color','red');
clear I0 I
%%
%-----------------------------------------------------------------------
%       3.      Determine first frame #
%-----------------------------------------------------------------------
close
N0=10;          % # of first frame for processing
I=mov{N0};
imshow(I,'InitialMagnification','fit','Border','tight');
% clear I
%%
%-----------------------------------------------------------------------
%       4.      Data processing
%-----------------------------------------------------------------------
```

```
threshold=20; % Adjustable parameter (noise intensity), typically >10


I=mov {1};

I0=imrotate(I,deg,'bilinear','crop');

Ig=rgb2gray(I0);

Ig=double (Ig);

st=Ig (x0,:);

CL=zeros(length(mov)-N0+1,2);

for N=N0: length(mov)

   I=mov{N};

   I0=imrotate(I,deg,'bilinear','crop');

   Ig=rgb2gray(I0);

   Ig=double (Ig);

   DI=abs (Ig(x0,:)-st);

   if max (DI)>=threshold

      k=1;

      while DI(k)<threshold

         k=k+1;

      end

      CL(N-N0+1,1) =k;

      k=length (DI);

      while DI(k)<threshold
```

```
            k=k-1;
        end
        CL(N-N0+1,2) =k;
    end
end
if min (CL)==0
CL (find(CL==0):end,:)=[];
end
clear k I I0 Ig st N DI
%%
%------------------------------------------------------------------------
%           5.      Visual Checking
%------------------------------------------------------------------------
Video_save=1; % Set this variable to 1 if you intend to create a video
close
if Video_save==1
    filenamenew=[filename(1: end-4),'M',filename(end-3:end)];
    v = VideoWriter([pathname,filenamenew]);
    open(v);
end
for N=N0:(length (CL)+N0-1)
    I=mov{N};
```

```
    I0=imrotate(I,deg,'bilinear','crop');

    imshow(I0,'Border','tight');

    hold on

    plot (CL(N-N0+1,1), x0,'o','Color','red','LineWidth',2);

    plot (CL(N-N0+1,2), x0,'o','Color','magenta','LineWidth',2);

    hold off

    frame = getframe(gcf);

    if Video_save==1

        writeVideo(v,frame);

    end

end

close

if Video_save==1

    close(v);

end

plot (CL(:,1))

hold on

plot (CL(:,2))

clear I I0 frame Video_save filenamenew
```

Appendix C: Modulation of surface charge by mediating surface chemical structures in nonpolar solvents with nonionic surfactant used as charge additives

C.1 Introduction

Surface charging mechanisms in non-polar media is far from being well understood even though they are important for many practical applications, such as the development of electrophoretic displays[85] and tribo-electricity nanogenerators[171, 172], stabilization of pesticide products[173], as well as measurements of enzyme activity.[174]

Theoretically, charges are more difficult to stabilize in non-polar solvents. The inclusion of a charge in a non-polar medium has a much longer range effect on any other charges present than that in an aqueous medium. This is captured by the Bjerrum length (λ_B), which is defined as the distance between two charges where the Coulombic energy is equal to the thermal energy (k_BT). In this expression, e is the elementary charge, and ε_0 is the permittivity of free space. [90]

$$\lambda_B = \frac{e^2}{4\pi\varepsilon_0\varepsilon_r k_B T} \qquad \text{(C-1)}$$

As an example, the Bjerrum length for two charge points is 0.71 nm in water at room temperature (T = 23 °C), which means the thermal energy can overcome the electrostatic energy between the ion and the charged surface that are separated more than 0.71 nm apart. In non-polar solvent, the Bjerrum length is about 28 nm, giving a typical ε_r value of 2.0.

Therefore, the surface charging in non-polar solvents cannot be achieved through ion dissociation or ion adsorption. However, it is still possible to generate and stabilize charged ions in non-polar solvents by a variety of methods, such as surfactants induced charging of surfaces.[175, 176]

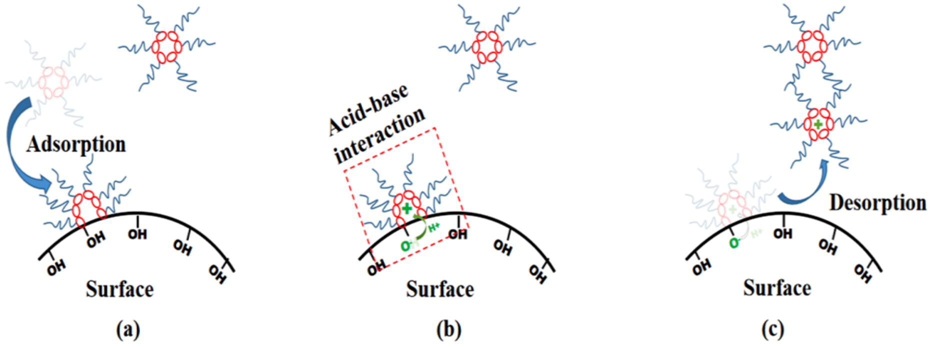

Figure C.1: Surface charging process. (a) The neutral reverse micelle is adsorbed onto the surface; (b) Charge is transferred between surface and reverse micelles; (c) Charged reverse micelles desorb from the surface and diffuse into non-polar solvent with nonionic surfactants used as charge control additive.

Surface can be charged in non-polar solvents if surfactants are used as charge control additives. In this process, the reverse micelles formed by the aggregation of surfactant molecules plays an important role in surface charging. In non-polar solvents, surfactants could form reverse micelle structures (also called inverted micelles) above their corresponding critical micellization concentration (CMC) due to solvophobic effect. It is worth mentioning that some authors specified the term “reverse CMC” for reverse micellization, since the nature of reverse micellization in non-polar solvents is different from the micellization in aqueous environment.[177] In this article, “CMC” and “reverse CMC” are used interchangeably. Recently, it has been confirmed that reverse micelles assist in surface charging in non-polar solvents, but the charging mechanism is still debatable. Morrison[92] summarized three possible charging mechanisms that can lead to the formation of charged colloidal species in non-polar media: (1) acid-base interactions between inverse micelles and particle surfaces, (2) dissolution of surface species into inverse micelles, and (3) preferential adsorption of charged inverse micelles onto particle surfaces. The adaptability of mechanism interpretations depends on the characteristics of each research system.

For surface charges in non-polar solvent induced by non-ionic surfactants, the mechanism of acid-base interaction is particularly applicable.[93] The acid-base interaction mechanism proposed that the surface obtains the charge through a three-step process, as illustrated in Fig. C.1a: the neutral reverse micelles are first adsorbed on the surface of the particles; Fig. C.1b: the charge is transferred from the surface to the reverse micelles; Fig. C.1c: finally, the now charged reverse micelles desorb from the surface, leaving an oppositely charged surface behind. The polarity and magnitude of the charge were suggested to depend on the relative acidity/basicity between the nonionic surfactants and the surface. By modifying both the surfactant and the particle, a relationship between relative aqueous acidity or basicity and the charge in non-polar systems has been determined. For example, Berg *et al.*[178] mixed an acidic surfactant (sorbitan monooleate, SPAN 80) with a basic surfactant (Chevron Oronite, OLOA 11000) with acidic and basic particles in isoparaffin, respectively. The basic particles were positively charged in the presence of the acidic surfactant, whereas the acidic particles were negatively charged in a solution with the basic surfactant. Poovarodom *et al.*[94] also indicated that the polarity and magnitude of the surface charge were strongly dependent on the acid-base properties of the surface and the surfactant in non-polar solvents. Some studies[179] have also speculated that the magnitude of surface charge may be proportional to the density of the acid-base reaction sites on the surface, but this hypothesis is still open to debate.

In some applications, charges need to be generated on surfaces with no potential acid-base interaction sites, *i.e.,* "afunctional" surface. According to the surface charge mechanism of acid-base interaction, these surfaces cannot be charged by nonionic surfactants although doubts continue to exist. One common method to charge afunctional surfaces in non-polar environment is by modifying them with inert alkyl groups, which produces hydrophobic surfaces and allows the adsorption of reverse micelles.[180] For example, Pooravodom *et al.*[179] found that the hydrophobicity of the surfaces was critical to the charging behavior of the particles in non-polar solvent with three surfactants (dioctyl sulfosuccinate sodium salt (AOT), OLOA 11000, and $ZrO(Oct)_2$). Smith *et al.*[181] suggested that particles in non-polar liquids could be charged by preferential adsorption of ionic surfactant, based on the surface hydrophobicity. Silica surfaces treated with cyano, amine, or hydroxyl surfaces have been observed to be charged, although the sign and magnitude of the charge depends on the surfactant and the surface functionalization groups and wettability.[182] From these treated surfaces, it is clear that the hydrophobicity of the surface plays an important role in determining the sign and magnitude of the charge. However, Fowkes *et al.*[182] found that surface charging features could be inconsistent for the same wettability carbon black, and they attributed this difference to the uneven surface chemistry of commercial hydrophobic particles. Their results raised the concern that it might not be appropriate to interpret the surface charging properties in non-polar solvents solely on macroscopic hydrophobicity, even though the hydrophobicity depends on the surface concentration of acid-base interaction site (such as hydroxyl group). Therefore, further studies are needed to investigate the factors that influence the surface charging behavior in non-polar solvents, such as surface chemical structure differences. For example, alkyl length of the surface groups, especially for self-assembled monolayer (SAMs) coated surfaces.

The alkyl length of surface groups has been demonstrated to affect the interfacial charging behavior in non-polar solvents, when non-ionic surfactants were used as charge control additives. According to the charging mechanism of the nonionic surfactant in the non-polar solvent shown in Fig. C.1, the surface charging properties are most likely related to the adsorption capacity of reverse micelles in non-polar solvents. According to the existing research results[183-185], it can be inferred that the alkyl length of surface groups may affect the adsorption behavior of reverse micelles on the surface. By coordinating different conditions, including the density of acid-base interaction sites and surfactant adsorption capacity on surfaces, the regulation of surface charge in non-polar solvents can be achieved with surfactants used as charge control additivities.

In this part, we revealed the mechanism of how surface chemical structures affect surface charging behavior in non-polar solvent, where nonionic surfactants were used as charge control additives. Surface chemical structures were tuned by the coating of a variety of SAMs, which manipulated the alkyl length and the concentration of acid-base interaction sites on the surface. After the characterization of SAMs-coated surfaces, the effects of surface chemical structure on the adsorption of nonionic surfactant and surface charging behavior in non-polar solvent was studied. By tuning the chemical structures of the surface, such as the surface hydroxyl site density and alkyl length, the surface charge strength could be further improved in non-polar solvents. This research could provide insights into the charging phenomenon in non-polar solvents and contribute toward more comprehensive understanding of the underlying mechanism. This study could also provide valuable guidance on developing effective charge control additives for industrial applications.

C.2 Materials and Experiments

Ethanethiol (C_2, ≥ 97%), 1-Hexanethiol (C_6, ≥ 99%), 1-undecanethiol (C_{11}, 98%), 2-Mercaptoethanol (C_2OH, ≥ 99%), 11-mercapto-1-undecanol ($C_{11}OH$, ≥ 99%); Tricholoro(ethyl)silane (TES-C_2, ≥ 98%), Tricholoro(hexyl)silane (THS-C_6, ≥ 99%), Tricholoro(dodecyl)silane (TDS-C_{11}, ≥ 98%) were purchased from Sigma-Aldrich. The nonionic surfactant, sorbitan monooleate (SPAN 80, Sigma, ≥ 99%), was used without further purification. The chemical constitution and chain structures of alkanethiols and chlorosilane are summarized below (Fig. C.2). Deionized water (18.2 MΩ·cm resistivity and surface tension of 72.5 mN/m at room temperature of 20 °C) and extra-dry heptane (Merck, purity ≥ 98%, water content < 0.0003 wt.%) were used as the two liquid phases. A series of surfactant-heptane solutions at the desired concentrations were prepared in the glove box and used immediately, to avoid the influence of moisture as much as possible. The CMC of SPAN 80 in the heptane was approximately 0.018 mM, (refer to Fig. C.3), which is similar to the reference value in the literature.[96]

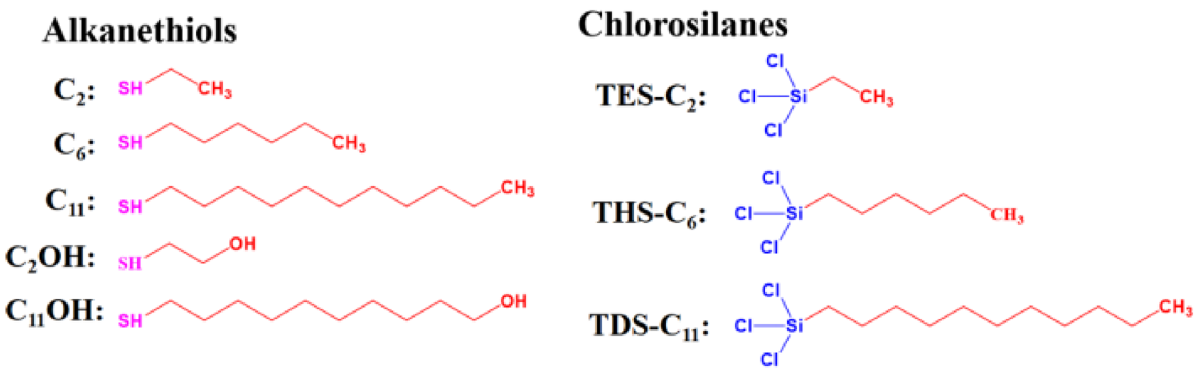

Figure C.2: Chemical structure of chemicals used in this research.

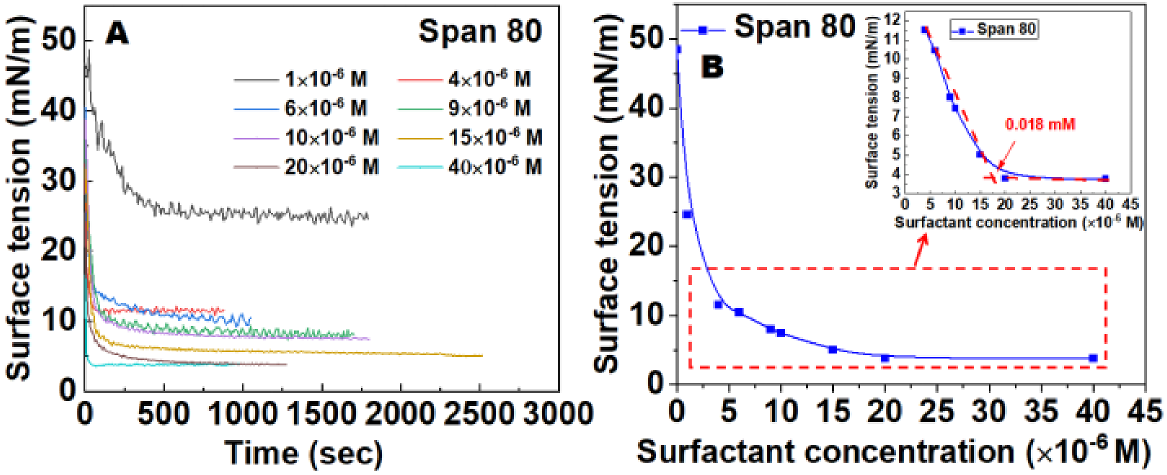

Figure C.3: CMC confirmation of SPAN 80 in extra-dry heptane: (A) dynamic surface tension changes with time under the condition of a fixed surfactant concentration; (B) surface tension changes with the concentration of SPAN 80; inset is a zoom-in of the concentration range of SPAN 80.

C.2.1 Preparation of self-assembled monolayer (SAM) with various surface compositions

Smooth gold sensors (QSX 301, Qsensor) were purchased from Boiolin Scientific (Sweden) with surface roughness less than 1 nm. Pre-cleaning the surface by UV/ozone for ten minutes was necessary to remove any possible contamination such as hydrocarbons and dust. Then, the SAMs coating surfaces were prepared by immersing the fresh gold sensor into methanol solutions containing 40 mM single-component thiols or binary-component thiols with different tail groups at specific molar ratios, as shown in Fig. C.4. Different SAMs coated solutions were prepared according to the proposed design in Table 3-3. This preparation process requires special attention to the following points: (1) use an extremely dry solvent (with a water content of less than 0.0003 wt.%) and remove impurities in advance; (2) use a special glass container and heating at high temperature (1000 °C) before use to reduce the water content as much as possible; (3) the whole process of preparing the SAMs coating solution is completed in the glove box to minimize the influence of atmospheric humidity; and (4) immersing the clean gold sensor in the SAMs coating solution and seal the container immediately, then transfer the container to a vacuum box. After being incubated for 24 h at room temperature, the surfaces were extensively rinsed with a large amount of methanol and thoroughly dried with nitrogen gas flow. After that, the nitrogen dried sample surfaces were immediately transferred into a vacuum desiccator for further use. Then, the hydroxyl concentration M_{OH} at the surface of different SAMs was calculated,

$$M_{OH} = \frac{c_{OH}}{c_S} \times 100\% \qquad \text{(C-2)}$$

where M_{OH} represents the concentration (or coverage) of OH-ended group in the whole SAMs layer, C_{OH} represents the concentration of OH-ended group (O1s signal peak area from XPS analysis), and C_S represents the concentration of both OH-ended and CH3-ended groups on the SAMs surface (S2p signal peak area from XPS analysis). For each SAM coated sensor, the wettability and surface coverage of hydroxyl group was confirmed by contact angle tests (static water contact angle in air on various solid surfaces), X-ray photoelectron spectroscopy (XPS) characterization and force mapping analysis.

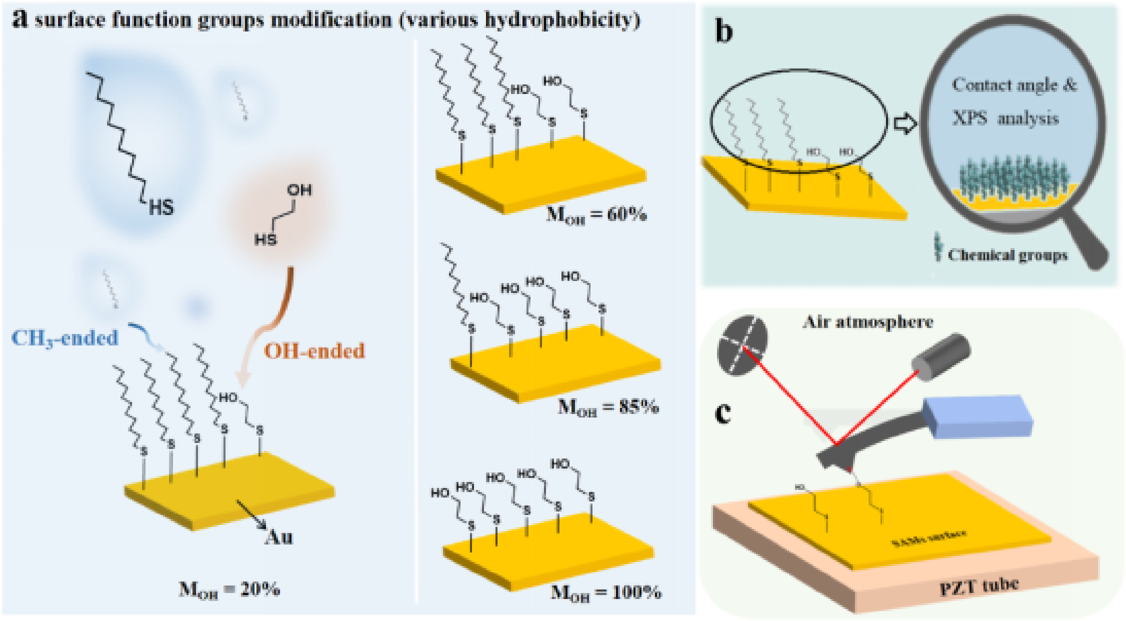

Figure C.4: Schematic illustration of the preparation of surfaces modified by various chemical functional group. (a) Mixing of the alkanethiols coupling agents and the self-assemblies of functional groups on the gold surfaces. (b) SAMs analysis of the modified gold surface by contact angle and XPS measurements. (c) Setup of the AFM platform for the force mapping experiments and measurements of the distribution of coated functional groups.

C.2.2 Adhesive force mapping by AFM

Adhesion force mapping was carried out using an untreated silicon tip mounted on a silicon nitride cantilever (Scanasyst-Air, Bruker, USA; cantilever stiffness 0.5 N/m) in commercial MFP-3D AFM system (Asylum Research, Santa Barbara, CA). More cantilever details are given in the Fig. 3.6. A sinusoidal driving voltage applied to the z-piezo is used to oscillate the cantilever position at frequencies ranging from 10 to 300 Hz. This led to intermittent contact between the probe tip on the cantilever and the sample surface. The frequency of z-piezo modulation was lower than the resonance frequency of the cantilever. For each force curve, the maximum deflection signal, read on the photodetector, is used to calculate the Z height measured by the Z sensor. Maximum force is calculated in real-time and is used as error signal for the Z feedback loop. While the probe position is driven (sinusoidal wave) in the Z-axis, the sample is moving underneath it in a raster pattern in the X-Y plane. One force distance curve could be obtained in one period of the z-piezo modulation. Desired signals, such as pull-off (adhesive force), and jump-in (attractive force) could be measured by using sample and hold circuit with suitable time windows. Deflection of the cantilever was monitored by the optical lever method[177]. The adhesive force mappings were performed in air (humidity, 44%) at room temperature (~ 23 °C). Brighter contrast in an adhesive force map corresponds to a higher adhesive force.

Table C. 1 Coating methods for specific SAMs surfaces (40 mM for all alkanethiols coating solutions).

Number	C_2OH	C_2CH_3	C_6CH_3	$C_{11}CH_3$	M_{OH}	θ_C
1	20 ml	-	-	-	100%	20°
2	16 ml	-	-	4 ml	85%	60°
3	10 ml	-	-	10 ml	60%	90°
4	2 ml	-	-	18 ml	20%	108°
5	10 ml	-	-	10 ml	60%	90°
6	10 ml	-	10 ml	-	60%	90°
7	10 ml	10 ml	-	-	60%	90°

D.2.3 Measurement of surfactants adsorption on the solid surface

The adsorption of surfactants at the solid-liquid interface was measured using a quartz crystal microbalance with dissipation (QCM-D). QCM-D monitors two characteristic parameters of resonant frequency (*f)* and dissipation factor (*D*). In our study, a Q-Sense Analyzer (Biolin Scientific, Sweden) was used to assess *f* and *D* of the piezoelectric sensor as a function of adsorption time. Different thiols coated gold sensors were used and the experiments were carried out at 20 °C in non-polar solvents throughout. The fluid was fed by a peristaltic pump at a volumetric flow rate of 0.1 mL/min. At the beginning of the experiments, stable baseline signals were established by flowing pure heptane. The surfactant solutions of desired concentrations were pumped through the cell while monitoring the change of *f* and *D* as a result of surfactant adsorption.

C.2.4 Electrophoresis measurements

The electrophoretic mobility in non-polar dispersions was measured by phase analysis light scattering (PALS) using a Zetasizer Nano ZS90 (Malvern Instruments). The system automatically converted the measured mobility into zeta potential ξ through the following equation.

$$\mu = \frac{\xi \varepsilon_r \varepsilon_0 f(\kappa a)}{\eta} \qquad \text{(C-3)}$$

where μ is the electrophoretic mobility, ξ is the zeta potential, κa is the reduced inverse Debye length, and η is the viscosity of the medium. In non-polar solutions where $\kappa a \gg 1$, $f(\kappa a)$ equals to 2/3 (Hückel limit). As for the detailed operation procedures of electrophoresis measurement are given below: a dip cell with two planar palladium electrodes spaced 2 mm apart was submerged in a sample dispersion (0.05 wt.%) held in a glass cuvette. An electric field of systematically varied strength (2.5-50 kV/m) was applied across the electrodes to obtain the field-dependent mobility based on time domain phase information on the light scattered by the particles. The field-dependent mobility was then extrapolated to zero field strength to infer the equilibrium charging state of the particles in the absence of the applied electric field. Prior to the measurements, the dip cell and glass cuvette were sonicated in tetrahydrofuran (THF, a good solvent for PIBS), carefully rubbed with a soft wipe in hot aqueous detergent solution, rinsed copiously, first with hot water and then with methanol, and dried with N_2.

C.3 Results and Discussion

C.3.1 Characterize the surface adsorption of SAMs

Surface charging in non-polar solvent could be achieved through acid-base interaction between the surface and adsorbed nonionic surfactant SPAN 80. It is reasonable to infer that the adsorption of surfactant on the solid surface plays an important role for surface charging in non-polar solvents. Therefore, in this section, we first characterized the factors that could influence on the surfactant adsorption. Effects of surface wettability and SAMs alkyl length on surfactant adsorption capacity and stability were explored in non-polar solvent by adjusting the surface chemistry and nanostructure.

The surface compositions of the prepared methyl (CH_3)/hydroxyl (OH)-ended SAMs were characterized by XPS in a vacuum chamber, and the results are shown in Fig. C.5. Binding energies referenced to C1s peak are located at 284.8 eV. Figs. D.5a-d display the sulfur signals for the four types of SAMs (various contact angle, θ_c), exhibiting characteristic doublet peaks at around 162 eV (2p3/2) and 163 eV (2p1/2). This could be assigned to the bonding of thiol to gold wafer. The red curves in Figs. D.5e-h denote the oxygen signals (O1s) for SAMs (C_2OH only or mixed $C_{11}CH_3/C_2OH$) surfaces with different surface coverage of -OH group respectively. The wide peaks at around 532 eV should be attributed to the overlapping of the signals from OH states. Thus, the average OH-ended group concentrations (M_{OH}) in the SAMs surface were calculated by Eq. (D-2). Based on the XPS characterization results, it can be inferred that the M_{OH} of these four binary-component SAMs surface were around 20%, 60%, 85% and 100%, respectively.[186]

After obtaining the average value of OH-ended group concentration, it is then necessary to determine the distribution of functional groups on the SAMs surface through AFM force mapping analysis. This is because XPS cannot be used to infer the uniformity of SAMs coating on the surface directly. The force mapping images of the four investigated surfaces are provided in Figs. D.5i-l. The tip (silicon) used in the present study shows distinctly higher adhesion forces to polar surfaces (e.g., -OH group) compared to nonpolar surfaces (e.g., -CH_3 group) [187] and is thus representative of attraction of polar molecules between surface and tip. As shown in Figs. D.5i-l, the gold surfaces coated by the OH-ended group were shown as the bright area, whereas the regions coated by CH_3-ended group exhibited dark color. That is to say, the bright color in a force mapping image reflects a strong adhesion force between the -OH group ended SAMs surface and the AFM tip (silicon). On the other hand, the black areas appeared if it is weak adhesion interaction between the -CH_3 group ended SAMs surface and the silicon tip.[188, 189] Since the pull-off force is proportional to the local adhesion energy, measured adhesion forces provide relative information about the degree of hydrophilicity of the surface.[190] Using image analysis software (Adobe Photoshop), M_{OH} concentration could be calculated from the ratio of the bright area in each image. The M_{OH} concentrations were approximately 20 ± 2.1%, 60 ± 1.8%, 85 ± 1.3% and ~ 100%, all of which are consistent with the results from XPS analysis. More importantly, force mapping images indicated that the adsorption of thiols molecules on the gold surface had a relatively uniform monolayer distribution. For M_{OH} ~100% SAMs surface, there were slight black spots in the force mapping image, which could be attributed to unavoidable contamination during the SAMs surface preparation. Therefore, it is reasonable to assume that the $\mathrm{M_{OH}}$ value of this type of surface is equal to 100%. On the other hand, the SAMs surface hydrophobicity was determined by the surface chemistry and nanostructures, the contact angle was expected to be lower with increasing concentration of the OH-ended group on the SAMs surface, as shown in Figs. D.5m-p.

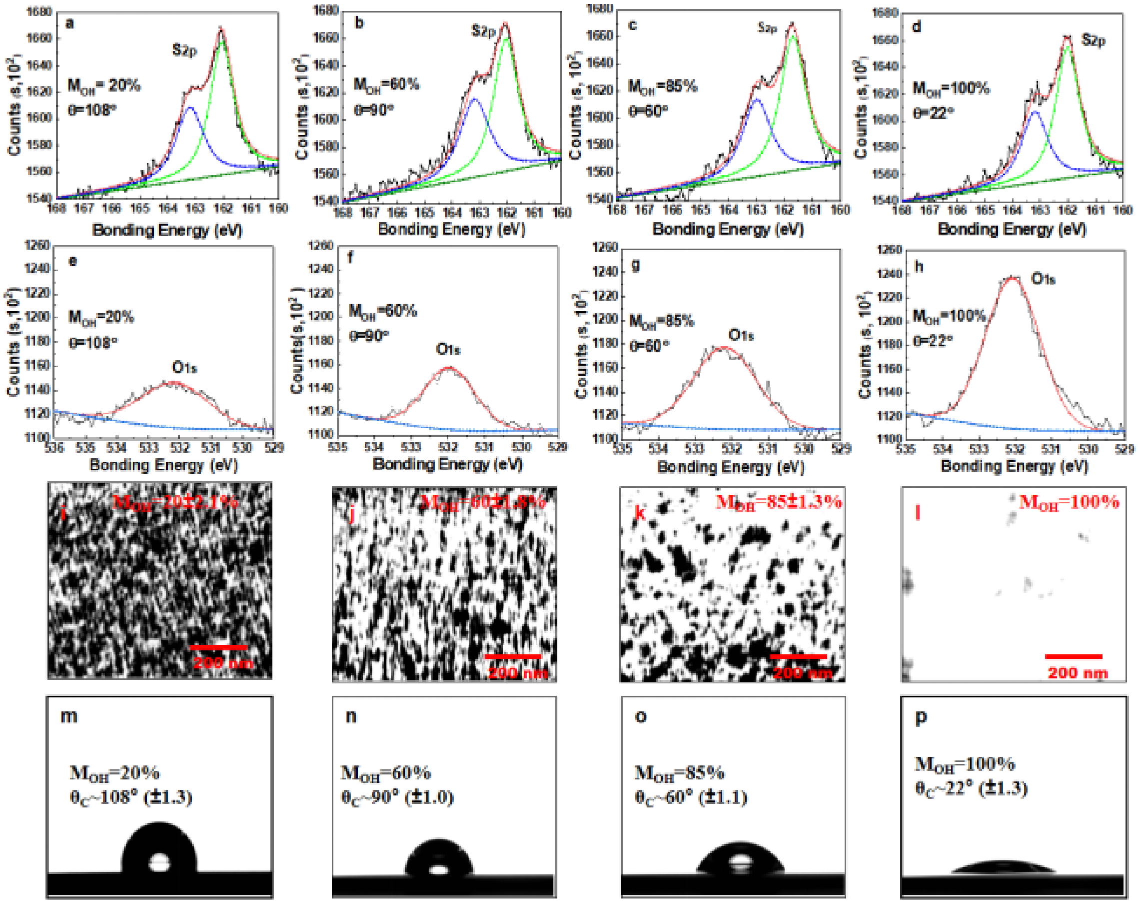

Figure C.5: Sulfur signals (a-d) and oxygen signals (e-h) for four types of SAMs, which could be assigned to the bounding of thiol to gold wafer and hydroxy group on the SAMs coated gold surfaces, respectively. (i-l) Distribution of OH-ended (bright area) and CH_3-ended (black area) thiols coated on gold surface through AFM force mapping measurements. (m-p) Images of static water contact angle (θc) in air on the prepared methyl/hydroxyl-ended SAMs($C_2OH/C_{11}CH_3$) with various molar ratio. The error values in the brackets show the standard deviations of ten independent measurements.

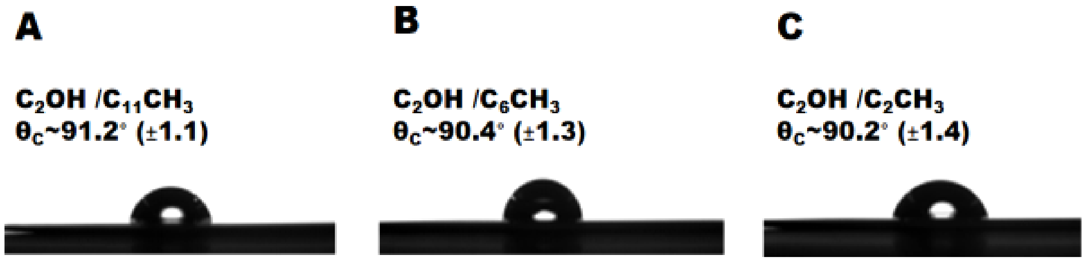

Figure C.6: Images of static water contact angle (θc) in air on the prepared methyl/hydroxyl-ended SAMs (A) $C_{11}CH_3/C_2OH$ (B) C_6CH_3/C_2OH and (C) C_2CH_3/ C_2OH. The error values in the brackets show the standard deviations of ten independent measurements.

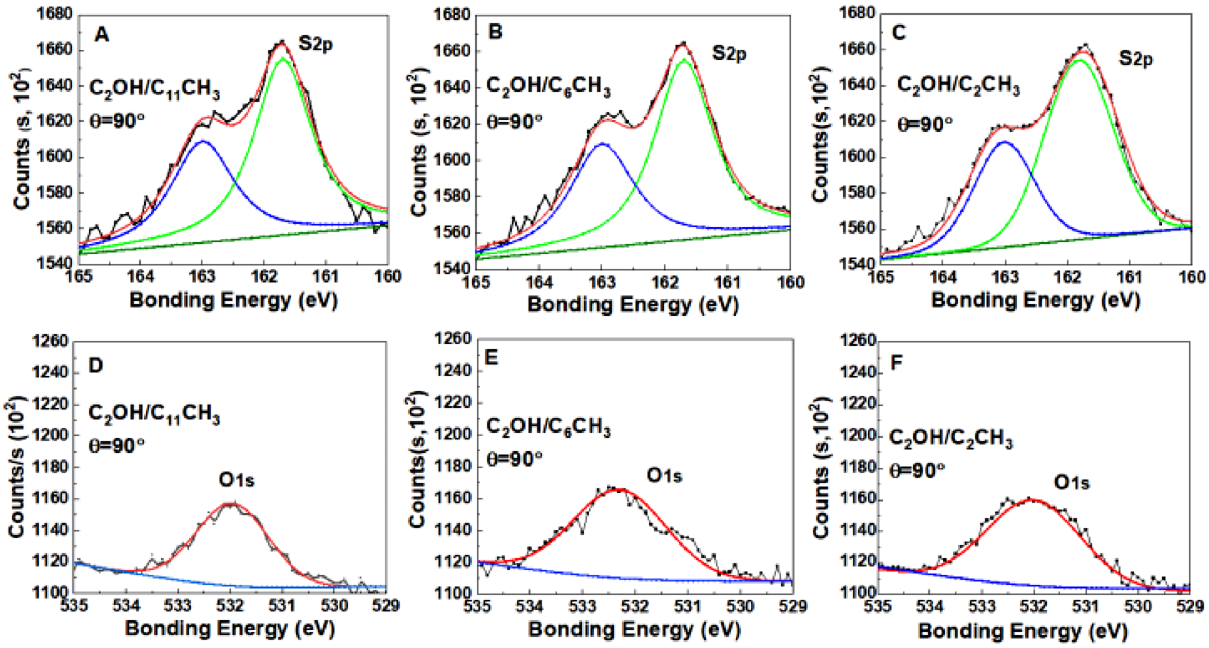

Figure C.7: Sulfur signals (A~C) and oxygen signals (D~F) for three types of SAMs (all surfaces with contact angle θ_C~90° in air), which could be assigned to the bonding of thiols (CH_3-ended and OH-ended) to gold wafer and hydroxy group on the SAMs coated gold surfaces, respectively.

In addition, according to the control of the molar ratio of the two thiols (OH-ended and CH_3-ended) and the coating time, we obtained another group of surfaces with the same surface coverage of the OH-ended group. This group of surfaces had a contact angle of ~ 90° (Fig. C.6) but featured different alkyl length of the CH_3-ended thiols. XPS analysis verified that the surface coverage of -OH group for this group SAMs surfaces were basically the same (Fig. C.7).

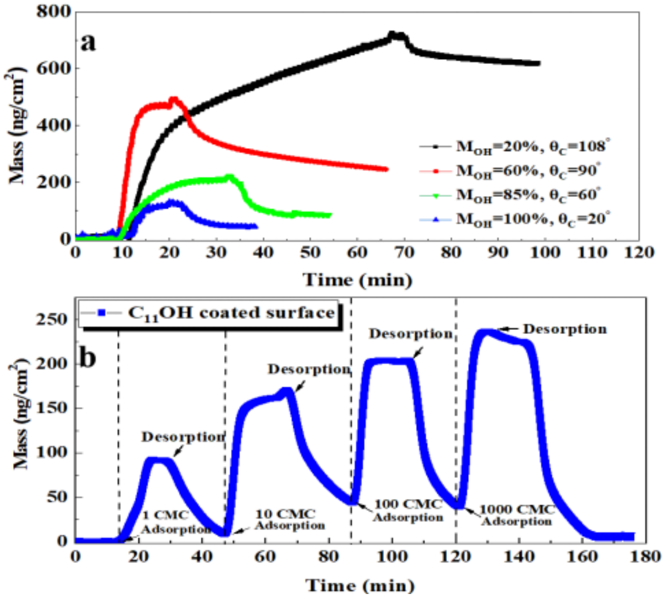

Figure C. 8: Mass as a function of time for (a) SPAN 80 (10 CMC) adsorption layer. (C_2OH only or C_2OH /$C_{11}CH_3$ at the interface with different hydrophobicity.) (b) SPAN 80 adsorptions on $C_{11}OH$ (M_{OH}=100%, θ_C=20°) SAMs surfaces at various concentrations. The increase of mass refers to as the adsorption process, and the decrease is the desorption process of washing.

The adsorption characteristics of SPAN 80 at the SAMs surfaces were investigated by QCM-D, whereas their effects on tuning the surface wettability were revealed by measuring the corresponding contact angle. Results are shown in Fig. C.8. The calculation of the mass of the adsorption layer in the QCM-D measurement is related to the changes in the vibration frequency and dissipation of the SAMs sensor, given by the following equation:

$$\frac{\Delta m}{A} = -\Delta f_n \left(\rho_q \mu_q\right)^{1/2} / 2n{f_1}^2 \qquad \text{(C-4)}$$

where Δf_n is the change in resonant frequency of the nth overtone of a crystal of fundamental frequency f_1, Δm is the change in mass (g), A is the area (cm^2), ρ_q is the density of quartz (2.648 g/cm^3), and μ_q is the shear modulus of quartz (2.947 × 10^{11} g/(cm·s^2)).

In non-polar solvents, the effect of surface hydrophobicity on the adsorption performance of non-ionic surfactants on the surface was studied by adjusting the chemical properties of the gold surface. Results in Fig. C.8a indicate that the average adsorption mass of SPAN 80 (10 CMC) on the SAMs surface was about 125 ng/cm^2 in equilibrium for SAMs with high -OH groups coverage (M_{OH} = 100%, θ_C = 20°). After washing by pure heptane, the average mass of adsorbed SPAN 80 decreased to less than 50 ng/cm^2 in equilibrium of desorption. With the decrease of the surface OH-ended group concentration from M_{OH}=85% to M_{OH}=60%, the adsorption amount of SPAN 80 (10 CMC) on the SAMs surface gradually increased from 220 ng/cm^2 to 500 ng/cm^2. After washing the surface with pure heptane, the mass of residual surfactant on the surface of SAMs with M_{OH}=60% was more than twice that of the surface with M_{OH}=85%, although the adsorbed surfactants on both surfaces have produced a relatively large degree of desorption. However, for the SAMs interface with a M_{OH} around 20% (θ_C = 108°), not only the adsorption density of SPAN 80 increased significantly by over 700 ng/cm^2, but also an irreversible adsorption on such a surface was observed. In summary, both SPAN 80 adsorption capacity and stability can be sharply improved by decreasing the OH-ended group concentration on SMAs surfaces.

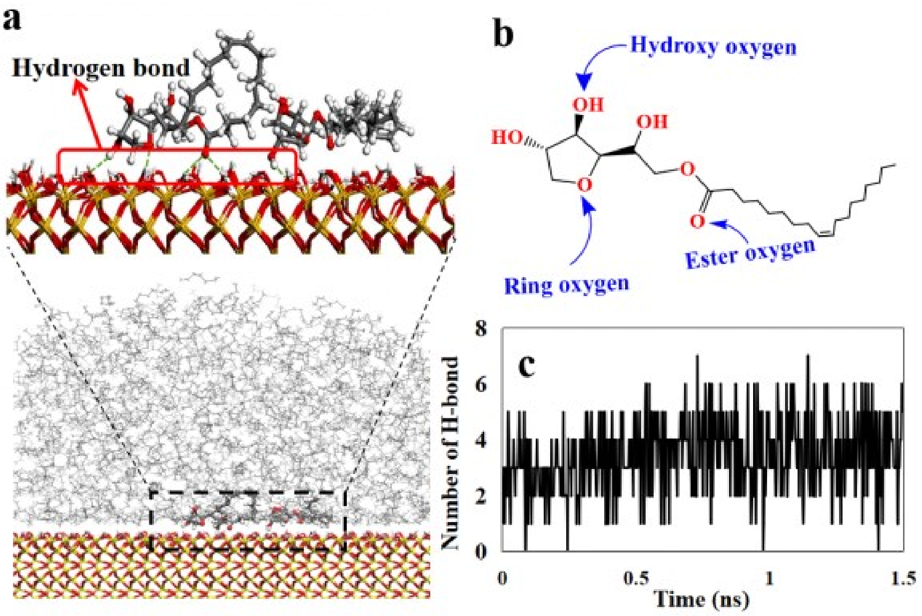

Figure C.9: (a) Nonionic surfactant SPAN 80 dissolved in 900 heptane molecules on 6.95 × 6.85 nm2 -OH group surface. An enlarged view of the hydrogen bonding between surfactant molecules and the surface is also shown on the top. (b) Chemical structure of nonionic surfactant SPAN 80. (c) Number of hydrogen bonds between surfactant and OH surface with time.

However, increasing the alkyl length of the OH-ended group on SAMs surface exhibited a less pronounced effect on the adsorption behavior of SPAN 80, as compared to the change of -OH group coverage. Results in Fig. C.5b indicate that, for -$C_{11}OH$ coated SAMs surface (M_{OH} = 100%, $\theta_C = 20^\circ$), the surface adsorption capacity of SPAN 80 increased slightly by 50 ng/cm^2 compared to the short alkyl length SAMs surface (-C_2OH, M_{OH} = 100%, in Fig. C.5a) with 10 CMC concentration of SPAN 80. Fig. C.8b also indicates that the adsorption amount of surfactant on the SAMs surface increased slowly when increasing the concentration of SPAN 80 in the solution. On the other hand, the reversible adsorption of SPAN 80 on coated surface was observed also after extending the alkyl length of the OH-ended SAMs from C_2 to C_{11}. The adsorption stability of surfactants on the surface should be related to the adsorption mechanism between surfactant molecules and the surface. It is most likely that non-ionic surfactant molecules should be bonded with OH group on silica surfaces through hydrogen bonds.[191] However, there is still a lack of unambiguous conclusions in terms of the nonionic surfactants' adsorption mechanism.

To answer this question, we proposed that the adsorption strength of nonionic surfactant molecules on OH-ended surfaces is related to the number of hydrogen bonds between the surfactant molecule and the surface. Molecular dynamics (MD) simulation was conducted to confirm our hypothesis. Details of the simulation method as shown below:

Hydroxylated silica surface with area 6.95×6.85 nm^2 and about 1.8 nm in height was prepared. 900 heptane molecules and 2 surfactant molecules were randomly placed in the simulation box with 10 nm vacuum gap in the z direction applied to eliminate any mirror image interactions due to periodic boundary conditions. INTERFACE forcefield was used to describe the interaction energies between components in the system. This relatively new force field is an extension on the platform of common harmonic force fields like (PCFF, CVFF, COMPASS, CHARMM, AMBER, GROMACS, and OPLS-AA). Among these extensions, CVFF-INTERFACE force field was chosen.

In addition to its generality, CVFF force field has already been utilized successfully in the literature and has been proven to produce reliable results. For instance, Liu *et al.* and Rogel successfully used CVFF force filed to describe asphaltene and other organic molecules in their systems. Tang *et al.*, in a molecular dynamics study of oil detachment from hydroxylated silica surface, used three sets of atomic charges including COMPASS, CVFF and INTERFACE force fields. In another study by Greathouse *et al*., the effect of salinity and temperature on adsorption of organic components on different clays including kaolinite, pyrophyllite and montmorillonite were studied using a combination of CVFF and Clayff.

Five different atom types were defined for silica substrate and partial charges of substrate atoms were assigned by differentiating bulk and surface atoms. To eliminate any excessive force on molecules, all simulations underwent steepest descent algorithm minimization with force tolerance of 10^{-10} kcal (mol Å)$^{-1}$. Systems was run for a 3 ns isothermal-isobaric (i.e., NPT) run at 300◦K and 1 atm using Nose-Hoover thermostat and barostat. Short range interactions were calculated using cut-off distance of 12.5 Å and long-range interactions were considered by using particle-particle particle-mesh (pppm) summation with accuracy of 10^{-4}. To keep silica slab stationary for ease of post processing as well as preventing layers from drifting, oxygen and silicon atoms in bulk slab were fixed by excluding them from integrations. Time step was set to 1 fs and collected trajectory in every 3000 steps in dynamic runs used for post processing. All simulations were conducted with LAMMPS simulation package.

As shown in Fig. C.9a, the surfactant molecules adsorbed on the surface through hydrogen bonds. MD results in Fig. C.9c show that the surfactant molecules exhibit different adsorption stability on OH-ended surface due to the difference in the number of hydrogen bonds between a single surfactant molecule and the surface. The number of hydrogen bonds ranges from 0 to 4 (average value is about 2), mainly happened between the SAMs surface (-OH group) and the hydroxyl oxygen, oxygen in the ring or oxygen of ester group of the surfactant SPAN 80 molecules, as shown in Fig. C.9b. The adsorption layer would become more stable with more hydrogen bonds between surfactant molecules and the surface. Therefore, after the washing process, the surfactant molecules with a small number of hydrogen bonds to the surface are prone to desorb from the surface. In general, MD simulation interprets that the insistent number of hydrogen bonds between the surfactant and the interface is the main reason for the difference in the adsorption stability of SPAN 80 on the OH-ended group SAMs surface after washing.

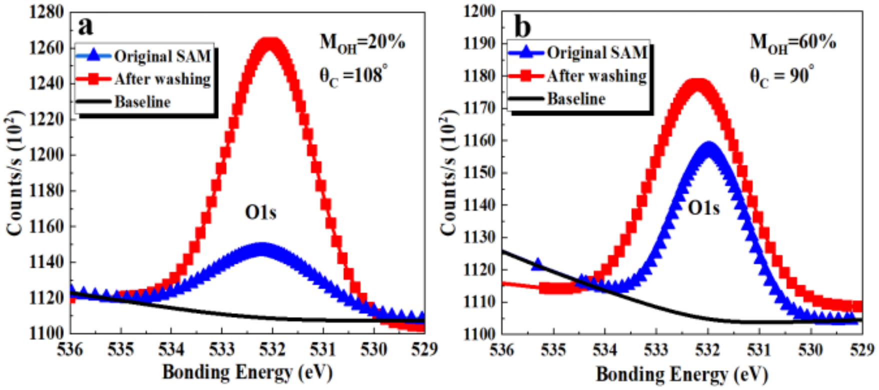

Figure C.10: Oxygen atoms concentration of various SAMs surface (a) M_{OH} = 20% (θ_C = 108°) and (b) M_{OH} = 60% (θ_C = 90°) before and after washing by pure heptane.

For high hydrophobicity SAMs surfaces, like surface with M_{OH} at 60% and 20%, we observed a strengthen in the adsorption ability of substances on such kinds of SAMs surface. However, it is possible that the heptane used in the adsorption experiment may still contain some impurities, such as methylcyclohexane and isooctane, although we used heptane with high purity (≥ 98%) as much as possible. These impurities are hydrophobic and might possibly adsorb on the hydrophobic SAMs surfaces with high methyl group concentration, which may cause greater interference on the surfactant adsorption experimental results. Therefore, it is necessary to confirm that the residual adsorbent on the surface was not from inevitable impurities but from the surfactant SPAN 80. Fig. C.10 shows the oxygen concentration for the washed SAMs surface and corresponding original SAMs surface by XPS analysis. For SAM surface with M_{OH} = 20% (θ_{C} = 108°), as shown in Fig. C.10a, the O1s signal intensity of the rinsed SAMs surface sharply increased compared to the original SAMs surface, which indicates that large amount of SPAN 80 was residue on the surface after washing. Similarly, for another washed SAMs surface (M_{OH} = 60%, θ_{C} = 90°), Fig. C.10b indicates that the O1s signal intensity of the washed surface was obviously higher than the corresponding original SAMs surface, verifying that the surfactant SPAN 80 did remain on the surface after washing by pure heptane. After comparison in Fig. C.10, it is found that the lower the coverage of OH-ended groups on the SAMs surface, the greater the amount of surfactant that could be stably adsorbed on the surface.

According to the results in Fig. C.8a and Fig. C.10, it has been determined that changes in the surface hydrophobicity can change the adsorption density of nonionic surfactants on the surfaces. The increase of the methyl group concentration on the surface of SAMs causes the adsorption density of SPAN 80 on the SAMs interface to increase. Surprisingly, however, we find that surface structure also plays an important role in surfactant adsorption, even if the surface hydrophobicity is the same. For example, the effect of the alkyl length of CH_3-ended SAMs on the adsorption of SPAN 80. Fig. C.11 shows the adsorption mass change of SPAN 80 on the SAMs surface. Surfaces were kept with the same surface hydrophobicity (M_{OH} = 60%, θ_{C} = 90°) but with different CH_3-ended alkyl length. The details of calculating the mass by dissipation (ΔD_n) and frequency (Δf_n) data are provided in Fig. C12 and Fig. C13, respectively.

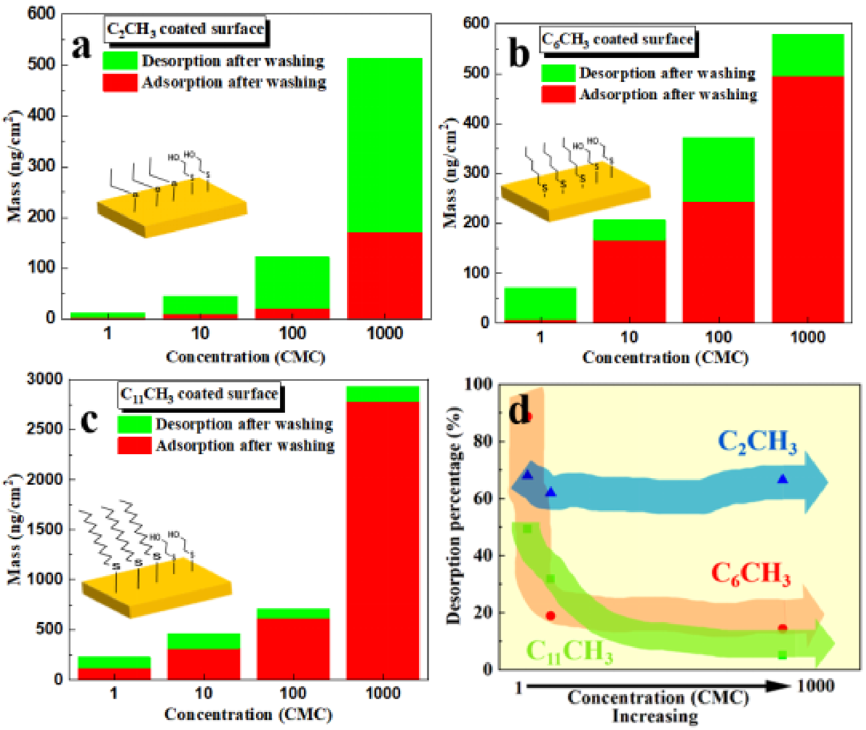

Figure C. 11: Adsorption mass changes of SPAN 80 on the surface of SAMs under different CH_3-ended alkyl lengths (a) C_2CH_3, (b) C_6CH_3, and (c) $C_{11}CH_3$. (d) Desorption percentage with concentration of SPAN 80 in heptane (M_{OH} = 60%, $\theta_C = 90 \pm 1.3°$).

By fixing the coverage of OH-ended and CH_3-ended groups on the SAMs surface (M_{OH} = 60%, $\theta_C = 90^{\circ}$), only the CH_3-ended alkyl length be adjusted. For the shortest alkyl length of the CH_3-ended SAMs, -C_2CH_3 in Fig. C.11a, SPAN 80 tended to be adsorbed on the surface reversibly. Most of the surfactant was desorbed from the surface after washing and the desorption percentage is greater than 60%, as shown in Fig. C.11d. Both the adsorption stability and the adsorption density of surfactants on the surface can be improved by increasing the alkyl length of SAMs. For example, when the alkyl length was increased to C_{11}, the desorption ratio could be as low as 5.1% (SPAN 80 concentration at 1000 CMC). Meanwhile, the adsorption capacity of SPAN 80 (concentration at 1000 CMC) increased from 150 ng/cm^2 to 2800 ng/cm^2, when the alkyl length was extended from C_2 to C_{11}. Besides, a large desorption ratio on the three SAMs surface were observed when the surfactant concentration was only 1 CMC. This is because most surfactants in low-concentration exist in the form of surfactant monomers, and the adsorption stability of single-molecule SPAN 80 on the SAMs surface is mainly determined by the number of hydrogen bonds between the two. The desorption of most SPAN 80 molecules from the surface is due to the weak hydrogen bonding strength with the hydroxyl groups on the surface of SAMs.

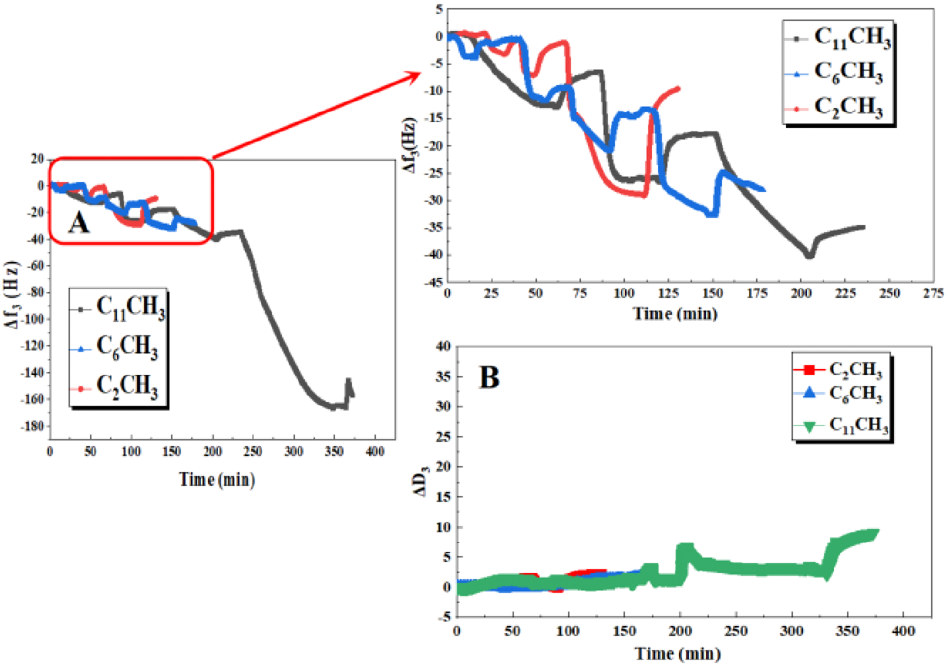

Figure C.12: (A) Vibration frequency change (Δf_3) and (B) dissipation change (ΔD_3) of SAMs sensors with different CH_3-ended carbon chain lengths in 10 CMC SPAN 80-Heptane solution (M_{OH}=60%, θ_C=90°).

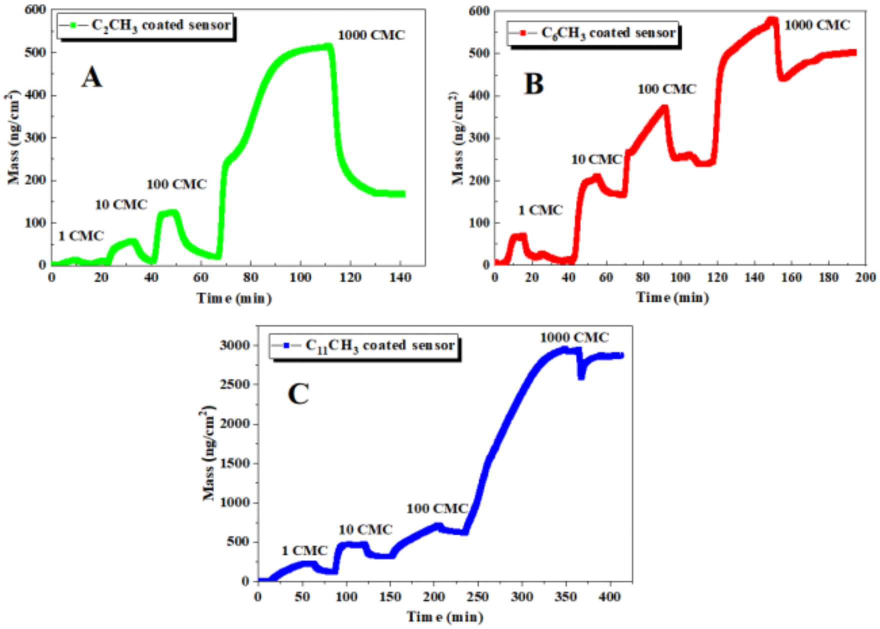

Figure C.13: Mass change of adsorbed SPAN 80 as a function of time for various SAMs surface with similar surface hydrophobicity (M_{OH}=60%, θ_C=90°) but different carbon chain length: (A) C_2, (B) C_6 and (C) C_{11} of CH_3-ended group on SAMs surface.

C.3.2 Relationship between surfactant adsorption capacity and surface charges

Non-ionic surfactants have a decisive effect on the charging of particles in non-polar solvents.[192] However, there were only few studies on the effect of particle surface chemistry on particle charging in non-polar solvents. With the results from Section C.3.1, we could explore the relationship between the particle surface chemical properties and the particles charging behavior in a non-polar solvent with SPAN 80 used as charge additives. Detailed operation steps and characterization methods of particle surface chemical modification are provided as below.

Prior to silanization, silica particles were dried for 10 h at 150 °C under nitrogen atmosphere and were used immediately. In a typical synthesis procedure, 25 mg silica particles (200–250 nm) were dispersed in dry toluene and stirred for 30 min. To the above mixture, 100 ml, 0.05% Tricholoro(dodecyl)silane (TDS-C_{11}, w/w) solution in toluene was added drop wise. This solution was then allowed to rest for 24 hours, filtered, and washed several times with toluene and ethanol to remove unreacted TDS-C_{11}. These modified silica particles (TDS-C_{11}-silica, θ_C=60°) were subsequently dried in a vacuum oven at 60-70 °C for 4 h and used for further characterization. Similarly, the silanization was carried out by changing the % of TDS-C11 (w/w) in toluene (*i.e.,* 0.15, 0.2) to obtain various hydrophobicity silica particles (θ_C equal to 90° and 108°) and by using different reagents such as Tricholoro(ethyl)silane (TES-C_2) and Tricholoro(hexyl)silane (THS-C_6) to create three specific SAMs surfaces with various carbon chain length but with consistent hydrophobicity (θ_C=90°). The FTIR spectra of pristine and modified silica particles are shown in Fig. C.14, which gives clear evidence for particle surface modification.

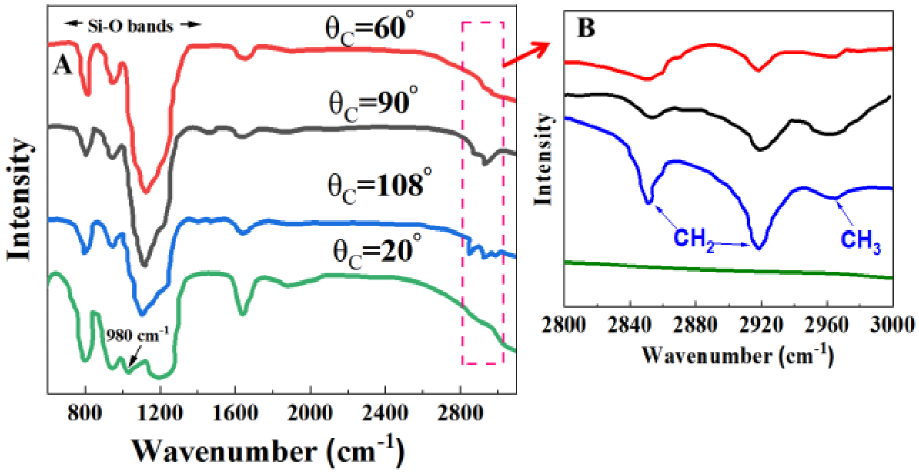

Figure C.14: Infrared spectra of silica samples at different chlorosilane concentrations.

It should be noted that at the same chlorosilane concentration, the length of the carbon chain has no significant effect on the infrared spectrum results, so it is not shown separately here. As shown in Fig. C.14(a), in the low frequency region, 700~1400 cm^{-1}, and fundamental Si-O bands are invariant with surface modification, while in the high frequency region certain distinct changes could be seen. Nevertheless, the band at 980 cm^{-1} is related to the stretching modes of isolated silanols and is visible only in the case of bare silica. Furthermore, the absence of this band in chlorosilanes-silica sample indirectly suggests chlorosilanes bonding on the silica surface. From Fig. C.14(b), new bands at 2850 and 2919 cm^{-1} of $-CH_2$ due to $-CH_3$ symmetric and antisymmetric stretching respectively indicate the presence in the peak positions that can be attributed to the entanglements of hydrocarbon chains after chlorosilane monomer adsorption on a surface.

The surface chemistry of particles plays an important role on their charging behavior in non-polar solvents. The results in Fig. C.15 reveal the effect of surface hydrophobicity on the zeta potential of particles with various concentration of SPAN 80. It is worth noting that overall, the contact angle characteristics of these four types of nanoparticles are basically the same as the contact angle characteristics of the previous large, flat surfaces. Therefore, we have made a reasonable assumption that the conversion of the research object from plane to nanoparticle will basically not affect this conclusion. It is indicated that particle surfaces could not be electrically charged at low surfactant concentration (e.g., 0.1 CMC) due to the lack of reverse micelles as charge carriers in the bulk solution. There exists a certain space in the middle of the reverse micelle, which can accommodate and stabilize polar ions in non-polar solvents.[193] When the surfactant concentration was high enough, the zeta potential of the particle surface increased. As showed in Fig. C.15a, particles with high OH-ended group coverage were positively charged in the non-polar heptane in the presence of SPAN 80, such as pure silica (Si-OH existing only, $\theta_C = 20^\circ$). This phenomenon is consistent with literature values[181] and is attributed to acid-base interaction by most researchers.[91] When there were only hydroxyl groups on the surface of the particle, the surface acted as a Lewis base, and the nonionic surfactant SPAN 80 could be considered as a Lewis acid. After the base-acid interaction, the Si-OH group on the particle surface acted as an electron donor, which was positively charged. However, when silica particles were coated with -CH_3 groups, many properties of silica would be changed, including the acid-base property.[91]. During the particles charging experiments, we observed the phenomenon of zeta potential reversal for silica particles before ($\theta_C = 20^\circ$) and after ($\theta_C \geq 60^\circ$) CH_3-ended thiol modification in the Fig. C.15a. Similarly, Poovarodom *et al.*[179] also indicated that for nonionic surfactant in non-polar solvents, -CH_3 thiol treated silica particles were negatively charged. It is possible that the increase in the concentration of surface methyl groups has changed the Lewis acidity and alkalinity of the particle surface. Namely, the surface methyl coated particle surface behaves as a Lewis acid, while the nonionic surfactant is a Lewis base according to a semi-heuristic method to analysis, which borrows its notation and conceptual framework from the theory by van Oss, Chaudhury, and Good (vOCG) for the surface and interfacial energy of pure phases.[194] Therefore, after the surfactant (positively charged through acid-base interaction) is desorbed from the surface, the particle surface appears to be negatively charged.

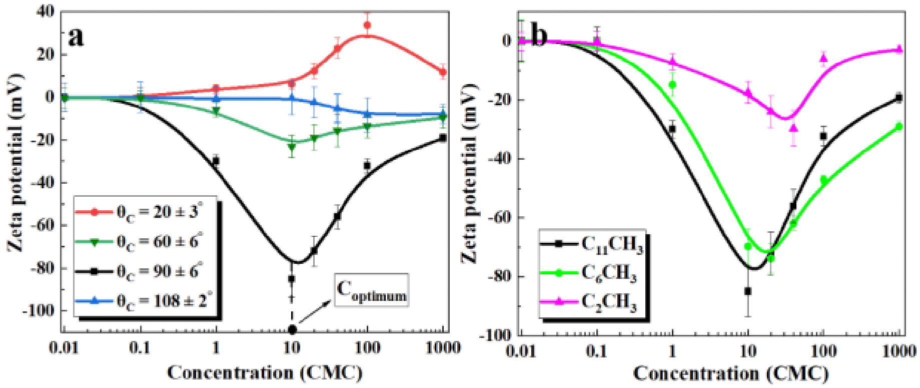

Figure C. 15: (a) Effect of surface (Si-OH only or mixed Si-OH/ $-C_{11}CH_3$) wettability on particle zeta potential with various concentration of nonionic surfactant SPAN 80. (Coptimum: a critical concentration where the charging strength of surface arrive maximum) (b) Effect of surface coating alkyl length ($M_{OH} = 60\%$, $\theta_C = 90 \pm 6°$) on particle zeta potential with various concentration of nonionic surfactant SPAN 80. The solid line is only for guiding the eyes.

As the hydrophobicity of the particle surface increased (contact angle from 20° to 90°), the surface charge of the particle became more negative under the same surfactant concentration, as shown in the Fig. C.15a. Our finding partly endorses the hypothesis provided by Fowkes *et al.*,[183] where the authors demonstrated that the silane treatment reduced the number of available acidic surface silanol (Si–OH) groups on the particle surface. In our system, the number of -OH group also decreased, as shown in Fig. C.5e-h. However, they proposed that all silane treated particles were expected to reduce the surface charge strength, not to increase as observed in this work. If the concentration of $-CH_3$ group on particle surface was increased further, e.g., increasing the hydrophobicity of the modified particles from 90° to 108°, the surface charge of the particles became more neutral due to lack of available acidic -OH group on the surface.

We observed the unusual charging behavior of particles with a hydrophobicity between 20 and 90°. When hydroxyl concentration on the surface of the particles gradually decreases, the charging strength of the particles still increases. The specific reasons for this unusual behavior are now discussed in detail. Based on the acid-base interaction theory, it was proposed that the density of acid (or base) sites on the surface determines the charging strength of the surface in non-polar solvents. The higher the interaction site density, the stronger the charging strength of the surface in non-polar solvents with nonionic surfactants acting as charge additives. However, the influence of the adsorption density of the surfactant on the surface charging behavior is easily overlooked, although it is also important in theory. For example, in the pure silica-heptane-SPAN 80 system, the hydroxyl groups on the surface of the alkaline silica serve as the electron donor, and the corresponding acidic SPAN 80 adsorbed on the surface serves as the electron acceptor. Even if rich electron donors (hydroxyl concentration) are provided on the surface, the density of electron acceptors (such as the adsorbed SPAN 80) on the surface could be insufficient. Under such circumstances, the surface charging strength in non-polar solvent is still hard to be improved, and vice versa. Therefore, it is reasonable to hypothesize that the charging behavior of the particles in non-polar solvents depends not only on the surface hydroxyl groups, but also on the adsorption capacity of the surfactant (e.g., reverse micelle) on the surface. In the previous section, we have demonstrated that the presence of alkyl-silane is beneficial to increase the adsorption capacity of surfactant on the surface (Fig. C.8). If the concentration of CH_3-ended group on the surface is insufficient, there would have a significant reduction on the adsorption density of reverse micelles on the particle surface. Thus, such surfaces cannot provide enough reverse micelles to interact with the -

OH groups on the surface, even if the density of -OH group concentration is extremely high. Therefore, the charge strength of pure silica is still relatively low even though the density of the OH group concentration on the surface is the highest. On the other hand, further increasing the methyl concentration on the surface reduces the surface OH-ended group density (e.g., in the case of M_{OH} = 10%, θ_{C} = 108°). Even if their corresponding adsorption capacity of reverse micelle on the particle surface increases sharply, there are insufficient -OH groups interacting with the adsorbed surfactant SPAN 80. Therefore, the strongly hydrophobic particles still tend to be neutrally charged in non-polar solvents. It is comprehensively shown that the particle charge intensity in the non-polar solvent could be maximized only in the cases when the concentration of the electron donor and the electron acceptor matches each other the best. One of the examples found in our experiment is the group with surface contact angle at 90° (M_{OH} = 60%). It exhibited a zeta potential value up to -70 mV.

On the other hand, Fig. C.15b revealed the effect of the alkyl length of the chlorosilane on particles charging behavior (constant wettability, θ_{C} = 90°). Results in Fig. C.15b show that longer alkyl length of the CH_3-ended chlorosilane on particles surface would result in more negative zeta potential values, which is possibly due to a stronger adsorption capacity of the surfactant on the surface. However, it is also found in Fig. C.15 that the charging strength of all particles decreased above a certain amount of surfactant concentrations. These critical concentrations are labelled as C_{optimum} (e.g., C_{optimum} = 10 CMC for the M_{OH} = 90% group). The decline in particle zeta potential at high surfactant concentration is a commonly reported behavior.[195] Such a decline in zeta potential could be attributed to the higher number of charged micelles generated via the disproportionation process. To be more specific, the disproportionation progress describes the scenario where two neutral micelles exchange their charges, generating one positively charged micelle and another negatively charged micelle.[196, 197] These resulting charged micelles serve as counter-ions, which could screen or partially neutralize the particle surface charges. The adsorption amount of the surfactant on the silica surface was relatively low compare with other surfaces containing methyl groups under the same surfactant concentration, as shown in Fig. C.155a. Therefore, the charge neutralization effect of the charged reverse micelle ions on the pure silica surface was also greatly reduced, and the C_{optimum} for pure silica (~100 CMC) was much larger than other modified particles (~10 CMC). The same experimental phenomenon also can be observed from Fig. C.15b. The adsorption capacity of surfactants on the surface increased with increasing alkyl length on the SAMs surface, therefore the adsorption probability of charged reverse micelles on the surface accordingly increased. Compared with shorter alkyl length (-C_2CH_3) coated silica particles, the C_{optimum} of -$C_{11}CH_3$ coated silica surface was the smallest.

On the other hand, increasing the alkyl length of the CH_3-ended group is beneficial to enhance the adsorption stability of surfactant on silica surface, which may be detrimental to surface charging in non-polar solvents. According to the charging process of the surface in the non-polar solvent, as shown in Fig. C.1, the surface and the surfactant are charged with opposite charges after the adsorbed non-ionic surfactant interacts with the surface by acid-base interaction. Next, the charging strength of the surface can increase accordingly only after the charged surfactants were desorbed from the surface. For surfaces with the same hydrophobicity, the desorption probability of SPAN 80 on the surface would gradually decrease as the alkyl length of CH_3-ended SAMs increases, and it is difficult for charged surfactants to desorb from the surface. Consequently, the lower probability of charged surfactants to desorb from the surface may be another important reason for the decrease in surface charge strength in non-polar solvent.

C.4 Summary

In this chapter, we determined the effect of surface structure and chemical properties on the surface charging with a nonionic surfactant used as a charge control additive in a non-polar solvent. In the classic acid-base interaction theory, the density of the electron acceptor (such as hydroxyl group) on the surface determined the charge strength of the surface in non-polar solvents.[198, 199] However, little attention was paid to the impact of electron donor density (e.g., adsorbed surfactant) on the surface charging behavior. In this work, it was proved that the electron donor density is equally important to surface charging in non-polar solvents. Silane-treated particles were found to reduce the surface charge strength when its hydrophobicity was between 90° to 108°. This result is consistent with previous discoveries in the literature[200] and could be explained by the decreasing number of available electron acceptors (hydroxyl groups) on the particle surface. However, a surprising charging behavior of particles was discovered for the first time, when the hydrophobicity was tuned to between 20° and 90°. For this group of particles, their hydroxyl concentration on the surface gradually decreased, but their corresponding charging strength kept increasing. Such an abnormal enhancement of surface charges in a non-polar environment is most likely because the adsorption density of the surfactant on the surface increased for particle surfaces with a contact angle of 20°-90°. More importantly, results from this study emphasized that the surface charging strength could be improved by optimizing the matching degree of electron donor-acceptor density through the regulation of surface chemical properties and nanostructures. One of the most representative examples found in our experiment was the group with a surface contact angle at ~ 90°, which exhibited an optimum zeta potential value up to -70 mV.

On the other hand, previous studies were mainly focused on exploring the influence of surfactant concentration on the surface charging strength in non-polar solvents[197]. It is believed that the charging strength decreased above a certain surfactant concentration, which could be attributed to the charge neutralization effect with a higher number of charged micelles generated via the disproportionation process[201]. However, the results from this research also pointed out that the adsorption stability of surfactants might be another important factor for the changes in surface charge intensity in non-polar solvents. According to the charging process of the surface in the non-polar solvent, the surface and the surfactant are charged with opposite charges after the adsorbed non-ionic surfactant interacts with the surface through acid-base interaction. Subsequently, the charging strength of the surface can be increased accordingly only after the desorption of charged surfactants from the surface. Therefore, the surface charging strength could be reduced if the surfactant possesses a lower probability of desorbing.

Additionally, for surfaces with pure hydroxyl groups such as silica, this study indicated that SPAN 80 adsorbed on silica surfaces by hydrogen bonding. The bonding strength was proportional to the number of hydrogen bonds between the surfactant molecules and the surface. By adjusting the surface chemical structure, such as by increasing the concentration of surface CH_3-ended groups or extending the alkyl length of CH_3-ended groups, the adsorption stability of surfactants on the surface would be enhanced. In general, this study provides insights into the charging phenomenon in non-polar solvents and contributes to a more comprehensive understanding of the underlying mechanism. This study could also provide valuable guidance on developing effective charge control additives for industrial applications.